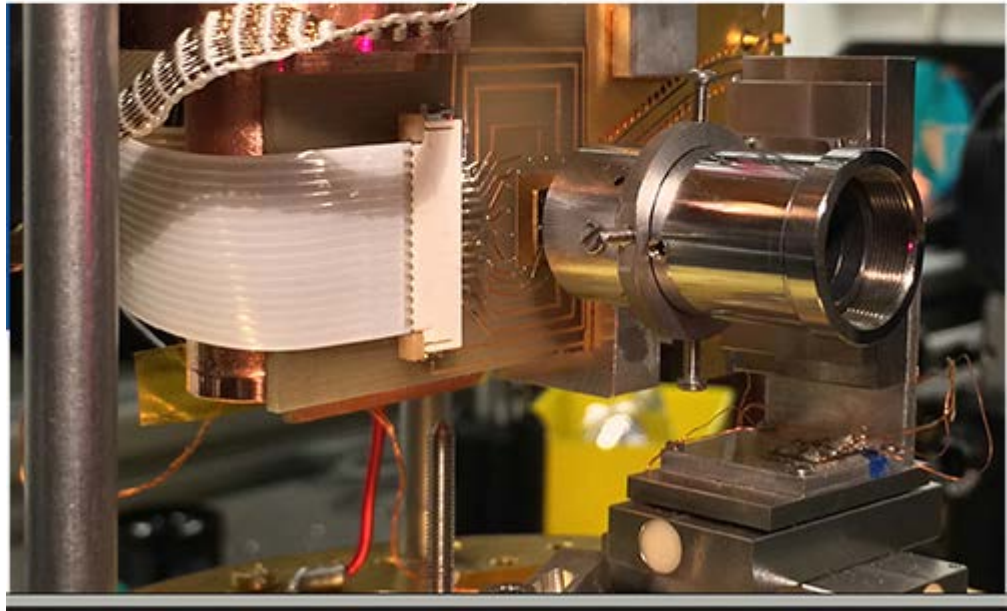


Spectral evidence for a condensate of dark excitons in a trap

MUSSIE BEIAN

Advisor: Prof. Dr. Maciej Lewenstein

Co-Advisor: Prof. Dr. François Dubin



To my parents

Abstract

Spatially indirect excitons, being composite bosons, are attractive candidates to explore correlated many-body systems. They possess an inherent large electric dipole, a four-fold spin manifold, and can be studied via the emitted photoluminescence after electrons and holes have recombined. Due to their extremely low mass compared to atoms, a sufficiently dense gas of indirect excitons is expected to form a Bose-Einstein condensate below a critical temperature of a few Kelvins. Recent theoretical results show that this condensation must take place in optically dark states of the spin manifold. However, under a density increase the condensate is expected to coherently couple to a small population of bright excitons. It is then possible to study the condensate through its weak photoluminescence.

In this thesis we report on experiments with a cold gas of indirect excitons in coupled quantum wells embedded in a field effect device. Indirect excitons are photo-generated through pulsed laser excitation, in a fashion that minimizes photo-induced perturbations in the field-effect device. Confinement is provided by exploiting the high-field seeking dipolar nature of spatially indirect excitons through independently biased surface gate electrodes. Time and spectrally resolved analysis of the photoluminescence allow us to extract the decay time of the bright exciton population while at the same time monitoring the decay of the overall exciton population through the energy of the photoluminescence. Maintaining a fixed density while varying the bath temperature, we are able to observe a depletion of the bright state population, by even three-fold when the bath temperature is lowered from 3.5 K to 0.33 K. This stands in stark contrast to the expected classical behavior of a cold gas of excitons obeying Maxwell-Boltzmann statistics. The experimental results are confirmed by a phenomenological model which shows that Bose-stimulation from bright to dark excitons is compatible with the observed anomalous darkening. Lowering the exciton gas temperature should reinforce these signatures. However, in GaAs exciton-phonon interaction is the main mechanism to cooling an exciton gas to quantum degeneracy. The efficiency of this process is strongly reduced for temperatures below 330 mK. We have thus developed a technique to control the exciton confinement in-situ, on a

time-scale of nanoseconds by pulsing the gate electrode. Our approach relies on a complete characterization of the transfer function linking the response of the indirect excitons to a voltage pulse, i.e. the strength of the confining potential. Our method shows no increase of the bath temperature thus paves the way towards exploration of evaporative cooling methods for a gas of cold indirect excitons.

Resumen

Los excitones espacialmente indirectos, siendo bosones compuestos, son muy buenos candidatos para explorar sistemas de muchos cuerpos correlacionados. Estos excitones poseen un gran momento dipolar intrínseco, spin de estado cuádruple, y pueden ser estudiados a partir de medir el espectro de fotoluminiscencia generado producto de la recombinación de un electrón con un hueco. Debido a su masa extremadamente pequeña comparada con la de los átomos, es de esperar que un gas de excitones indirectos suficientemente denso de lugar a la formación de un condensado Bose-Einstein por debajo de la temperatura crítica de unos pocos grados Kelvin. Resultados teóricos recientes muestran que esta condensación pasa en estados ópticamente oscuros del estado spin. Sin embargo, bajo un incremento de la densidad se espera que el condensado se acople coherentemente a una pequeña población de excitones brillantes; Siendo entonces posible estudiar el condensado a través de su débil fotoluminiscencia.

En esta tesis reportamos experimentos con gases fríos de excitones indirectos acoplados con pozos cuánticos implementados en un dispositivo de efecto de campo. Los excitones indirectos son foto-generados a través de la excitación con un láser pulsado, de manera que se minimizan las perturbaciones foto-inducidas en el dispositivo de efecto campo. El confinamiento se proporciona aprovechando los altos campos en busca de naturaleza dipolar de los excitones espacialmente indirectos a través de electrodos de contactos superficiales con tensión de polarización independiente. El análisis temporal y espectral de fotoluminiscencia nos permite extraer el tiempo de decaimiento de la población de excitones brillantes mientras que al mismo tiempo podemos monitorizar el decaimiento de la población total de excitones a través de la energía de la fotoluminiscencia. Manteniendo la densidad fija mientras se varia la temperatura de baño, somos capaces de observar una reducción de la población del estado brillante de hasta tres veces cuando la temperatura de baño disminuye des de 3.5 K a 0.33 K. Esto está en marcado contraste con el comportamiento clásico esperado para un gas frío de excitones que obedece la estadística de Maxwell-Boltzmann. Los resultados experimentales son confirmados por un modelo fenomenológico que muestra que la

estimulación de Bose de de excitones brillantes a excitones oscuros es compatible con el oscurecimiento anómalo observado. Se espera que una disminución en la temperatura del gas del excitón refuerce estas características. Sin embargo, en GaAs, la interacción excitón-fotón es el principal mecanismo de enfriamiento de un gas de excitones hasta la degeneración cuántica. La eficiencia de este proceso es fuertemente reducida para temperaturas por debajo de 330 mK. Por este motivo hemos desarrollado una técnica para controlar el confinamiento de excitones “in-situ”, en una escala de tiempo de nanosegundos mediante el contacto de electrodos pulsados. Nuestro enfoque se basa en la caracterización completa de la función de transferencia relacionando la respuesta de los excitones indirectos a un voltaje pulsado, por ejemplo la fuerza del potencial de confinamiento. Nuestro método muestra un incremento nulo de la temperatura de baño cosa que abre el camino a la exploración de métodos de enfriamiento por evaporación para gases fríos de excitones indirectos.

Résumé

Les excitons spatialement indirects, en tant que bosons composites, constituent des candidats intéressants pour l'exploration des systèmes corrélés à N-corps. Ils possèdent en effet un large dipôle électrique intrinsèque, une variété de spin quadruplement dégénérée, et peuvent être étudiés grâce à la photoluminescence émise lorsque les électrons et les trous se recombinent. Bénéficiant d'une masse extrêmement faible par rapport aux atomes, un gaz d'excitons indirects suffisamment dense devrait former un condensat de Bose-Einstein en-dessous d'une température critique de quelques degrés Kelvin. Des résultats théoriques récents montrent que cette condensation doit survenir au sein des états optiquement noirs de la variété de spin. Cependant, une augmentation de densité devrait amener le condensat à se coupler de manière cohérente avec une faible population d'excitons brillants. Il devient alors possible d'étudier le condensat par le biais de sa faible photoluminescence.

Ce manuscrit décrit nos expériences sur un gaz froid d'excitons indirects dans un double puits quantique intégré à un dispositif à effet de champs. Les excitons indirects sont générés optiquement par une excitation laser pulsée, d'une manière qui minimise les perturbations induites optiquement dans le dispositif à effet de champs. Le confinement est assuré en utilisant la nature dipolaire des excitons spatialement indirects. En effet ceux-ci sont attirés vers les zones de forts champs électriques qui sont créés grâce à des électrodes de surface polarisées de manière indépendante. Les analyses temporelles et spectrales de la photoluminescence permettent d'extraire le temps de déclin de la population d'excitons brillants tandis que le déclin de l'ensemble de la population d'excitons est contrôlé grâce à l'énergie de la photoluminescence. En maintenant une densité fixe tout en variant la température de l'échantillon, nous observons une réduction de la population des états brillants qui peut atteindre un facteur trois lorsque la température est diminuée de 3.5 à 0.33 K. Ceci contraste fortement avec le comportement classique et attendu d'un gaz froid d'excitons soumis à la statistique de Maxwell-Boltzmann. Ces résultats expérimentaux sont confirmés par un modèle phénoménologique montrant que la stimulation de Bose des états brillants

vers les états noirs est compatible avec le noircissement anormal observé. Une diminution supplémentaire de la température du gaz d'excitons devraient ainsi pouvoir renforcer ces signatures. Néanmoins, dans le GaAs, l'interaction entre phonons et excitons est le principal mécanisme de refroidissement des excitons vers la dégénérescence quantique et l'efficacité de ce processus est fortement réduite pour des températures inférieures à 330mK. Nous avons donc développé une technique de contrôle du confinement des excitons in-situ, en pulsant la tension aux électrodes avec une résolution temporelle de l'ordre de la nanoseconde. Notre approche repose sur une caractérisation complète de la fonction de transfert reliant la réponse des excitons indirects aux pulses de tension, c'est-à-dire à la force du potentiel de confinement. Notre méthode ne provoque aucune augmentation de la température de l'échantillon et ouvre donc la voie à l'exploration des processus de refroidissement évaporatif pour les gaz froids d'excitons indirects.

Acknowledgements

First of I would like to take the opportunity to thank Pr. Maciej Lewenstein for his generous and continuous support of our experimental project at ICFO and even after our move to Paris. I would also like to thank my thesis supervisor Francois Dubin for giving me the opportunity to join his team and his extensive and dedicated support throughout the last years. Thank you very much this would not have been possible without you, I wish you all the best for the future.

A big thanks goes also to Mathieu Alloing, my brother in arms throughout most of the PhD, for his dedication, motivation and patience when introducing me to the experiment and during alot of the measurements. We started as a group of three at Barcelona and soon grew to five with the arrival of Romain Anankine and shortly after of Suzanne Dang. They quickly became a big help and I had the great opportunity with Francois and Mathieu to introduce them to our experiment. Thank you for your help and I wish the two of you all the best for the remainder of your PhD.

This PhD wouldn't have been possible without the dedicated support of several collaborators. In particular I would like to thank our collaborators from LPN, Aristide Lemaître and Carme Gomez, for providing us with such great samples. The success of this project is also largely a result of the expertise of the research engineers, at LPN Edmond Cambрил and Kamel Merghem and at ICFO Johan Osmond and Luis Enrique Romero who helped me in realizing and connecting the gate structures on our sample. Your patience and hard work during the countless hours in the clean room were of fundamental importance for this PhD. I would also like to express my gratitude to Monique and Roland Combescot for their great theoretical input which was a big influence on my work. It was an honor to work with such outstanding theorists and to benefit from their extensive knowledge. This experiment also largely benefited from the mechanical and electronic workshops at both ICFO in Barcelona and INSP in Paris. In particular I would like to thank Jose-Carlos Gonzales at ICFO for his support during the construction of the printed circuit board which was an important part of this thesis.

This PhD led me through two institutes in two different countries and I'm truly grateful for having met so many great people. Thanks for making the time in and outside of ICFO so much fun. Stefan Engelhart Teichmann, Benjamin Wolter, Achim Woessner, Peter Weber, Barbara Buades, Noslen Soares, Ioannis Tsuotsis, Esteban Bermudez, Gabriele Navickaite, Jana Nieder, Francisco Da Silva, Seth Cousing, Dane Austin, Judit Dura, Michael Geiselmann, Jan Gieseler, Dominik Kufer, James Douglas, Erin Babinsky, Alexandros Tavernarakis Johannes Guettinger, Sebastian Thompson, Allison Thompson(not related), Antoine Reserbat-Plantey, Kevin Schaedler, Idris, Chiara Brophy, Michael Pullen Michele Sclafani. The same holds true for the great people that I met during my stay in Paris: Richard Hostein (thank you so much for your help during the move to Paris) Maja Brunstein, Iñaki, Gwenn Le Pavic, Aboubakre Benhallam, Meryem Bensaid, Maxime Mansour and Florian Piolain.

At this point it is time to thank my family for their whole support throughout their journey, your love and trust was invaluable. Thank you so much!

At last I would like to thank you Anjana, for your love, your humor your patience and continued support during all the time which took us together from Paris to Barcelona. I am truly lucky to have had you throughout this great journey.

Contents

| | |
|---|-----------|
| Introduction | 1 |
| 1 Excitons in Semiconductors | 5 |
| 1.1 Excitons in bulk Semiconductors | 5 |
| 1.2 Excitons in 2D | 7 |
| 1.3 Trapping spatially indirect excitons in coupled quantum wells . . | 8 |
| 1.3.1 Increase of the exciton lifetime | 8 |
| 1.3.2 The exciton dipole | 10 |
| 1.3.3 Electrostatic traps for spatially indirect excitons | 12 |
| 1.4 Formation and decay of spatially indirect excitons | 13 |
| 2 Bose-Einstein-Condensation of excitons | 17 |
| 2.1 Basic theory of BEC | 18 |
| 2.2 Bose-Einstein condensation of spatially indirect excitons | 20 |
| 2.3 The dark condensate - The role of the spin | 23 |
| 2.4 Advances towards the realization of an exciton BEC | 25 |
| 2.5 Expected signatures for dark state condensation | 29 |
| 3 Sample and Experimental Setup | 31 |
| 3.1 Experimental Setup | 31 |
| 3.1.1 The Cryostat | 31 |
| 3.1.2 The Laser System | 33 |
| 3.1.3 Photoluminescence Detection | 34 |
| 3.2 Experimental Control | 35 |
| 3.3 Sample design and fabrication | 36 |
| 3.3.1 Heterostructure Layout | 37 |
| 3.3.2 Trap design | 38 |
| 3.3.3 Contact fabrication | 40 |
| 3.3.4 Electrical properties of the heterostructure | 42 |
| 4 Electrostatic trapping of spatially indirect excitons | 45 |
| 4.1 Exploring the potential landscape | 46 |
| 4.1.1 Trap Depth - Recording a Potential Map | 47 |

Contents

| | | |
|----------|--|-----------|
| 4.1.2 | Electric Charges in the field effect device | 48 |
| 4.1.3 | Measurement of the dipole moment | 49 |
| 4.1.4 | Linewidth | 50 |
| 4.2 | Trap stability | 53 |
| 5 | Trapped indirect excitons in the cold temperature regime | 55 |
| 5.1 | Measuring the indirect exciton population in the trap | 56 |
| 5.1.1 | Extracting the density at 330mK | 57 |
| 5.1.2 | Density dynamics at higher Temperatures | 58 |
| 5.2 | Studying the luminescence linewidth | 59 |
| 5.3 | Probing the spatial profile of the exciton gas | 62 |
| 5.4 | Studying the distribution between dark and bright states | 62 |
| 5.5 | Modeling the dynamics between the dark and bright states | 65 |
| 5.6 | Conclusion | 68 |
| 6 | Arbitrary in-situ control of the potential landscape | 71 |
| 6.1 | Exciton thermalisation and evaporative cooling | 72 |
| 6.2 | Arbitrary high-speed control of the exciton confinement | 74 |
| 6.2.1 | The Arbitrary Waveform Generator | 74 |
| 6.2.2 | Coaxial Transmission Lines | 74 |
| 6.2.3 | Design of the printed circuit board | 75 |
| 6.3 | Characterization of the Components | 76 |
| 6.4 | Engineering the arbitrary voltage pulse | 78 |
| 6.4.1 | Experimental determination of the Transfer Function | 79 |
| 6.4.2 | Determining the corrected pulshape | 81 |
| 6.5 | Conclusion | 85 |
| 7 | Conclusion and Outlook | 87 |
| | Bibliography | 89 |

Introduction

The realization of a Bose-Einstein condensate (BEC) has been a long standing goal in the field of many-body physics since its theoretical formulation based on the works by Satyendranath Bose and Albert Einstein. Bose-Einstein condensation occurs when an ideal gas of non-interacting bosonic particles is cooled below a critical temperature. Below this temperature the ground state of the system becomes macroscopically populated and thus forms a Bose-Einstein condensate. The critical temperature, at which the phase transition occurs, scales inversely with the boson mass. Thus, Wannier-Mott excitons in semiconductors, a bound state of an electron-hole pair forming a composite boson, were believed to be promising candidates for the realization of this peculiar state of matter.

The hope for an exciton condensate was founded on proposals made by Moskaleiko and Blatt and additional calculations by Keldysh in the early 1960's [60, 11, 45]. At the time, it was expected that the condensation could easily be observed at a temperature of 100 K or even room temperature since the excitons effective mass amounts only to a fraction of the electrons mass. Inspired by their theoretical groundwork, early experiments focused on producing a gas of excitons in a bulk semiconductor. The most prominent example following this approach involved Cu_2O which has been studied for more than 30 years [78]. However, a BEC of excitons in Cu_2O could not be demonstrated due to Auger recombination and bi-exciton formation that limit the creation of a sufficiently dense gas necessary to create a BEC of excitons [89]. In fact, the first Bose-Einstein condensate was not observed with excitons, but for another species of bosonic particles, neutral alkali atoms.

The first successful realization of a Bose-Einstein condensate was demonstrated by Cornell and Wiemann at NIST in 1995 with rubidium atoms [5]. Shortly after this, the group of Wolfgang Ketterle at MIT demonstrated a BEC of sodium atoms [24]. Two years later Ketterle and coworkers were able to perform one of the most impressive fundamental tests of quantum mechanics by observing interference between two freely expanding condensates [7]. This demonstrated the quantum mechanical matter-wave nature exhibited by a Bose-Einstein condensate

Introduction

on a macroscopic order. These revolutionary achievements lead to the award of the Nobel Prize in Physics to Cornell, Wiemann and Ketterle in 2001. However, this remarkable achievement was preceded by enormous technical challenges [22]. To observe the phase transition, the atomic cloud had to be confined in space using a magneto-optical trap and cooled down through evaporative cooling below the order of $1 \mu\text{K}$ [64, 5, 24], making the use of a huge experimental setup necessary to meet the necessary temperature requirements. Nevertheless, these remarkable technical achievements have led to the realization of BEC for several other atomic species and paved the way towards the discovery of novel phenomena in the field of many-body-physics [12].

Advances of ultra-cold quantum gases with neutral atoms, however, has not lead to a decreased interest in the realization of an exciton Bose-Einstein condensate. On the contrary, the composite nature of excitons, exhibiting fermionic and bosonic features, offers a rich platform to explore novel collective quantum phenomena unaccessible to atoms. Furthermore, several challenges regarding the thermalization of excitons were overcome due to the progress in molecular epitaxial beam growth techniques. Thus, GaAs quantum wells allow for efficient cooling of exciton gases. However, the short radiative lifetime in quantum wells leads to the depletion of the exciton population before the gas is thermalized. An elegant solution to this obstacle was proposed by Lozovik and Yudson [59]. Their idea led to the development of biased heterostructures containing two coupled quantum wells separated by a barrier leading to a spatial separation between electrons and holes which form the exciton. This kind of excitons are called spatially indirect excitons or dipolar excitons due to their inherent electric dipole. As we will emphasize in this manuscript, coupled quantum wells allow for an unprecedented level of control over excitons, making the realization of a rich variety of potential landscapes and optoelectronic devices possible [3, 33, 35, 30, 39, 29, 68, 72].

These novel advances recently lead to remarkable, but controversial progress towards an excitonic BEC [37, 36]. For decades the manifestation of an excitonic BEC was believed to be detected in a very intense photoluminescence signal emitted from condensed bright excitons below some critical temperature. Thus, the condensation of excitons would manifest itself in a coherent photoluminescence signal, emitted from condensed bright excitons. This, however, doesn't take into account the composite nature of excitons. This fact was pointed out by Monique Combescot et. al. in 2007 for the first time [17, 18]: Excitons possess four distinct spin states, two bright states which can couple to light and two dark states which can not decay through radiative recombination and are energetically below the bright states [4, 10, 83]. Combescot et. al. demonstrated that repulsive inter-

band coulomb scattering, which exist only for bright excitons, are responsible for this energy splitting. This means Bose-Einstein condensation of excitons can not be observed through photoluminescence experiments alone, since it must occur in the dark states. However, Combescot et. al. were able to show that this is only true in a very dilute regime. At higher densities, in order to minimize its energy, the condensate acquires a bright component. This leads to the emergence of a bright part in the predominantly dark exciton condensate. Thus the condensate becomes "gray" and can be probed through its optically accessible bright component [21].

Recently, research groups have provided evidence for the dark-state condensation [75] and a build-up of coherence through the bright part of the gray condensate [2], below a critical temperature, by means of photoluminescence experiments. However, experimental results showing an unambiguous signature for a BEC of excitons is still missing. To this point a key challenge remains, namely the realization of a trapping potential allowing for the control of a constant exciton density at different temperatures, all other experimental parameters, i.e. excitation power and gate voltages, being kept unchanged. This would allow for comparable quantitative measurements of the evolution of the photoluminescence signal at different temperatures, which is necessary to demonstrate this high temperature phase transition

In this thesis we show that this degree of control is achieved by using a simple array of two gate electrodes to realize a trapping potential. Our experiments are based on a GaAs/AlGaAs coupled quantum wells embedded in a field-effect device. Spatially indirect excitons are injected into the trap by optical means and the population is studied through the exciton photoluminescence signal. We will show, that at 330 mK, the trapped exciton gas exhibits an anomalous darkening evidencing that bright and dark states are not equally populated, despite their splitting being negligible compared to the thermal activation energy. This darkening occurs in the dilute regime where excitons can be well described as bosons. Furthermore, we will introduce a new technique that allows for an arbitrary in-situ control of the potential landscape. State-of-the art techniques lead to undesired thermal heating due to energy dissipation in passive electrical components necessary to realize impedance matching. We will show that our technique stands in no way behind the current state of the art and does not lead to such undesired heating effects.

The thesis is structured as follows:

- Chapter 1 introduces key properties and concepts necessary to our studies

Introduction

of indirect excitons. Starting from exciton in bulk we will progressively introduce the steps leading to the formation of indirect excitons.

- In Chapter 2 we describe the phenomenon of Bose-Einstein condensation in general and discuss the challenges and constraints arising from the composite nature of indirect excitons. We also give a brief review of current developments in the area of Bose-Einstein condensation with indirect excitons.
- Chapter 3 discusses the experimental apparatus used for the studies discussed throughout the thesis. After introducing the experimental setup and control, we introduce our field-effect device containing the double quantum well. We elaborate the fabrication process of the device itself as well as the necessary simulations to fabricate a functional electrostatic trap for two dimensional indirect excitons.
- We demonstrate the versatility in terms of realizable trapping configurations in Chapter 4. Furthermore we discuss the influence of charges on the trap and quantitatively assess the stability of our trapping potential.
- In chapter 5 we show that our trapping technology allows for the controlled loading of indirect excitons with constant density below temperatures of 3.5 K without varying the excitation power which allows for comparable studies of the photoluminescence in terms of linewidth, blue shift and integrated intensity between different temperatures. These measurements allow us to show a non-classical distribution of the exciton population among the bright and dark states which can only be explained in the framework of Bose-Einstein Condensation.
- In chapter 6 we introduce a novel technique to control the exciton trapping potential in-situ. We show that this technique allows for an arbitrary control of the potential landscape. Using a customized printed circuit board in combination with coaxial cables for a cryogenic environment, we are able to control the trapping potential on the timescale of nanoseconds without any hazardous heating effects.

1 Excitons in Semiconductors

This chapter introduces the key properties and concepts necessary to describe indirect excitons in double quantum wells. As they have been extensively studied in the literature, we refer the interested reader to [70, 48, 31] for a more comprehensive review and introduction to the field of quantum well excitons. We begin by introducing the physical properties of excitons in bulk semiconductors and discuss the changes arising from a two dimensional confinement of excitons in quantum wells. We will then explain how the exciton lifetime can be extended and how we can exploit its electric dipole to trap a gas of excitons and deduce its density. Since the excitons investigated throughout this thesis are created by means of photo-excitation, we will conclude this chapter by reviewing the life cycle of spatially indirect excitons from photo-generation to their decay via radiative recombination.

1.1 Excitons in bulk Semiconductors

The irradiation of a semiconductor with light can lead to the creation of electron-hole pairs. The requirement on the incident photon is that its energy is greater than or equal to the band gap energy E_G , that separates the valence band from the conduction band (see figure 1.1). The photon absorption leads to the promotion of a valence-band electron to the conduction band, leaving behind an empty state in the valence band. This empty state is called a hole. Electron and hole are characterized by their effective masses m_e^* and m_h^* and their equal but opposite elementary charge. The electron and hole experience a mutual attractive Coulomb interaction and thus, they can form a bound state called an exciton as depicted in figure 1.1, similar to a metastable hydrogen-like bound state. Due to the large dielectric constant in most semiconductors the coulomb interaction is screened. This leads to a large Bohr radius for semiconductor excitons, which exceeds multiple lattice constants. In this regime the excitons are referred to as Wannier-Mott excitons.

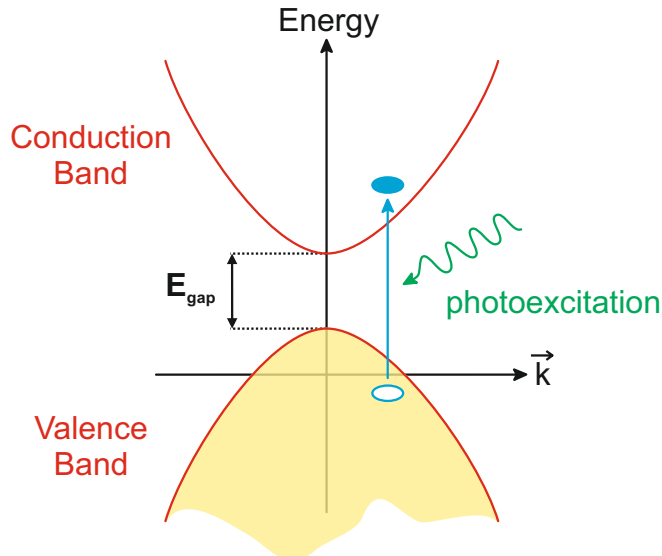


Figure 1.1: Photo-induced exciton generation process: The semiconductor absorbs a photon, which has an energy at least larger than the band gap E_G , thereby promoting an electron from the valence band to the conduction band. The empty state left behind in the valence band is called a hole and has a positive elementary charge. The attractive coulomb force between the electron and hole leads to the formation of a bound state which is called an exciton.

Wannier-Mott-Excitons are very similar to hydrogen atoms since they are both composed of two oppositely charged particles bound by the Coulomb force. This makes the calculation of the exciton eigenenergies quite convenient. One can simply use the solution for the hydrogen atom eigenenergies adapted to the case for the exciton. This means one has to use the effective electron and hole mass m_e^* and m_h^* and the effective reduced mass $\frac{1}{\mu} = \frac{1}{m_e^*} + \frac{1}{m_h^*}$ to calculate the eigenenergies. In addition one has to account for the semiconductor environment to correct the vacuum permittivity using the dielectric constant of the host crystal. Assuming isotropic and parabolic energy bands, this yields the following energy relation for excitons,

$$E_x = E_g + \frac{\hbar^2 k^2}{2M_x} - \frac{Ry^*}{n^2}, \quad n=1,2,3,\dots \text{ together with} \quad (1.1)$$

$$Ry^* = \frac{\hbar^2}{2\mu a_B^2} \quad (1.2)$$

$$a_B = \frac{\hbar^2 \epsilon_0 \epsilon_r}{e^2 \mu} \quad (1.3)$$

where E_g is the band gap energy, Ry^* is the exciton Rydberg energy, n the principal quantum number, μ the reduced exciton mass, ϵ_r the dielectric constant of the host crystal and a_B the exciton Bohr radius. For the excitons studied throughout this thesis the relevant parameters for GaAs are $\epsilon_r \approx 13$, $M_X \approx 0.22m_e$,

and $a_B \approx 10$ nm [77]. Another important property of the exciton is its spin. In order to quantify the spin of an exciton one has to consider the band structure of GaAs. The GaAs crystal lattice is described by a zincblende structure. In a zincblende structure the minimum of the lowest conduction band coincides with the maximum of the highest valence band at the Γ ($\vec{k} = 0$) point in the first Brillouin zone as depicted in figure 1.1. In GaAs this corresponds to the fundamental absorption edge. Valence band electrons possess p-like symmetry yielding a total angular momentum of $|J_p = \frac{3}{2}\rangle$ whereas the conduction band electrons possess s-like symmetry resulting in a total angular momentum $|J_s = \frac{1}{2}\rangle$. The spin-orbit interaction leads to a splitting in the valence band shifting light holes $|J = \frac{1}{2}\rangle$ below heavy holes $|J = \frac{3}{2}\rangle$. The bands show in general different curvatures, all of them away from the Γ point. In GaAs the different effective masses for electron, light hole and heavy hole are therefore $0.067m_0$, $0.08m_0$ and $0.5m_0$ respectively.

1.2 Excitons in 2D

By embedding a layer of GaAs between two layers of a material with a wider band gap, e.g. AlGaAs, excitons created in the GaAs layer remain confined there. Quasi 2D confinement of excitons can thus be achieved by reducing the thickness of the GaAs layer to a few nm. Such structures can be realized by means of standard molecular epitaxial growth techniques.

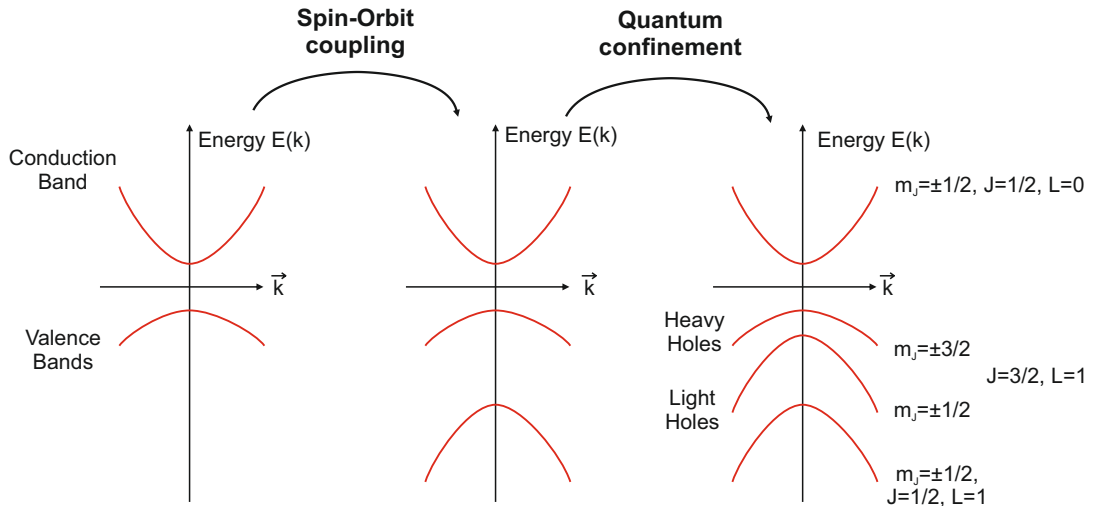


Figure 1.2: Energy bands for GaAs in 2D: In bulk spin-orbit coupling shifts the $|J = \frac{1}{2}\rangle$ states below the $|J = \frac{3}{2}\rangle$ states. The quantum confinement effect shifts the $m_J = \frac{1}{2}$ light holes below the $m_J = \frac{3}{2}$ heavy holes.

This configuration is referred to as Single Quantum Well (SQW). In a sufficiently narrow SQW the excitons motional degree of freedom along the growth axis

is quantized, which has a profound impact on the energy states. The reduced dimension along the growth axis compresses the electron and hole wave functions onto the quantum well plane, leading to a modification of the last term in equation (1.1) which describes the binding energy of the exciton. For 2D quantum wells with vanishing width, and infinite barrier height, this term reads:

$$-\frac{Ry^*}{\left(n - \frac{1}{2}\right)^2} \quad (1.4)$$

Thus, the binding energy of the exciton is increased. Another consequence of the confinement is the modification of the effective masses. While the hole masses remain similar to the bulk case along the growth direction, their masses along the quantum well are modified. This is described by the Luttinger Hamiltonian, which provides the effective masses near the Γ point [31]. For GaAs, the effective masses for heavy and light holes are $m = 0.11m_0$ and $m = 0.2m_0$ respectively.

As heavy and light holes have different effective masses, the band curvature is modified. This becomes immediately evident when one considers the confinement energy of a hole in a quantum well with infinite barrier height and width L which reads

$$E_n = \frac{1}{2m_h^*} \left(\frac{\hbar\pi n}{L} \right)^2 \quad (1.5)$$

where m_h^* is the effective mass of the hole. Equation 1.5 shows that the confinement energy scales inversely with the effective mass, giving rise to the different band curvatures for heavy and light holes. The confinement in 2D also leads to a degeneracy lift at the Γ point between the heavy and light hole as depicted in figure 1.2.

The increased binding energy is experimentally favorable since it improves the robustness against thermal ionization, for instance. However, the increased wave function overlap limits the lifetime of excitons due to the increased rate of the radiative decay [28].

1.3 Trapping spatially indirect excitons in coupled quantum wells

1.3.1 Increase of the exciton lifetime

The typical lifetime for excitons in GaAs is below 1 ns. It is comparable to the time it takes to thermalize hot photo-generated excitons to the lattice tempera-

1.3 Trapping spatially indirect excitons in coupled quantum wells

ture [42]. To observe collective quantum phenomena in a gas of excitons it would thus be desirable to work with excitons that have lifetimes significantly longer than the thermalization time. This is the case for spatially indirect excitons in coupled quantum wells (CQW) which have recently been of great scientific interest [14]. A coupled quantum well consists of two quantum wells separated by a barrier that allows for the tunneling of an electron between the two quantum wells. This approach can extend the exciton lifetime through an externally applied electric field parallel to the growth axis.

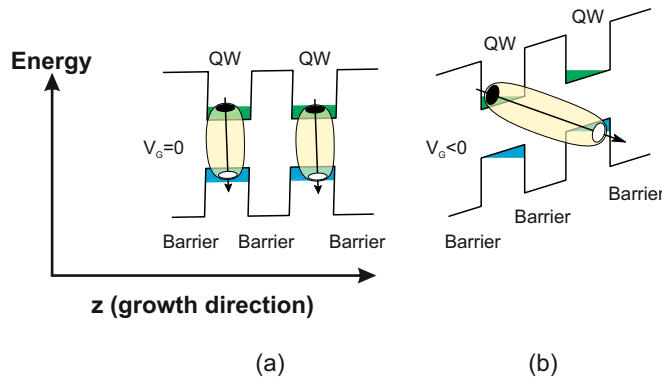


Figure 1.3: Band-Diagram of unbiased and biased coupled quantum wells: a) An unbiased pair of adjacent quantum wells forms a coupled quantum well populated with direct excitons in each well, the electron hole waveform overlap is large leading to short lifetime on the order of 1 ns. b) A biased coupled quantum well containing a spatially indirect exciton after the hole has tunneled to the adjacent quantum well in order to minimize its energy. In this case the waveform overlap is reduced, leading to much longer lifetimes of spatially indirect excitons compared to direct excitons.

A CQW is realized by combining two SQW's with an inter-well barrier. The inter well barrier has to be thin enough such that the coulomb interaction between electrons and holes can lead to a tightly bound exciton (see figure 1.3). By employing an electric field along the growth direction, the energy levels in the CQW become tilted, as depicted in figure 1.3b. A uniform electric-field along the growth axis is achieved by depositing large enough gate electrodes on the top and bottom surface of the CQW to apply a bias voltage V_G . The barrier between the coupled quantum wells has to be narrow enough to allow charges in the wells to be separated by means of carrier tunneling. Under an externally applied electric field the minimum energy states for electrons and holes lie in two different quantum wells. Hence, the electron and the hole of the exciton become spatially separated after a carrier has tunneled through the barrier to minimize its energy. In this configuration the exciton is referred to as spatially indirect exciton. Let us note that the spatial separation imposed between electrons and

holes leads to an exponential reduction of the electron-hole wave function overlap thus leading to increased lifetimes of indirect excitons of up to microseconds [85]. In this configuration, the excitons have sufficient time to cool down to the lattice temperature, allowing one to study a gas of cold excitons.

1.3.2 The exciton dipole

Excitons in general and therefore also spatially indirect excitons possess an inherent dipole moment \vec{d} due to their oppositely charged constituents. Hence, spatially indirect excitons in particular are subject to an interaction between the exciton dipole and the electric field present in the quantum well. In the case of indirect excitons dipole-field interaction reads

$$U_{dip} = -\vec{d}\vec{E}_{ext} \quad (1.6)$$

where \vec{E}_{ext} denotes the uniform externally applied electric field, parallel to the growth axis, in the field effect device embedding the CQW (see figure 1.4). The dipole interaction U_{dip} causes the exciton dipole to orient itself along the growth axis. In order to minimize their energy the dipoles will always align themselves parallel to the electric field. Therefore, because of $U_{dip} < 0$, the contribution of the dipolar interaction is always negative, which causes a red shift of the photoluminescence energy. Indirect excitons are also subject to a repulsive dipole-

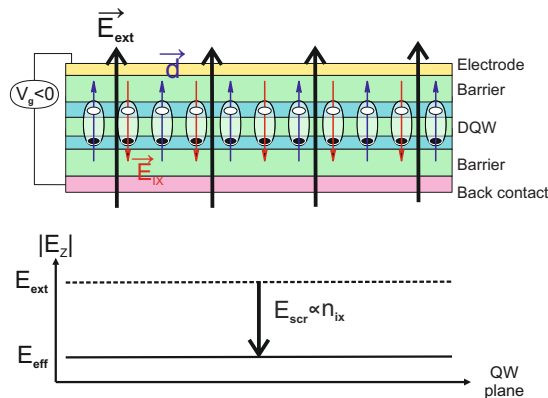


Figure 1.4: The exciton dipoles (blue arrows) are always parallel to the externally applied electric field \vec{E}_{ext} . Thus every dipole creates an antiparallel oriented field \vec{E}_{IX} leading to a screening field. The screening field reduces the externally applied electric field (dashed line) leading to an effective electric field that is smaller than the externally applied field. The screening scales with the indirect exciton density n_{IX} .

dipole interaction U_X , since the individual dipoles of the excitons align themselves

1.3 Trapping spatially indirect excitons in coupled quantum wells

parallel to the electric field \vec{E}_{ext} as shown in figure 1.5a. This is favorable to study dense gases since it prevents the exciton gas from forming excitonic molecules, i.e. bi-excitons. The dipole-dipole interaction also modifies the photoluminescence. Since it is repulsive it causes a blueshift of the emission spectrum as the density of the gas increases. The blueshift can be approximated in a basic manner by using the plate capacitor approximation which computes the screening of the internal electric field by the carriers confined in the CQW. Following this approach gives

$$U_X = \frac{4\pi e^2 d}{\epsilon_b} n_{IX} \quad (1.7)$$

where n_{IX} is the density of indirect excitons and d the distance between the quantum well centers [40]. However equation (1.7) is not fully suitable to determine

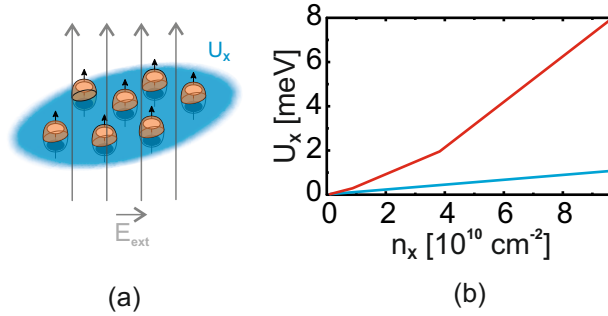


Figure 1.5: Exciton Density and Photoluminescence Energy: a) A gas of indirect excitons with parallel electric dipoles are subject to repulsive exciton-exciton interaction. b) Blue shift of the photoluminescence energy U_X calculated using the plate capacitor formula (blue) and by including inter-exciton interactions (red) using the model provided in [43]. The bath temperature is set to 340 mK.

the density of a gas of indirect excitons since it neglects the role of the repulsive exciton-exciton interaction onto the photoluminescence energy. Theoretical studies have been carried out to include this effect. We will refer to the method described in [43], which considers also exciton-exciton interactions, to extract the exciton density from the photoluminescence energy. Figure (1.5)b shows the variation of the blueshift for spatially indirect excitons using the plate capacitor formula and the method outlined in [43]. One can see that the plate-capacitor formula underestimates the density by at least an order of magnitude. At this point it must be mentioned that a theoretical model which links the blueshift to the exciton density is still an area of active research and subject to strong debates in the field [43].

1.3.3 Electrostatic traps for spatially indirect excitons

By exploiting the dipolar nature of indirect excitons it is possible to tailor customized potential landscapes which they can explore. This approach has led to the development of exciton traps and devices like exciton conveyors, exciton based circuits or artificial quantum dots [72, 38, 39, 68, 67, 81]. The key idea behind this technology is depicted in figure (1.6) where a sample containing a CQW is placed in an electric field aligned along the z -axis. The electric field is spatially inhomogeneous. In this case we assume two local minima with a field maximum in the middle ($|E_1(x_1)| = |E_3(x_3)| < |E_2(x_2)|$). According to equation (1.6) the dipole energy is the smallest where the electric field is the strongest. The exciton will therefore be subject to a force gradient which is oriented towards the local maximum of the electric field. Since excitons always tend to move towards the point where the electric field magnitude is the highest they are also called high-field seekers.

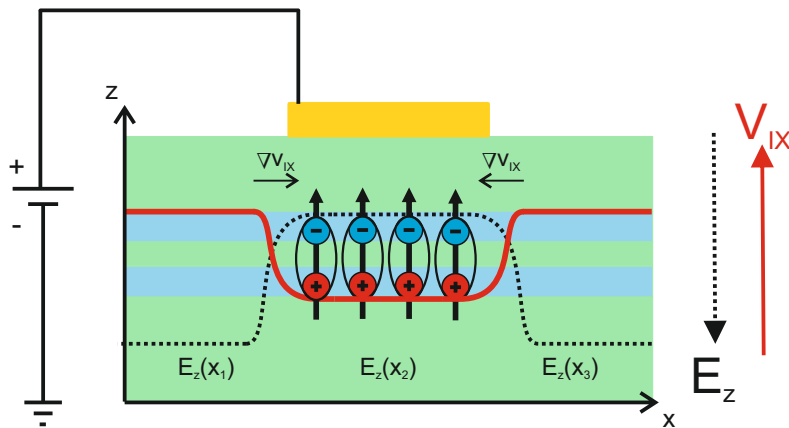


Figure 1.6: Excitons in a spatially inhomogeneous electrical field. The field is created by a gate electrode on top of the field effect device containing the coupled quantum wells. Excitons, being high-field seekers, will accumulate in the region where the z -component of the electric field is the largest in order to minimize their energy.

As a part of this thesis such a trapping potential has been realized by engineering gate electrodes on a field-effect device that embeds the CQW. This method offers multiple options to manipulate the confinement and dynamics of indirect excitons. The electric field is realized by applying bias voltage to the gate electrodes that enclose the field effect device. This allows for an in-situ control of the force gradient acting on the excitons, the depth of the trapping potential or the transition from indirect excitons to direct excitons by setting the electric field to zero [88]. Using metallic gates on top of the sample allows for a high degree of flexibility in terms of the trapping geometry by using lithographic fabrication methods.

1.4 Formation and decay of spatially indirect excitons

The resulting field distribution in a double quantum well, induced by the electric contacts, can be simulated before the device is fabricated by using commercially available finite-element based simulation software for stationary electromagnetic fields, like Comsol Multiphysics or nextnano. Several devices ranging from an exciton conveyor to an exciton based transistor have been realized by exploiting the exciton dipole-field interaction. The speed at which these devices operate is limited by the RC time constant of the circuit, consisting of voltage source, electrical wires and the field-effect device. It typically lies in the range of ms [87].

Exciton ionization by in-plane electric fields

The finite size of the gate electrodes naturally leads to the emergence of radial field components, perpendicular to the growth axis, which can lead to the ionization of excitons. It is thus necessary that the in-plane electric field \vec{E}_r remains smaller than the exciton binding energy of $E_B \sim 4 \text{ meV}$ [77] which is expressed by the following inequality

$$a_B e |\vec{E}_r| < E_B \quad (1.8)$$

and gives an approximation of the critical threshold for \vec{E}_r where exciton ionization occurs:

$$|\vec{E}_r| \stackrel{!}{<} ||\vec{E}_{critical}|| = \frac{E_B}{a_B e} \sim 4 \cdot 10^5 \frac{V}{m} \quad (1.9)$$

This criteria is of fundamental importance for all electrostatic exciton traps and devices since in-plane electric fields are inherent to all finite-size gate contacts and particularly strong near the electrode edges. To prevent this malicious effects, the CQW can be positioned close to the bottom electrode at a distance of around 100 nm while its distance to the top electrode is 10 times larger, where ionization effects are most likely to occur since the in-plane electric fields are strongest in magnitude near the edge of the surface electrodes [68]. We have followed these design constraints for the traps developed as part of this thesis and discuss them further in chapter 3.

1.4 Formation and decay of spatially indirect excitons

Having introduced the properties of direct and indirect excitons we can now discuss the full life cycle of spatially indirect excitons from photogeneration to their decay via radiative recombination. Spatially indirect excitons created by

photo-excitation are either created through an excitation resonantly tuned to the direct exciton transition energy of the 2 quantum wells or a non-resonant excitation tuned above the band gap of the AlGaAs barrier layers. Both processes are depicted in figure 1.7a.

By using a resonant excitation one injects direct excitons in the quantum wells in the lowest energy states of the direct exciton band. This is favorable since these direct excitons can then transform to high momentum indirect excitons, as depicted in figure 1.7b, once the carriers have tunneled through the barrier and relaxed to their respective subbands. However the laser excitation also leads to the absorption of photons in the n-doped layer, used as a back-contact of the field effect device (see figure 1.7a). This can lead to unwanted modifications of the electrostatic confinement due to captured charges that can either screen or reinforce the externally applied field as shown in figure 1.7c. The non-resonant excitation on the other hand leads to the creation of high energy electron hole pairs throughout the barriers in the heterostructure. These carriers relax to their respective subbands via the emission of longitudinal phonons or many-body scatterings. When these charges are captured in the quantum wells they can form direct excitons once the coulomb attraction becomes dominant. As in the case for the resonant excitation they can then transform to high momentum spatially indirect excitons. These excitons possess a high kinetic energy and relax through several mechanisms, namely inter-exciton, exciton-free carrier and exciton-acoustic phonon scattering until they are thermalized to the bath temperature of the host crystal. One can see directly that the resonant excitation provides a much more controlled approach to create indirect excitons since the amount of excess charges that can potentially remain trapped in the field effect device is greatly reduced compared to the non-resonant excitation. Like in the case for the resonant excitation, also here free charges can become trapped at the hetero-interfaces, thus, altering the potential experienced by spatially indirect excitons.

Once the excitons are cold enough, which means $\vec{k}_{\parallel} \approx 0$, they can recombine via the emission of a photon. Let us note that the 2D confinement of excitons relaxes the momentum conservation rule along the growth axis. As a result the thermalization of excitons to the lattice temperature via emission of bulk longitudinal acoustic phonons is 3 orders of magnitude more efficient compared to excitons in bulk [42, 41]. In order for an exciton to decay via radiative recombination it needs to be able to couple to the photon field. Thus energy and momentum need to be conserved during the recombination process. Due to this constraint the radiative decay is only allowed for excitons inside the light cone. In the following we derive an analytic solution for this threshold. The energy of an exciton confined in a

1.4 Formation and decay of spatially indirect excitons

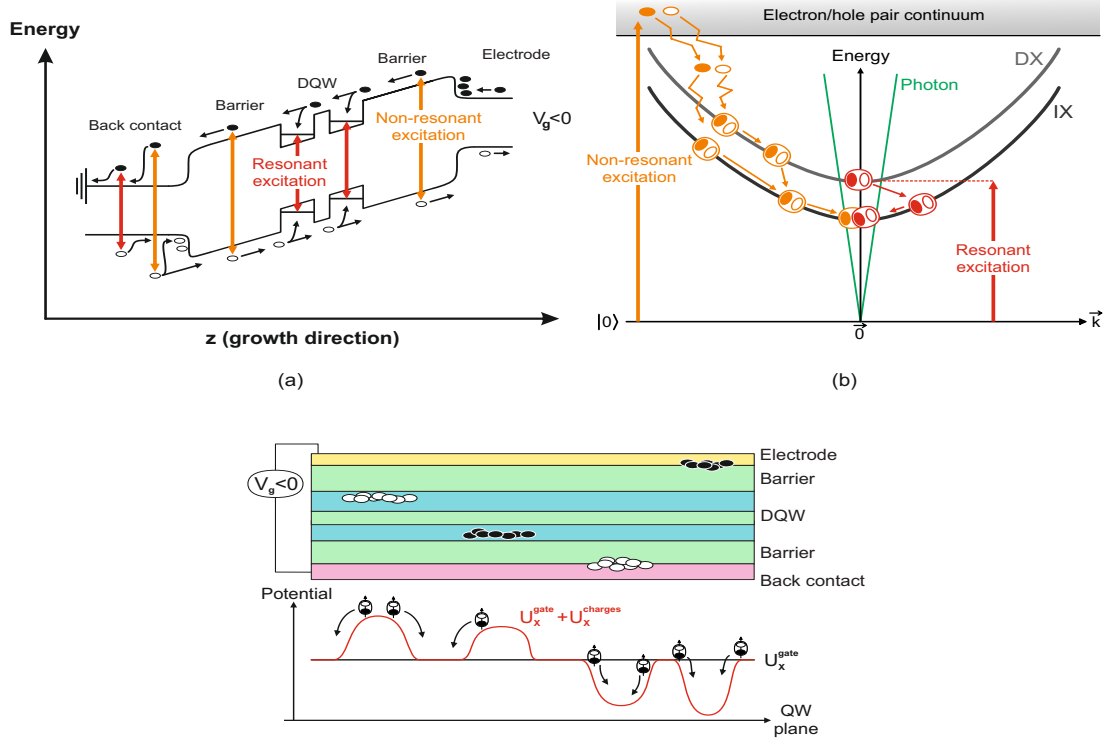


Figure 1.7: Photogeneration process of excitons: a) Band diagram of the field effect device showing that the non-resonant excitation (orange) leads to the creation of free charges throughout the field effect device. Exciton formation then relies on the quantum wells capability to efficiently capture these free charges. In case of an excitation resonantly tuned to the direct exciton transition (red) carriers are mainly created in the adjacent quantum wells. b) Energy diagram with dispersion relations for direct as well as spatially indirect excitons (black) and the photon dispersion (green). The non-resonant excitation (orange) creates free high energy carriers that form direct and indirect excitons while the resonant excitation (red) injects direct excitons at the lowest energy state of the direct exciton band allowing for the formation of spatially indirect excitons. c) Effect of free charges on the applied electric field: Free electrons (black circles) and holes (white circles) can become trapped at the hetero-interfaces leading to a modulation of the otherwise homogeneous potential explored by the excitons

quantum well can be written as

$$E_X = E_G + E_n - E_B + \frac{\hbar k_{\parallel}^2}{2M_X} = E_0 + \frac{\hbar k_{\parallel}^2}{2M_X}, \quad (1.10)$$

E_B being the binding energy due to the coulomb force, and k_{\parallel} the in-plane exciton momentum. The Energy E_{Ph} of a photon in the crystal is written as

$$E_{Ph} = \hbar \frac{c}{n} \left\| \vec{k}_{ph} \right\| = \hbar \frac{c}{n} \sqrt{k_{\parallel}^2 + k_{\perp}^2} \quad (1.11)$$

where \vec{k}_{ph} is the photon momentum, k_{\perp} the momentum along the growth axis

1 Excitons in Semiconductors

and n the index of refraction in the crystal. Imposing $E_{ph} = E_X$ yields

$$k_{\perp} = \sqrt{\frac{n^2}{c^2\hbar^2} \left(E_0 + \frac{\hbar k_{\parallel}^2}{2M_X} \right)^2 - k_{\parallel}^2} \quad (1.12)$$

which gives a real root only for

$$k_{\parallel}^2 < \frac{n^2}{c^2\hbar^2} \left(E_0 + \frac{\hbar k_{\parallel}^2}{2M_X} \right)^2 \quad (1.13)$$

The two solutions for this inequality are

$$k_{\parallel,1} \stackrel{!}{<} \frac{cM_X}{n\hbar} \left(1 - \sqrt{1 - \frac{2n^2 E_0}{c^2 M_X}} \right) \quad (1.14)$$

$$k_{\parallel,2} \stackrel{!}{>} \frac{cM_X}{n\hbar} \left(1 + \sqrt{1 - \frac{2n^2 E_0}{c^2 M_X}} \right) \quad (1.15)$$

The second solution leads to values of k_{\parallel} beyond the first Brillouin zone. Therefore only excitons with an kinetic energy lower than $\Delta E = \frac{\hbar k_{\parallel,1}^2}{2M_X}$ can decay via radiative combination and define the light cone as depicted in figure (1.7). For our experiments with a typical emission wavelength around 1519 meV, $n=3.6$ for GaAs and $M_X = 0.2m_e$, we get $\Delta E = 150 \mu eV$.

2 Bose-Einstein-Condensation of excitons

The peculiar nature of macroscopical quantum systems and their behavior, e.g. superconductivity and superfluidity, led to a set of remarkable experiments on dilute alkali gases in the 90's [12]. In 1924 Satyendra Nath Bose published a paper in which he derived Planck's law of black body radiation [13]. Albert Einstein extended the concepts of Bose's work and formulated his quantum theory of the mono-atomic ideal gas of bosons. He realized the peculiarity of this theory which is nowadays known as the Bose-Einstein statistics. Einstein notably postulated that at a low but finite temperature the energetic ground state would experience a macroscopic occupation, a Bose-Einstein condensate (BEC) would form. The experimental realization of this prediction in 1995 is an extraordinary contribution to fundamental research which was awarded with the Nobel prize in 2001 to E. Cornell (NIST), C. Wiemann (NIST) and W. Ketterle (MIT).

The concept of a Bose-Einstein condensate was first used in an attempt to explain the superfluidity in liquid ^4He by London and Tisza [58, 82]. It turned out that superconductivity and superfluidity are phenomena related to Bose-Einstein condensation despite their occurrence in a liquid state unlike the prediction of BEC in an ideal gas.

Like atoms, excitons were long considered promising candidates to demonstrate Bose-Einstein condensation, after Keldysh and Kozlov could show in 1968 that the exciton made up of two fermionic constituents obeys Bose statistics in the dilute limit [45]. Since excitons in GaAs have a mass of approximately $0.22m_e$, the condensation occurs below a critical temperature which can be on the order of a few Kelvin. This makes the experimental search for BEC a priori much easier than for atomic vapors. Nevertheless, unambiguous signatures for a BEC of excitons are still missing, whereas atomic condensates are nowadays well established. In this chapter we will review only basic concepts of Bose-Einstein condensation since the topic is extensively covered in numerous textbooks and review papers [66, 23, 55]. We elaborate the constraints and challenges imposed when trying to

create a BEC of excitons and furthermore review the latest advances towards a BEC of excitons.

2.1 Basic theory of BEC

In statistical physics all elementary particles can be sorted into one of two groups, which, depending on their spin, obey two fundamentally different statistics.

- A particle with half integer spin, like e.g. an electron, is called a fermion. For fermions, one particular quantum state can be occupied by maximally one fermion at a time due to the Pauli exclusion principle. This is due to the fact that N fermions represented by the wave function Ψ must be antisymmetric when interchanging two particles k and l with $\{k, l\} \in \{1, \dots, N\}$ according to the spin statistic theorem [63]. Thus, a gas of fermions in thermodynamic equilibrium obeys the Fermi-Dirac statistics

$$P_{FD}(E) = \frac{1}{e^{\left(\frac{E-\mu}{k_B T}\right)} + 1} \quad (2.1)$$

where P_{FD} describes the occupation probability for a particle with energy E at a given Temperature T and k_B being the Boltzmann constant.

- A particle with integer spin is called a boson. Bosons are fully symmetric under particle exchange and therefore not subject to the Pauli exclusion principle, thus, allowing the occupation of one particular quantum state by an arbitrary number of bosons. This is of fundamental importance in the context of Bose-Einstein condensation as we will see later. In thermodynamic equilibrium bosons obey the Bose-Einstein statistics

$$P_{BE}(E) = \frac{1}{e^{\left(\frac{E-\mu}{k_B T}\right)} - 1} \quad (2.2)$$

It is interesting to note that unlike for the case of fermions, matter bosons are only found in a composite form. This means they are always made of an even number of fermions. As a consequence composite bosons obey the relation in equation (2.2) only when the effects of the fermionic constituents can be neglected [20, 19].

Equation (2.2) allows us to study the thermodynamic properties of a non-interacting bosonic gas at low temperatures. In particular we are now able express the total

number of particles as

$$\begin{aligned} N &= \int_0^\infty P_{BE}(E) dN &&= \int_0^\infty \frac{1}{e^{\left(\frac{E-\mu}{k_B T}\right)} - 1} dN \\ &= \int_0^\infty P_{BE}(E) D(E) dE &&= \int_0^\infty \frac{1}{e^{\left(\frac{E-\mu}{k_B T}\right)} - 1} D(E) dE \end{aligned} \quad (2.3)$$

where the density of states for unconfined systems is given by

$$D(E) = \frac{dN}{dE} \propto E^{\frac{d}{2}-1} \quad (2.4)$$

and d denotes the dimension of the system. In equation (2.3) we can see that $\mu \leq 0$ must hold at all times. If not $P_{BE}(E)$ would become negative for energies E smaller than the chemical potential μ , which is unphysical. In the case of a Bose gas in 3D we find by setting the chemical potential to the upper limit of $\mu = 0$ and $D(E) \propto \sqrt{E}$, a maximum density of

$$n_c = \frac{N_c}{V} = 2.612 \left(\frac{mk_B T}{2\pi\hbar^2} \right)^{\frac{3}{2}} \quad (2.5)$$

In equation (2.5) we note that when the maximum density is reached and the temperature is lowered further, the particles can not longer be properly described by the Bose-Einstein distribution. Therefore it can not be an universal description for all particles at any given temperature. Einstein realized this and postulated that in the thermodynamic equilibrium, above this maximum density, all excess particles have to condense into the ground state of the system, which then has to be treated separately from the non-condensed part [25]. Equation (2.5) therefore describes the critical density n_c for a given temperature T above which a macroscopic population of the ground state takes place. This macroscopic occupation of the ground state is called a Bose-Einstein condensate. Vice-versa it also defines the critical temperature T_c below which for a given constant density Bose-Einstein condensation occurs.

A more intuitive approach of BEC can be acquired by considering the wave nature of bosons. By defining their average energy at a given temperature T by $E = \frac{p^2}{m} \approx k_B T$, where p is the boson momentum, we can derive their thermal wavelength, known as the de-Broglie wavelength:

$$\lambda_{dB} = \frac{2\pi\hbar}{p} = \frac{2\pi\hbar^2}{\sqrt{2\pi mk_B T}} \quad (2.6)$$

A rule of thumb is that Bose-Einstein condensation occurs when the de-Broglie wavelength becomes comparable to the interparticle distance. In this case the single particle wave functions start to overlap. In this regime we can not describe

2 Bose-Einstein-Condensation of excitons

the particles as a collection of independent particles but rather as a single quantum state as depicted in figure 2.1. Following this methodology we can compare the inter-particle distance to λ_{dB} and estimate a critical temperature for BEC at a given temperature. Equation (2.6) shows the de-Broglie wavelength diverges as the temperature is lowered towards absolute zero suggesting the appearance of a single giant-matter wave, a pure Bose-Einstein condensate.

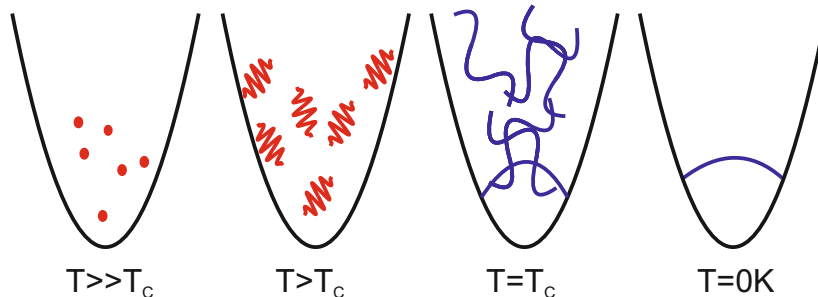


Figure 2.1: Matter Wave picture of a BEC in a harmonic trap: As the temperature is decreased towards the critical temperature the de-broglie wavelength increases. At $T = T_C$ the inter particle distance is becoming comparable to the de-Broglie wavelength of the trapped bosons and , leading to a macroscopic occupation of the ground state in a trap, a BEC..

At last, let us note that the critical temperature does not only depend on the gas density. Since the density of states $D(E)$ is dimension dependent, the exact form of the critical temperature depends on the dimension and trapping geometry of the system under consideration. We give an overview of the critical temperatures depending on the geometry of the system in table 2.1.

| Confinement | 2D | 3D |
|--------------|--|--|
| free | No BEC | $T_c \approx 3.31 \frac{\hbar^2}{mk_B} n^{\frac{3}{2}}$ [47] |
| harmonic | $T_c \approx \sqrt{6N} \frac{\hbar\omega}{k_B\pi}$ [23] | $T_c = 0.94 \frac{\hbar\omega}{k_B} N^{\frac{1}{3}}$ [47] |
| quantum well | $T_C = \frac{4\pi\hbar^2 n}{mgk_B} \frac{1}{\ln(\frac{nS}{g})}$ [47, 14] | $T_c = 3.31 \frac{\hbar^2}{mk_B} n^{\frac{3}{2}}$ [57] |

Table 2.1: Critical Temperatures T_c depending on the density n or particle number N , for bosons with mass m .

2.2 Bose-Einstein condensation of spatially indirect excitons

A very dilute gas of rubidium atoms has to be typically cooled down to the order of nanokelvins to observe the BEC transition with typical atom numbers

2.2 Bose-Einstein condensation of spatially indirect excitons

on the order of $N_{atom} \approx 1000$ and characteristic trapping frequencies on the order of 100 Hz for a 2D confinement geometry [71]. To reach it sophisticated cooling methods such as, laser cooling, evaporative cooling combined with optical trapping were used to bring an ensemble of atoms to the quantum regime. As we can see from the equation for a harmonic trapping potential in table (2.1), the critical temperature scales with the trapping frequency and atom number. Due to the low exciton mass, which is 6 orders of magnitude lower than for rubidium, trapping potentials on the order of GHz are easily achievable[86]. Assuming typical exciton densities on the order of $n_{IX} \approx 10^{10} cm^{-2}$, typical exciton numbers in electrostatic traps are, as in the case for atoms on the order of $N_{IX} \approx 10000$ as in the case for atoms. Thus, the critical temperature is expected to be on the order of Kelvins. This temperature range can be easily reached using standard cryogenic equipment. Creating a BEC of excitons then mainly requires to cool a gas below a few Kelvin at a density of $n_X \approx 10^{10} cm^{-2}$. This density condition imposes quite clean constraints:

- The fermionic nature of the exciton must be negligible such that they can be treated as bosons.
- Excitons must be experience repulsive interactions to form an excitonic ground state at high enough densities.
- Excitons must be long lived in order to be able to efficiently thermalize to the lattice temperature below a few kelvins

Additionally, to achieve a BEC of excitons, we need to fulfill the requirements listed in table 2.1. It shows the temperature and density requirements that need to be met. Particularly in two dimensions, which is the geometry studied in this thesis. With special regard to BEC, let us now consider the consequences arising from the excitons fermionic nature, their finite lifetime, their thermalization properties and their two dimensional confinement in a coupled quantum well structure.

- Bosonic vs Fermionic Nature: Excitons are composite bosons made up of two fermionic particles, an electron and hole. It is thus necessary to show when the description of excitons as bosons is a valid one. A naive estimate is that the average inter-particle distance is larger than the exciton Bohr radius which gives $n_{IX} a_B^2 < 1$, where n_{IX} is the exciton density. However this neglects the influence of the underlying fermionic as pointed out by combescot and coworkers. When included, the criterion becomes $5n_{IX} a_B^2 \ll 1$, which gives an upper limit for the exciton density of $n_{IX} \approx 10^{10} cm^{-2}$ [20].

2 Bose-Einstein-Condensation of excitons

- **Finite Lifetime:** First of, excitons being elementary excitations of a semiconductor, are quasi particles composed of an electron and hole. In the same way that excitons can be created through photon absorption, they decay through radiative electron hole recombination which yields a finite radiative lifetime. For GaAs quantum wells this lifetime is typically on the order of 100 ps , too short for the excitons to thermalise to the lattice temperature, since the thermalisation time lies on the order of ns. This obstacle is overcome in coupled quantum wells, as introduced in Chapter 1. In GaAs coupled quantum wells, as studied in this thesis, the indirect excitons created, have lifetimes ranging from a few tens of ns to over $30\ \mu\text{s}$, as electrons and holes are spatially separated in adjacent quantum wells. This is much longer than the theoretically predicted thermalisation time of approximately 1 ns in these systems and it is reasonable to assume, given no other heating sources, that spatially indirect excitons are in thermal equilibrium with the host lattice.
- **Fast thermalisation:** Photo-injected excitons have to quickly cool down to lattice temperatures below a few Kelvins. In contrast to excitons in a bulk semiconductor where exciton thermalisation is not efficient, excitons confined to 2D rapidly cool through interacting with longitudinal-acoustic phonons. Since the momentum conservation condition is relaxed along the growth axis, the exciton ground state can couple to a continuum of phonons which satisfy the condition $E \geq 2mv_s^2$. In the 3D case only the coupling to the mode $E = 2mv_s^2$ would be permitted, where m is the exciton mass and v_s the speed of sound of sound in GaAs [42].
- **Two-Dimensional Confinement:** As we have seen in table 2.1, BEC does not occur in an infinite 2D system. A non-confined gas of bosons in 2D will undergo a transition towards a superfluid known as the Berezinsky–Kosterlitz–Thouless (BKT) Transition. This phase is also characterized by the macroscopic population of the ground state. However, thermal fluctuations at any finite temperature lead to the destruction of true long range order [49, 32], thus making a confinement of the gas necessary. This is a condition which can be easily met with indirect excitons, as we have shown that their interaction with a spatially non-uniform electric field provides a direct route to control their spatial confinement. We will discuss this further in chapter 3, where we introduce the design of our trap.
- **Oriented electric dipole:** Spatially indirect excitons exhibit a electric dipole oriented perpendicular to the quantum well plane. As a result, indirect ex-

citons experience repulsive dipole-dipole interactions which prevent the formation of bi-excitons. In addition, the repulsive interactions between indirect excitons shift their photo-emission towards higher energies, a blueshift, which enables one to estimate the exciton density as discussed in subsection 1.3.2.

2.3 The dark condensate - The role of the spin

The role of the spin deserves special attention in the quest for a BEC of excitons. An exciton composed of an electron hole pair inherits its spin from its constituents. For the conduction band electron we have $m_{J,e} = \pm\frac{1}{2}$ whereas the valance band hole has a spin of $m_{J,h} = \pm\frac{3}{2}$. As a consequence the excitons can be in 4 distinct spin states.

$$S = |\pm 1\rangle = \left| m_{J,e} = \mp\frac{1}{2}, m_{J,h} = \pm\frac{3}{2} \right\rangle \text{ (Bright States)}$$

$$S = |\pm 2\rangle = \left| m_{J,e} = \pm\frac{1}{2}, m_{J,h} = \pm\frac{3}{2} \right\rangle \text{ (Dark States)}$$

The $S = \pm 1$ states are referred to as bright states since they can directly couple to σ^\pm polarized light. On the other hand, the dark states, with $S = \pm 2$, can not couple to light. Thus, excitons created through photo-excitation are initially all bright. Bright to dark state conversion takes place through individual carrier spin flips or through carrier exchange between two bright excitons. The same holds true for the conversion of a dark to a bright exciton as depicted in figure 2.2. To understand the formation of the exciton BEC in coupled quantum wells it is

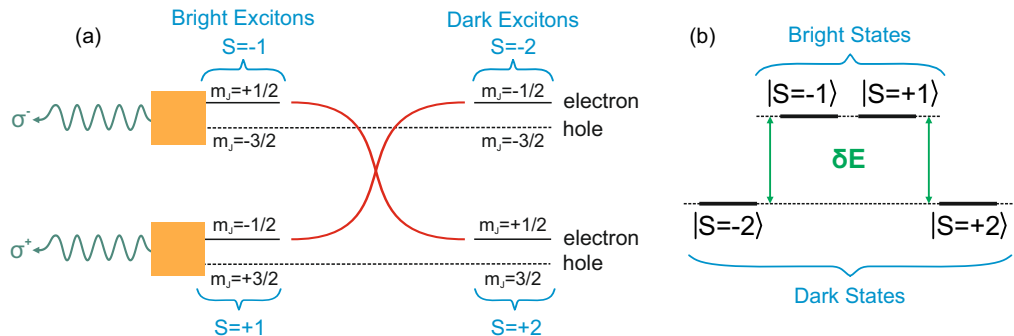


Figure 2.2: a) Schematic of the Bright-Dark conversion processes due to carrier exchange processes. The bright states $|\pm 1\rangle$ decay with polarization σ^\pm respectively. b) Illustrating the shift of bright states ($S = \pm 1$) above the dark states ($S = \pm 2$) due to the repulsive interband coulomb scattering for bright excitons.

fundamental to realize that, contrary to the consensus at the time, the four spin

2 Bose-Einstein-Condensation of excitons

states are not degenerate. This was recently demonstrated by M. Combescot and co-workers who were able to show that interband coulomb scattering processes shift the energies of bright excitons above the dark states. This process is described by the absorption and emission of a virtual photon, which only exists for bright excitons, since they are the only ones who can couple to light. The repulsive nature of these interband scatterings shifts the bright states energetically above the dark ones [17]. For a GaAs double quantum well this energy splitting is on the order of $5 \mu\text{eV}$ [10]. However, since BEC is defined as the macroscopic occupation of the ground state, the condensation must occur in the dark state, regardless of how small the energy splitting might be. These results stood in direct conflict with the search for coherence from a bright photoluminescence peak at the bottom of a trap as reported in previous experiments[36, 37]. Nevertheless, in a subsequent publication Combescot and co-workers were also able to show that under a density increase the carrier exchange between two dark excitons, i.e. the exchange of an electron or hole (see figure 2.2a), should lead to a population of bright states that are coherently coupled to the otherwise fully dark condensate. This bright part should then be observable through photoluminescence experiments. The term “gray condensate” has been introduced to highlight the interplay between the dark and bright part that constitute the condensate in this density regime [21].

2.4 Advances towards the realization of an exciton BEC

Macroscopically ordered state in an exciton system

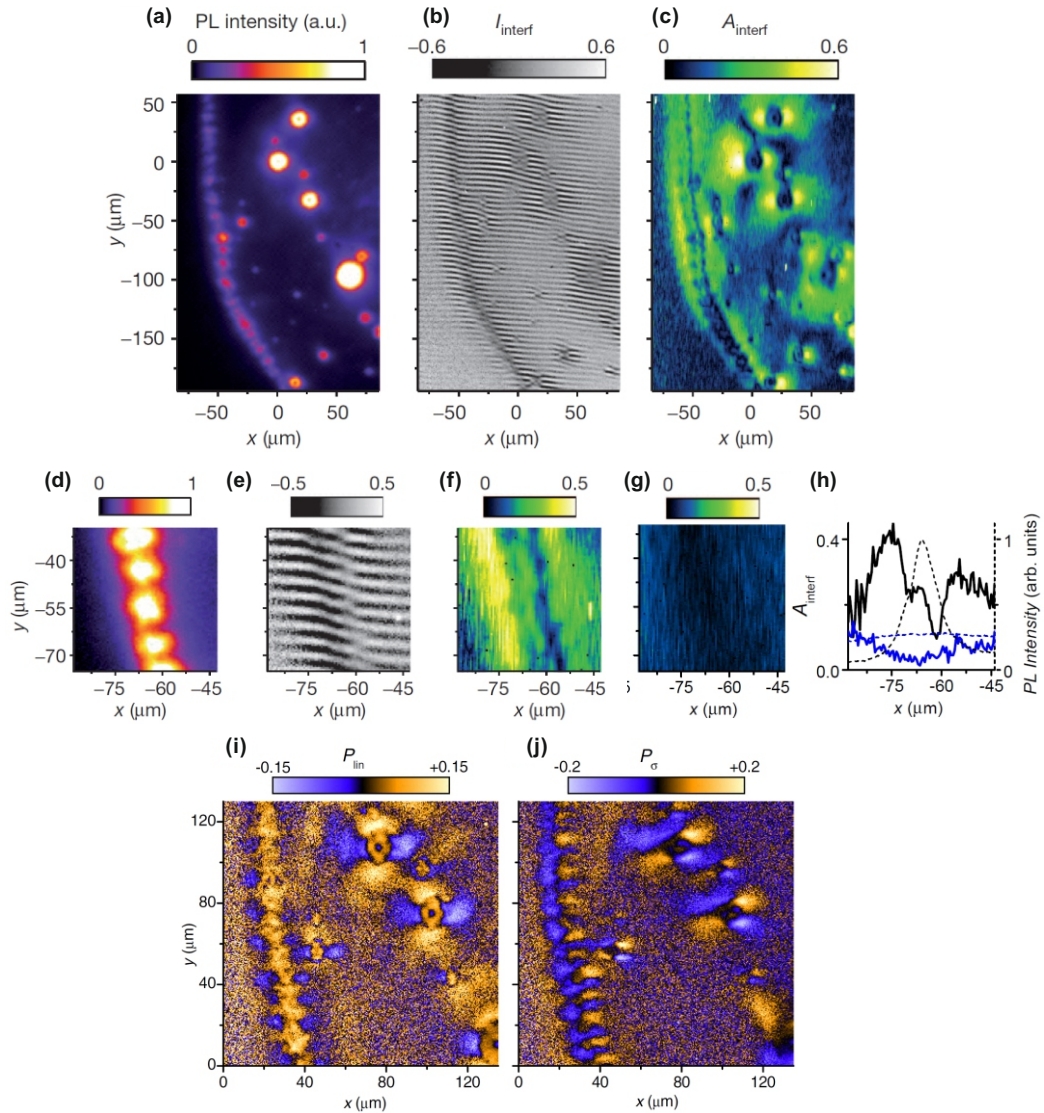


Figure 2.3: a) Luminescence emission pattern. b) Shift-Interferogram, normalized, with a lateral shift of $\delta x = 2\mu\text{m}$. c) Coherence amplitude map of the luminescence. d-f) close up of a-c). g) Coherence map same as f) taken at high temperature. h) Variation of the Intensity (dashed lines) and the contrast (solid lines) along a bright fragment along the x -axis at 0.1K and 8K (black and blue line respectively). Images taken from.

In 2011 High et al. reported on spontaneously established spatial coherence in the luminescence signal of a cold gas of non-resonantly photo-injected indirect excitons, cooled below a critical temperature of around 2 K. Quite remarkably,

2 Bose-Einstein-Condensation of excitons

the coherence length of the gas was extended over $15 \mu\text{m}$ near localised bright spots of a macroscopic fragmented ring, as shown in figure 2.3. This is about two orders of magnitude larger than the de-Broglie wavelength, assuming a temperature of 1 K , an exciton density of $n_X = 10^{10} \text{ cm}^{-2}$ and an exciton effective mass of $0.2 m_e$. This observation was interpreted as a signature for a coherent exciton state with a non-classical momentum distribution [36]. Extended spatial coherence was observed together with spontaneous polarization patterns which lead High et. al. to conclude that they observed a multi-component spinor exciton condensate. Let us note that extended coherence occurs only in regions where the intensity of the photoluminescence signal is very weak. This suggests that this exciton condensation is dominated by a macroscopic population of dark excitons which has not been discussed by the authors.

Condensation of excitons in a trap

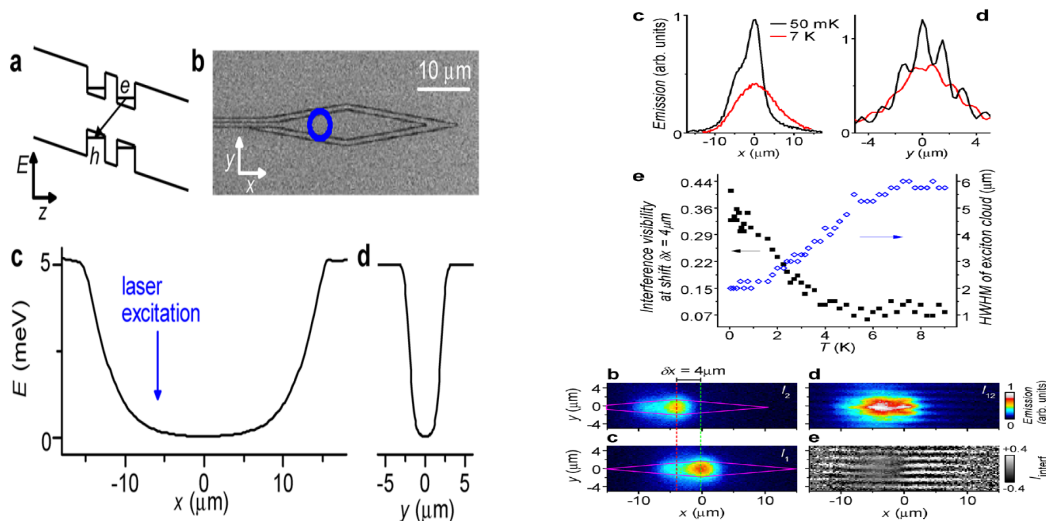


Figure 2.4: Experimental results performed in a a) diamond shaped trap with remote laser excitation showing b) an increased interference visibility as the bath temperature is lowered together with a contraction of the exciton cloud. Images taken from [37]

In 2012 the same authors (High et. al.) reported on extended spatial coherence for an exciton gas confined in an electrostatic trap, created with a top electrode resembling the shape of a diamond. In these experiments, indirect excitons were created in the quantum well, at the edge of the diamond trap, with a continuous wave laser. Excitons would then drift towards the region with the highest electric field along the growth axis. The shape of the top electrode creates a harmonic trapping potential, with two different trapping frequencies along the x and y di-

reaction, as shown in figure 2.4. High et. al. performed interference measurements and reported a critical temperature of 2 K below which the indirect excitons exhibit a coherence length of approximately $6\ \mu\text{m}$. This observation was interpreted as a direct signature of Bose-Einstein condensation of excitons. Furthermore, the authors reported a contraction of the exciton cloud in the trap, as they lower the temperature similar to atomic Bose-Einstein condensates. However it has to be mentioned that in the case for atoms, the atom cloud is released from the trap and the momentum distribution is imaged in a time-of-flight measurement. This is realized by taking absorption images of the atomic cloud after it had time to expand freely. The distribution of the absorption strength can then be used to deduce if one has observed a pure thermal gas or a Bose-Condensed gas which manifests itself through a bimodal distribution due to the non-condensed thermal part which is always present at finite temperatures. The analogy to an atomic BEC is therefore not correct. Moreover, Semkat and coworkers raised doubts concerning the measurements by suggesting that shift interferometry measurements can as well induce coherence patterns for incoherent sources [74]. In the same comment article the authors also raised doubts regarding the particle number in the trap. According to their calculations the critical number of particles necessary for condensation to occur in the experiments of High et. al. is only achieved at their lowest bath temperature of $50\ \text{mK}$.

Dark state condensation in a dipolar exciton fluid

The first report on dark state condensation was published by Shilo and coworkers in 2013 [75]. They used a $50\ \mu\text{m}$ wide circular electrode to create a box like trap for indirect excitons. The authors reported a temperature dependent decrease of the blueshift for a fixed density of indirect excitons which in their case, as they report, is a fluid. When lowering the temperature below a critical temperature T_C , however, they observe a sharp interaction increase while, according to their calculations, at the same time the population of bright states is remaining constant. They argued that the sharp temperature dependent increase of the interactions rules out the repopulation of the dark state, but rather indicates a macroscopical population of the dark state in a fashion reminiscent of the theoretical predictions of Combescot and coworkers.

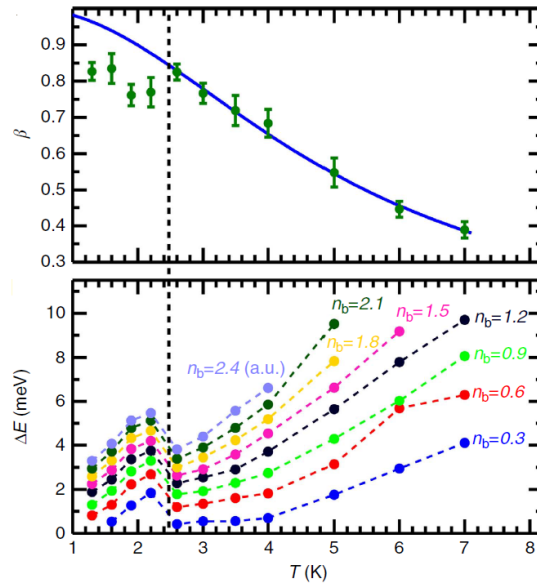


Figure 2.5: Top: Measurement of β the proportion of bright excitons within the light cone (green dots) together with the theoretical β (blue line) for an ideal 2D Bose Einstein distribution with a bright exciton density of $3.5 \cdot 10^{10} \text{cm}^{-2}$ [75].

Fragmented exciton ring

In 2014 Alloing and coworkers reported on evidence of a gray condensate of excitons, as predicted by Combescot and coworkers [2]. They obtained the evidence through interferometric measurements of the photoluminescence resembling a fragmented ring, below a critical temperature of approximately 2 K. This state is reminiscent of the macroscopically ordered state of excitons discovered by the group of Butov and coworkers. However, Alloing and coworkers provided further evidence for a gray condensate by showing extended coherence in regions next to the bright beads where the photoluminescence signal was 20 times smaller than in the bright beads. Furthermore they performed pump probe measurements which revealed a trapping potential for indirect excitons next to the bright beads. Additional spectroscopic measurements revealed a homogeneous density throughout the trap while the photoluminescence signal was inhomogeneous along the trap. Since the thermal activation energy was much higher than the energy splitting between the dark and bright states, they should be equally populated. However the density in the bright and dark regions do not reflect this situation. This contradiction led them to conclude this non-classical distribution between the population of bright and dark states was the manifestation of the gray condensate.

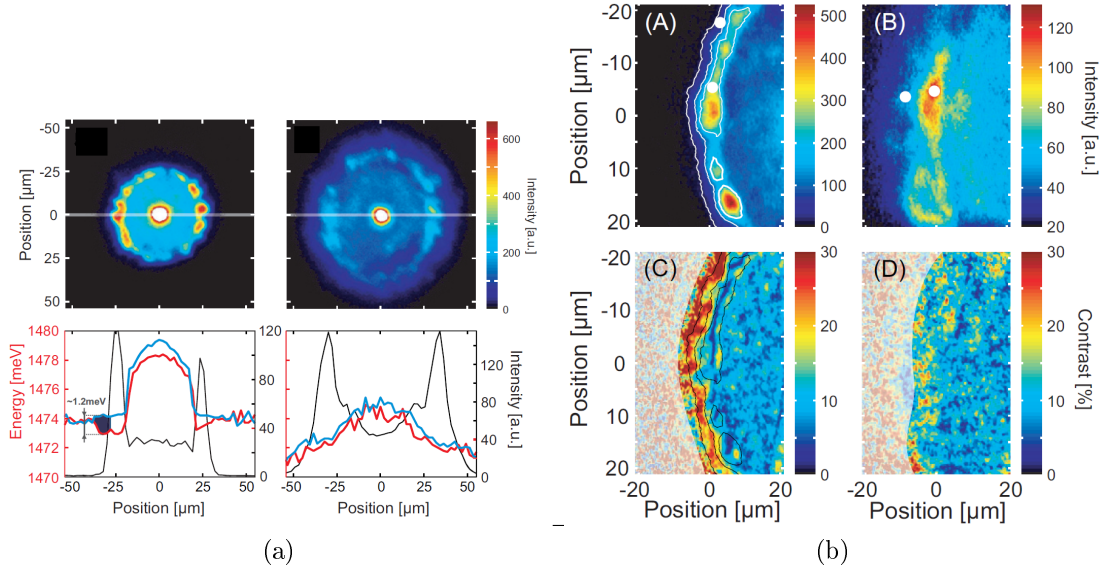


Figure 2.6: a) Top Row: Image of the fragmented ring at 330mK (left) and 3K (right) Bottom Row: Spatial variation of the density profile (blue), the trapping potential (red) and the photoluminescence signal for a horizontal cut as depicted in the images above for 330mK (left) and 3K (right). At 330mK a trap potential is revealed where the density of excitons is constant but the luminescence signal is varying drastically. b) Top Row: Intensity with isolines for 330mK and 3K. Bottom Row: Contrast of the coherence signal respectively. The white dots depict areas of high and low intensity.[2]

2.5 Expected signatures for dark state condensation

To finalize this chapter we would like to give an overview of experimental results that would unambiguously proof the dark state condensation of indirect excitons. This should manifest itself in a variety of ways which can all be quantified through photoluminescence experiments.

As pointed out in section (2.3), the dark states being energetically below the bright states, exciton condensation must predominantly take place in the dark state. As a result exciton condensation must be accompanied by a decrease of the integrated photoluminescence intensity when the bath temperature is lowered. A quantitative measurement would thus be to load a trap with a fixed density of excitons and map the evolution of the integrated photoluminescence intensity as the bath temperature is lowered. Lowering the temperature should also lead to a decrease of the spectral linewidth since exciton-phonon interaction is reduced.

2 Bose-Einstein-Condensation of excitons

Furthermore, for a dense enough exciton gas a bright part, which is coherently coupled to the dark exciton condensate, emerges. As the temperature of the exciton gas is lowered this photoluminescence signal from the bright part should show two characteristics. It should exhibit long-range spatial coherence due to the condensates extended wavefunction and an extremely narrow spectral linewidth. The magnitude at which this characteristics can be quantitatively measured is highly dependent on the ratio of condensed to non-condensed excitons in the trap. If the condensate fraction is too small, these quantum signatures will be blurred by the thermal part of the exciton cloud.

3 Sample and Experimental Setup

3.1 Experimental Setup

The experimental setup aims towards facilitating studies of the temporal and spatial dynamics of indirect excitons confined in a CQW heterostructure through photoluminescence experiments. Excitons are thus created through pulsed laser excitations and spatial as well as spectral information from the photoluminescence signal is extracted by optical means in a time resolved manner. To be able to obtain time resolved data, it is imperative that the laser excitations, as well as our detector, are well synchronized while at the same time allowing for great flexibility in terms of delay choices and pulse widths. In the first part of this section we introduce the three key components of our experimental setup. First, the cryostat used to cool our sample to sub-Kelvin temperatures while allowing for optical access and electrical connectivity to the sample.. Second, the laser system designed to provide the laser pulses, and at last the luminescence detection setup composed of an imaging spectrometer with a subsequent intensified CCD camera. We conclude this section by elaborating how the experimental control is implemented in terms of data acquisition and delay control to allow for time-resolved photoluminescence measurements.

3.1.1 The Cryostat

For the experimental work discussed in this thesis, the sample device is glued on a printed circuit board which is mounted on top of a cold finger of Helium 3 insert, cooled through thermal interaction with a closed cycle ^4He pulse tube (see figure 3.1a). The optical cryostat from Oxford Instruments (Model: Heliox-ACV) comes with optical access to the sample and extends a microscope objective with an effective focal length of 8.55mm from Edmund Optics. The objective is used

3 Sample and Experimental Setup

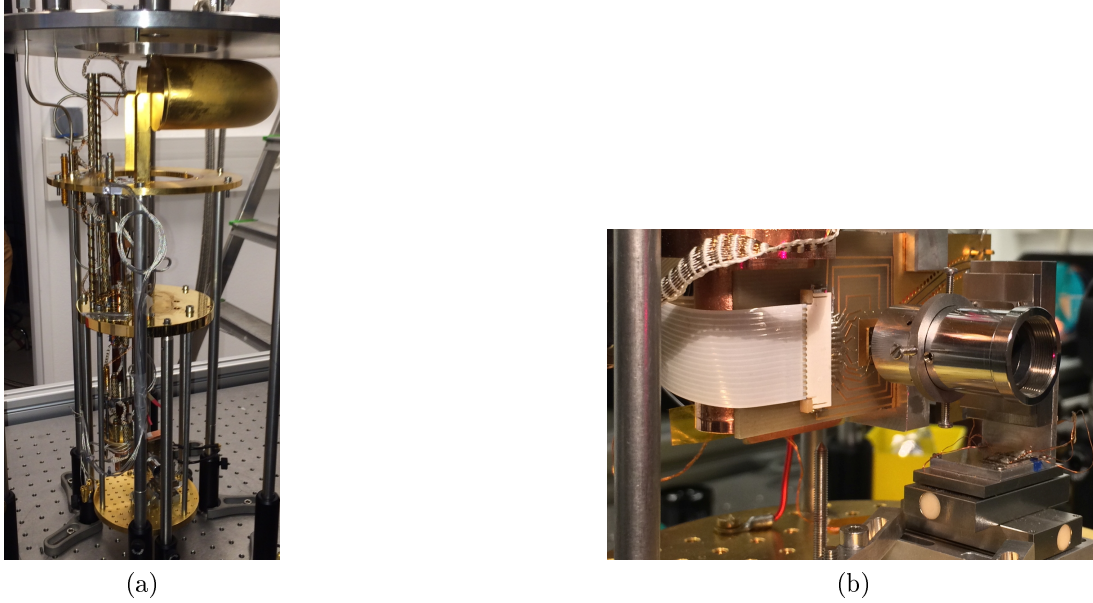


Figure 3.1: a) Image of the Heliox-ACV showing the pulse tube together with the ^3He inset. b) Close up image showing the microscope objective mounted on the piezo-stage, fixed on the PT2-plate. In front of the objective is the printed circuit board used to establish the electrical connection with the sample.

to excite the sample and collect the photoluminescence at the same time. The objective is mounted on a ML-17 piezo-based positioning stage from Mechanics AG. The positioning stage allows for linear translation over a range of 5mm in all three dimensions. It is mounted on top of the 2 K stage plate and placed in front of the sample holder(see figure 3.1b). A major drawback of our cryostat are the mechanical vibrations. They are mainly caused by the ^4He compressor that injects pulses of ^4He gas into the pulse tube which is used to cool the ^3He gas below 3K. In order to suppress these vibrations we have introduced a mechanical coupling between the 2 K stage plate and the sample mount. This coupling limits the displacement between the components to $2\ \mu\text{m}$ at frequencies up to 1 kHz. Let us note that the mechanical coupling also introduces a thermal coupling between the ^4He pot and the 2 K stage. However, the sample can still be cooled down to a temperature of $T_B \approx 330\text{mK}$ with a hold time of approximately 14 hours.

The DC voltage bias for our heterostructures is provided by source meter unit (SMU: Keithley Model 2614B) with a NI-Visa interface allowing the device to be completely computer controlled using standard test and instrumentation software (Matlab,Labview,...). The SMU has two independently controllable outputs. Beside providing a voltage bias, the SMU also measures the current down to $0.01\ \text{nA}$ sensitivity at each output port. The cryostat offers two possibilities to bias the sample via an external voltage source. The first option is to use one of 16 channels on a switch box connected to a loom of constantan cables ($R \approx 130\ \Omega$) in the

cryostat. This loom is mainly used to apply DC biases. Since the individual lines are not shielded, they are not suitable for AC operation due to crosstalk among the individual wires. The second possibility consists of 4 coaxial lines with a well defined electrical impedance of 40Ω . They allow for a simultaneous AC/DC operation through SMA connectors. All connections terminate at a printed circuit board that has been developed as part of this thesis. The board has been optimized to match the impedance of the four coaxial lines and allows for a rapid exchange of the sample (see chapter 6).

A major advantage of this cryogenic system is that it does not require a regular refill of Helium. Nevertheless, this independence comes at a price in terms of mechanical stability due to the mechanical vibrations created by the ^4He pulse tube. The modifications to suppress the vibrations limit the hold time at the base temperature of 330 mK . This last constraint restricts the type of experiments one can perform. In particular one has to carefully consider the trade off between a good signal to noise ratio, by selecting sufficiently long exposure times, and the hold time for temperatures below 2.5 K . Above this temperature the hold time does not act as a constraint for our experiments.

3.1.2 The Laser System

The laser system can be divided in three parts. Light generation, pulse generation and beam shaping. Our experiment has three Toptica DL-100 tuneable diode lasers with different excitation wavelengths.

- $\lambda_{exc} = 641.5 \text{ nm}$ to excite the AlGaAs barrier that separates the quantum well
- $\lambda_{exc} = 794.25 \text{ nm}$ to resonantly inject direct excitons in the GaAs quantum wells
- $\lambda_{exc} = 815.15 \text{ nm}$ matched to the photoluminescence wavelength of indirect excitons for optical alignment and homodyne detection

All lasers operate in continuous wave mode, whereas in studies of cold indirect excitons one wants to avoid a continuous laser induced heating, that would naturally prevent the exciton gas from thermalising to low enough temperatures. Hence, a temporal pulse shaping stage is necessary to create $50\text{-}150 \text{ ns}$ long laser pulses. This is realized by employing either integrated electro-optic modulators (EOM) provided by Jenoptik, or by using acousto-optic modulators (AOM) from

3 Sample and Experimental Setup

Crystal Technologies Inc. The EOM allows for the engineering of laser pulses with rise and fall times of 2ns while the acousto-optical modulators achieve rise and fall times of around 5ns. All three lasers can be pulsed independently through reception of a trigger pulse provided by a DG645 delay generator from Stanford Instruments.

After the pulse generation the beams are superposed and undergo a beam shaping stage to obtain the desired geometry on the surface of the sample, after being focused by the microscope objective embedded in the cryostat. In particular we made use of a small gaussian beam with a full width half maximum (FWHM) of approximately $5\mu\text{m}$, a wide gaussian beam with a FWHM of approximately $100\mu\text{m}$ and a line excitation. The 6 channels of the delay generators enable us to deploy 6 independently pulsed lasers along the same beam line. The mean excitation power is continuously monitored through a Thorlabs usb powermeter PMD100 and held constant by a motorized wave plate controlled through a customized software that has been developed as part of this thesis.

3.1.3 Photoluminescence Detection

The photoluminescence signal is collected by the microscope objective inside the cryostat and magnified in two stages by two different telescopes, mounted on the optical table. The first telescope yields a magnification of 20 while the second telescope yields a magnification of 2.3. The luminescence signal can be routed through a Mach-Zehnder, a Michelson-Interferometer or a polarization-analysis stage, by using magnetic mirror mounts. At last the photoluminescence is focused with a 200 mm lens on to the entrance of our imaging spectrometer, Acton SP2500 from Princeton Instruments. It is equipped with a mirror as well with a $600\frac{1}{\text{mm}}$ and a $1800\frac{1}{\text{mm}}$ grating, which can be selected by using the rotational motor on which they are mounted. The imaging spectrometer is mounted in front of an intensified CCD camera, Picostar-UF from LaVision, which has an effective pixel size of $13,9\mu\text{m}$. The intensified camera is triggered by the delay generator which also times the excitation pulses. Thus, we can either record real images with a spatial resolution of approximately $1.8\mu\text{m}$ by using the mirror[1], or spectra with a resolution of 0.25 meV or 0.5 meV using the $1800\frac{1}{\text{mm}}$ or $600\frac{1}{\text{mm}}$ grating respectively, with a temporal resolution down to 200 ps.

3.2 Experimental Control

The experiment is operated by two computers. The first computer controls the piezo stage inside the cryostat and also logs the sample temperature via the RS-232 interface of our temperature controller, the Oxford Instruments ITC-503. Furthermore, the computer hardware is used to control two monochrome Firewire800 CCD cameras, provided by "The Imaging Source", which allow us to quantify the optical axis of our experimental setup.

The second computer is our main experimental control computer. Its primary purpose is to operate the imaging spectrometer, the intensifier the integrated delay generator del350 and the Picostar CCD Camera. The image acquisition and storage is done with the Davis software provided by LaVision. A feature that is of great importance is the macro driven measurement capability. This functionality allows for automatized custom acquisition macros written in the DaVis Command Language. This command language also provides a NI-Visa interface and the capability to issue system commands, making it possible to control the state of our experiment and save it as metadata in the image file to facilitate later analysis. As part of this thesis we implemented the controls to read the status of the following devices of our experiment through DaVis:

- Stanford Instruments DG645 Digital Delay Generator
- Keithley 2614B source meter unit
- Thorlabs PM100USB power meter interface
- Thorlabs motorized DC rotation stage PRM1/MZ8E

This also means we can automatically log the current, the applied voltage and all delays, including their corresponding width. Of particular importance is the interplay between the motorized waveplate and the power meter interface which enables us to ensure that the excitation power stays constant at all times. The degree of control introduced by using custom measurement macros allows for extended measurement runs that are only limited by the hold time of the target temperature for measurements below 2.5 K. The automated measurement capability together with the log functionality of our experimental parameters allows for a much more efficient data acquisition since a majority of manual steps during the measurement are obsolete.

3 Sample and Experimental Setup

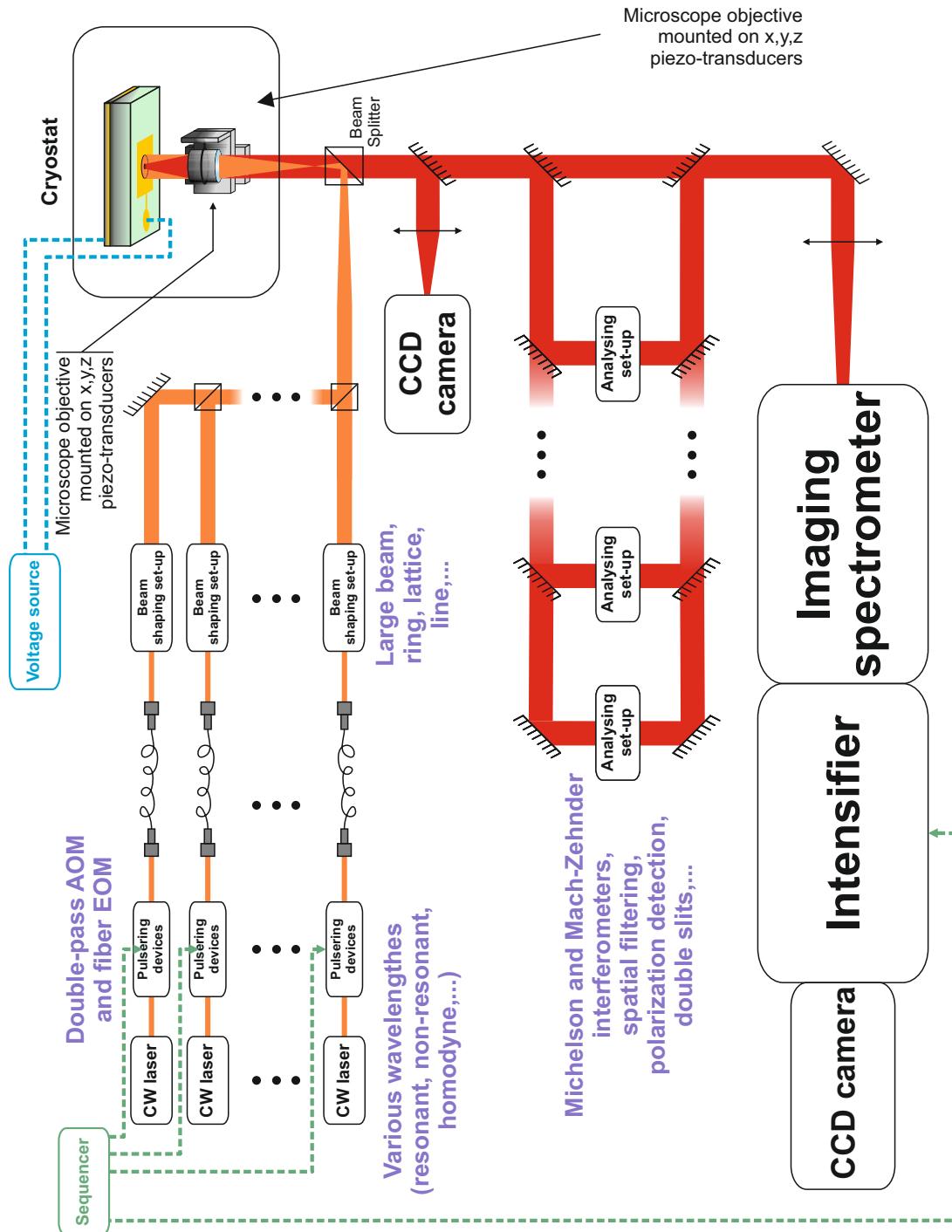


Figure 3.2: Overview of the experimental setup

3.3 Sample design and fabrication

The sample investigated throughout this thesis was grown by Aristide Lemaître and Carmen Gomez at the Laboratoire de Photonique et Nanostructures (CNRS/LPN) in Marcoussis, France, by molecular beam epitaxial growth. The growth of our sample is performed on a n-doped GaAs wafer which has been produced by standard crystal growth techniques by epitaxially depositing crystal layers with a

precision down to a single atom layer under ultra high vacuum conditions of approximately 10^{-11} mbar. In the case of $Al_xGa_{1-x}As$, with $0 < x < 1$, subsequent layers with different Aluminum alloy ratio allow for a high quality growth independent of their Aluminium content due to the small lattice mismatch. This allows for customized band-gap engineering of semiconductor heterostructures with low interlayer surface roughness [26, 27].

The top contacts of the sample were realized by means of electron beam lithography (EBL) and metal evaporation. This steps have been carried out by Edmond-Cambril (CNRS/LPN). The design of the top contacts was driven by the goal to ensure a control of the electrostatic environment to the fullest extent possible in terms of the trapping geometry and achievable trap depth. Thus, simulations of the electrostatic field distributions were performed prior to the actual realization of the field-effect device.

3.3.1 Heterostructure Layout

In this thesis we study an $Al_xGa_{1-x}As/GaAs$ coupled quantum well with $x \approx 0.3$. It consists of two 8 nm wide GaAs quantum wells, separated by a 4 nm wide $Al_xGa_{1-x}As$ barrier, in a wide layer of $Al_xGa_{1-x}As$. The structure is grown on a $n^+ - GaAs$ layer which is followed by a 800 nm wide undoped GaAs layer. Due to the undoped GaAs Layer, the CQW is a priori electrically isolated from

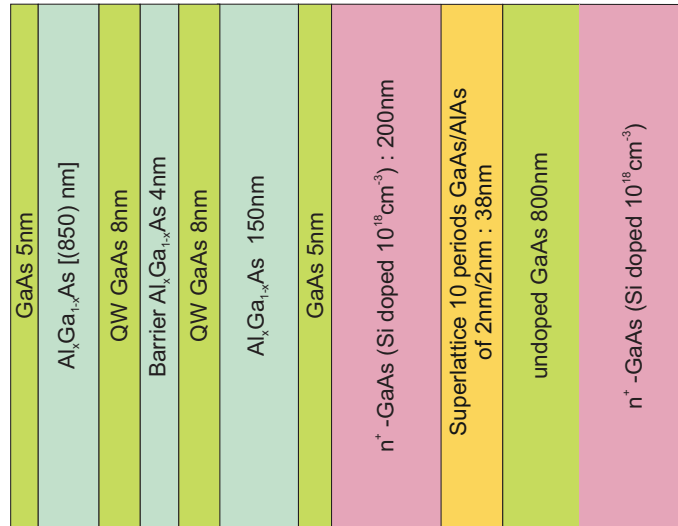


Figure 3.3: Scheme of our sample structure

the sample holder. On top of this layer, a 10 period superlattice was grown, consisting of 2 nm wide alternating GaAs/AlAs layers. It serves as a barrier for leakage currents. The superlattice is followed by a 200 nm wide $n^+ - GaAs$ layer.

3 Sample and Experimental Setup

This layer serves as the bottom electrode of our device. An ohmic contact is engineered by means of a diffusive bonding contact. Our coupled quantum well structure is then embedded within two 5 nm wide GaAs layers 150 nm above the bottom electrode and 850 nm below the top electrode. The top GaAs layer serves as protective layer against oxidation. When storing the device it is recommended to protect the top GaAs layer from scratches by depositing a protective PMMA layer on top.

3.3.2 Trap design

The main purpose of our electrostatic trap, besides the creation of long lived indirect excitons, is to control their confinement in the CQW plane. The trap studied throughout this thesis consists of two electrodes. A circular trap electrode with 10 μm diameter surrounded by a large guard electrode as depicted in figure 3.4a. The spacing between the trap and the guard electrode was set to 400 nm. A lead electrode within the guard gate is needed to bias the trap gate. It is 0.5 μm wide and has a distance of 0.25 μm to the guard gate. Ideally we would like to control

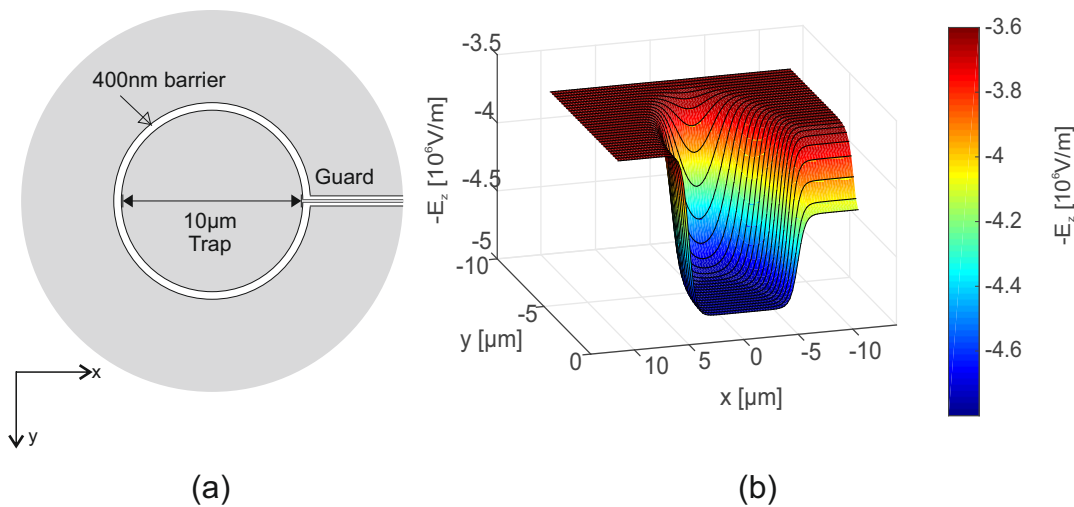


Figure 3.4: a)Schematic drawing of our top gates. A circular gate of 10 nm diameter gate is surrounded by a guard gate of 50 nm diameter. b)Simulated electrostatic trapping potential for our indirect excitons for $V_{trap} = -4.8V$ and $V_{Guard} = -3.6V$.

the trap depth over an arbitrary range of values., However, it is also important to keep electric fields perpendicular to the growth axis as small as possible. Due to the excitons finite binding energy, too large in-plane electric fields will lead to exciton dissociation through ionization, especially at the trap boundaries as seen in subsection 1.3.3. In the case of our sample the binding energy of our

indirect excitons is $E_B \approx 4meV$ [77]. According to equation 1.9 this imposes an upper limit for the critical in-plane electric field of $|\vec{E}_{r,critical}| \approx 4 \cdot 10^5 \frac{V}{m}$. We simulated the field distribution in our device using the COMSOL Multiphysics[©] software with $V_{trap} = -4.8V$ and $V_{Guard} = -3.6V$. This allows us to get an estimate of the electric field distribution inside the trap. In figure 3.4b we plot the z-component of the electric field. The simulation reveals a trapping potential with a flat bottom and steep flanks at the boundaries of the central gate, resembling a box trap with radial symmetry. The radial symmetry of the electrostatic potential is actually broken by the lead electrode necessary to establish a connection between the voltage source and the central disc. The electric flux originating from the potential difference between trap electrode and the ground is reduced in the z-direction along the strip resulting in a potential trench along the electrode with reduced trap depth. This is a fringe effect at the edge of the electrodes, it is common for all finite size gate electrodes. Since the electric flux through a closed surface is conserved according to Maxwell's equations, the radial component grows as the surface of the electrode is reduced [39]. By plotting the radial component, we can directly identify the regions where in-plane fields are strong enough to ionize the excitons. The results are plotted in 3.5. First let us examine the dependence of the in-plane electric field along the x-axis depicted in figure 3.5a. As one would expect the in-plane field reaches its maximum at the edges of the trap gate. Along the boundary of the trap the in-plane field is constant except at the joint between lead electrode and trap gate where the discontinuity is less pronounced due to the physical connection of the trap to the lead electrode. The in-plane electric field is furthermore strongly dependent on the z-coordinate as depicted in figure 3.5b. Thus, the quantum well should be placed as close as possible to the ground electrode in order to keep the in-plane field as small as possible over a wide range of values for the trap and guard voltages. In order to get a comprehensive overview for a wide range of trap configurations we simulated the electric field for all pairs $\{V_{trap}, V_{guard}\} \in [-4.8V, -2.2V]$ with a step size of 0.2 V. The result of the maximum in plane field is shown in figure 3.6. As one would expect, the in-plane field grows with the difference between the potential of the trap and guard gate. Nevertheless, the simulation indicates that the maximum in-plane field with $|\tilde{E}_r| \approx 2 \cdot 10^5 \frac{V}{m}$ is a factor two smaller than our critical field $|\tilde{E}_{r,critical}| \approx 4 \cdot 10^5 \frac{V}{m}$. The simulation shows that the trap allows for a broad parameter space $\{V_{trap}, V_{guard}\}$ where in-plane fields remain still well below the critical in-plane critical field.

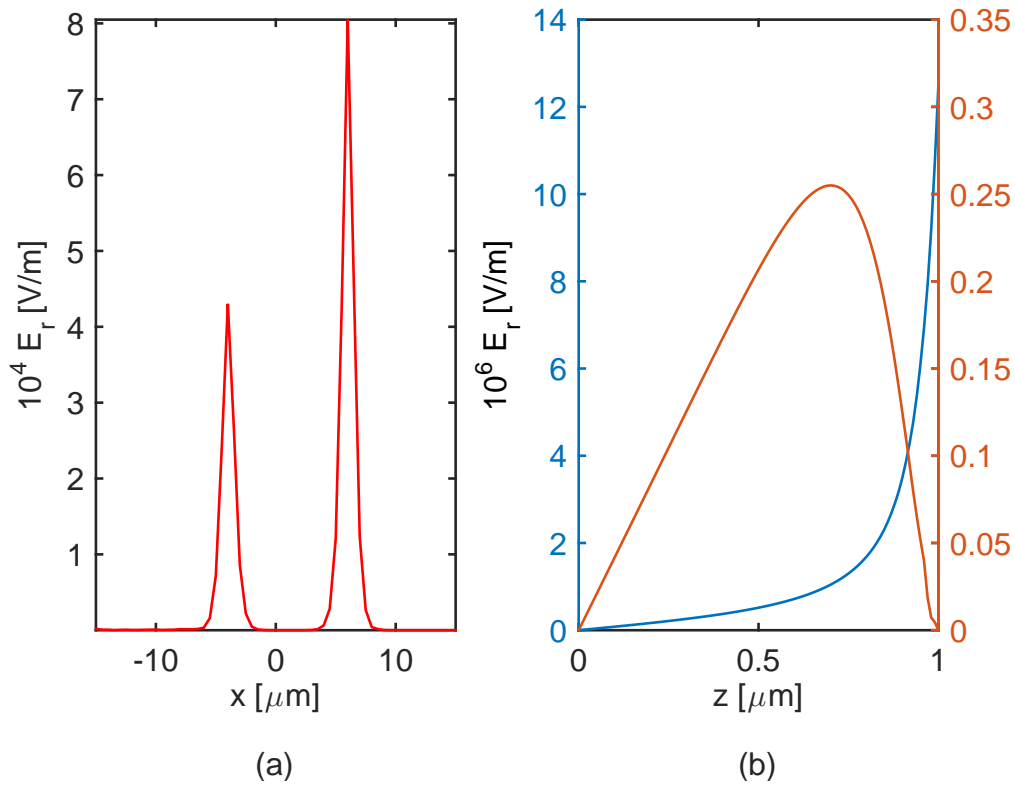


Figure 3.5: Simulation results of the in-plane electric field E_r : a) Plot showing the in-plane electric field along the x-axis 100 nm above the electric ground. The simulation shows two maxima at the edges of the center electrode. The peak at $x = -5 \mu\text{m}$ is reduced since center gate and electrode provide intersect at this point. b) Plot showing the radial electric field component along the growth axis (z-axis) at the intersection between lead electrode and center gate (red), and at the discontinuity at $x = -5 \mu\text{m}$ (blue).

3.3.3 Contact fabrication

Top electrode fabrication

Our top contacts consist of two layers. The first layer is a thin semi-transparent metal surface. It provides us with optical access to the excitons in the CQW below the trap electrode. The second layer is a thick metal layer used to contact our sample by means of wire bonding. The fabrication process is shown in figure 3.7. Prior to the fabrication, the sample is cleaned in a bath of acetone to remove any unwanted residuals from the top GaAs layer, and thus avoid any impurities in the metal layers. The sample is then spin coated with a polymethyl methacrylate (PMMA) solution and placed in a hot oven to solidify the PMMA layer. After this step the sample is ready for electron beam lithography (EBL). The PMMA in the exposed areas, which will later be metal coated, is fractured by the electron beam. After the lithography we put the sample into a developer bath which removes the

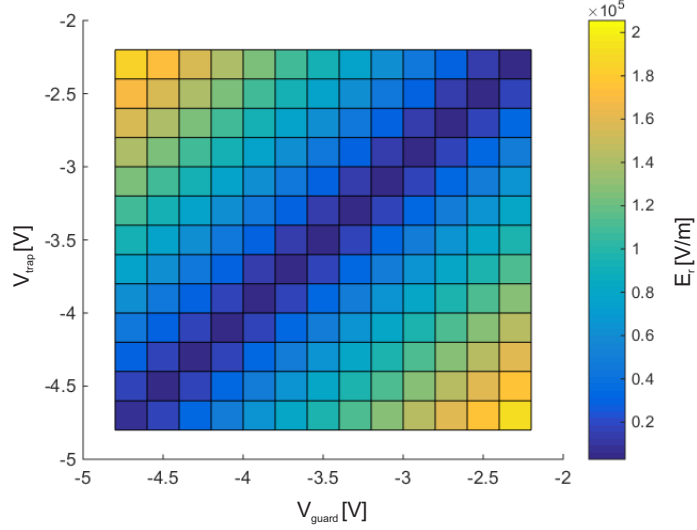


Figure 3.6: Result of the in plane electric field simulation for all $\{V_{\text{trap}}, V_{\text{guard}}\} \in [-4.8 \text{ V}, -2.2 \text{ V}]$ showing that in-plane field grows with increasing difference between the gate voltage.

exposed PMMA layers. The sample is then ready for metal evaporation where, first, we deposit a 4 nm layer of Titanium followed by 6 nm of Gold. The remaining PMMA will be removed with Aceton. To ensure a good electrical contact and to be able to attach wire bonds to our electrodes we repeat the process but this time we deposit a 200 μm thick gold layer in the areas where wire bonding will be performed. In contrast to the first layer we didn't expose the same areas, to be precise we do not expose the areas where we want to inject excitons or where we later want to retrieve their photoluminescence signal.

Bottom electrode fabrication

The bottom electrode is used as an electrical ground. This back contact is realized by etching down two separate 1 mm wide strips at the outer edges on the top of our sample, as depicted in figure 3.8, down to the 200 nm wide n^+ – GaAs layer. The ohmic back contact is realized by first evaporating a mixture of Germanium and Indium particles on to the etched strip. Then, in order to create the ohmic back contact, is necessary that the Germanium and Indium particles diffuse in the n^+ – GaAs layer. This is achieved by processing the sample in a diffusion oven. In order to remove any water residuals from the sample, it is first heated to 150^o C in an inert Argon atmosphere. Afterwards the sample is heated to a temperature of 420^o C which will cause the evaporated particles to diffuse into the n^+ – GaAs layer, transforming it into an ohmic contact. The ohmic character of the contact is tested by recording the current-voltage curve and confirming a

3 Sample and Experimental Setup

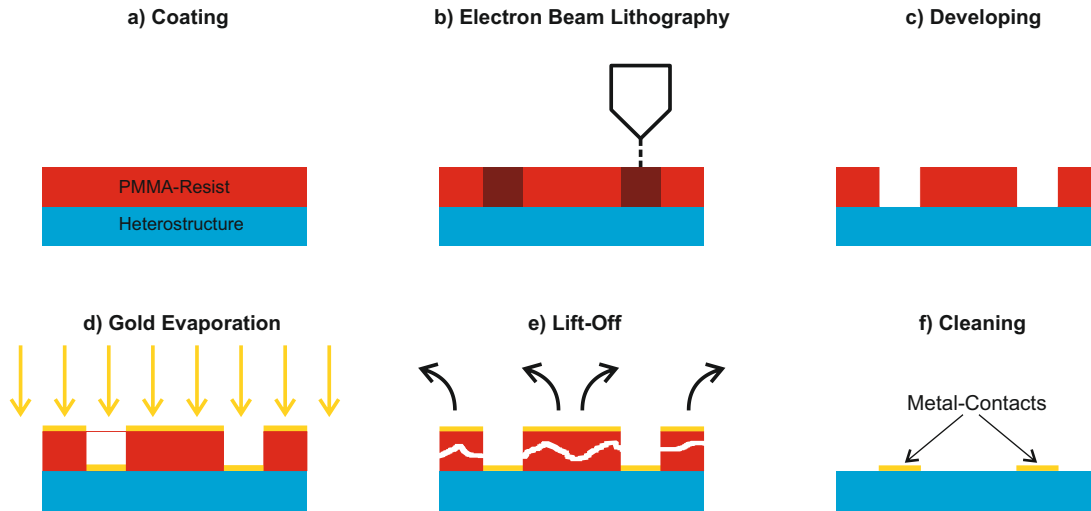


Figure 3.7: a) The sample is coated with a PMMA photoresist. b) The desired trap gate is fabricated by removing the photoresist where the electron beam has fractured the PMMA resist which c) is removed by the developer. d) The gates are fabricated by evaporating a thin metal layer to the open GaAs surface. e) The remaining PMMA is removed in a lift-off stage that only leaves the metal gates on the GaAs surface. f) The sample is put in a beaker with Aceton and put in an ultrasonic bath to remove remaining residues. The fabrication is repeated to obtain a thick gold layer for the bonding contacts.

linear dependence. In a last step a layer of gold is evaporated onto the two strips in order to be able to contact them by means of wire bonding.

Wire bond process

We use conductive silver paste to glue our sample on the PCB. The bottom and top electrodes are then contacted to their corresponding pads on the PCB by means of thermosonic wire bonding. The bonding wires are made of gold and have a diameter of $25\mu\text{m}$. The connection is made by feeding the gold wire through a thin ceramic capillary. A high-voltage discharge is used to melt the end of the wire causing it to form a ball. The ball will rapidly solidify and is then pushed onto a contact pad on the sample where a short ultrasonic pulse will weld the bonding wire on to the thick gold layer. The tip is then directed to a the PCB where it is welded on to a designated connection pad. Figure 3.8 shows the complete assembly on the PCB.

3.3.4 Electrical properties of the heterostructure

At the interface between metal contact and top GaAs layer a schottky barrier is formed leading to a built-in voltage $V_{Schottky}$. The field in the heterostructure is

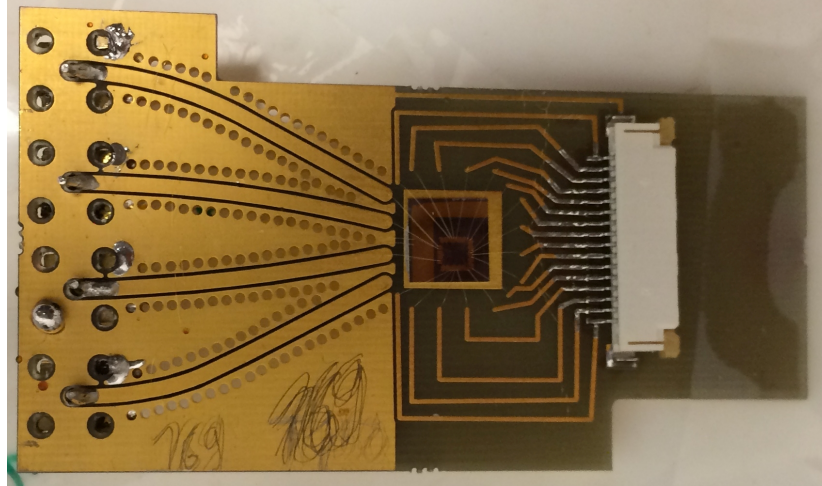


Figure 3.8: Photo of the complete assembly. The sample is glued on top of the PCB. The electrical connections are established through wire bonds between the signal lines of the PCB with the thick gold contacts on the sample. The two gold strips at the edge of the sample are diffusive bond contacts which serve as electrical back contact.

therefore the sum of the field created by the applied bias voltage and the built in potential. When the device is reverse biased electron flow is prohibited unless we exceed the breakdown voltage which would lead to permanent damage of our device.

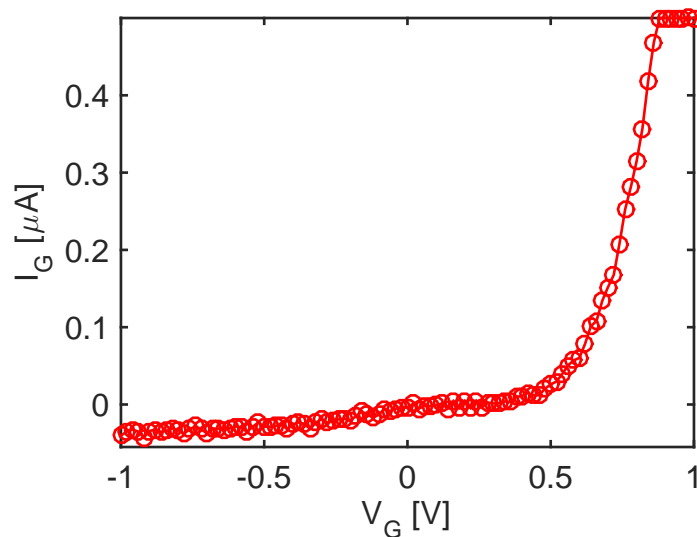


Figure 3.9: Current-Voltage characteristics of our field-effect device taken at room temperature showing that for safety reasons the applied voltage should not exceed $V_G < -0.8$ V. Exceeding this voltage could lead to severe damage of our field-effect device when the breakdown voltage is reached. For voltages $V_G > 0.5$ quantum wells become populated with electrons, thus leading to a screening of the external field and leading to an exponential increase of I_G . Exceeding this limits must be avoided under all circumstances to prevent permanent damaging of the field-effect device.

3 Sample and Experimental Setup

Forward biasing the device yields no significant increase of the measured current up to the point where the energy of the conduction band electrons in the quantum wells is lowered below the Fermi energy. This leads to a flow of electrons from the back contact into the quantum wells until they are filled up to the Fermi energy again. A further increase of the voltage leads to an exponential rise of current through the device that could damage the heterostructure as well. Exceeding this limiting voltages must therefore be avoided at all cost.

Figure 3.9 shows the room temperature I-V characteristics of our heterostructure measured by a semiconductor device analyzer. The analyzer was set to record the current while sweeping V_G from -1 V to 1 V. In order to protect the sample the current limit was set to $0.5 \mu\text{A}$ to avoid exceeding the breakdown voltage as well as an exponential increase of the tunneling current when increasing the forward bias. The measurements were performed at room temperature. There are in principal three distinct areas

- $V_G < -0.8\text{ V}$: Current of up to 10 nA measurable, voltages much lower than -0.8V should be avoided to avoid exceeding the breakdown voltage which will permanently damage the field-effect device.
- $-0.8\text{ V} < V_G < 0.5\text{ V}$: The current is negligible allowing for the safe operation of the field effect device in this area.
- $V_G > 0.5\text{ V}$: Quantum wells get populated with electrons leading to a screening of the internal electric field. Study of indirect excitons are not possible in this area.

The described behavior is strongly temperature dependent. At temperatures below 3 K for instance, we do not detect any significant dark current. For instance, given the sample is not illuminated, for gate voltages down to $V_G \approx -5\text{ V}$ the leakage current is less than 10 pA.

4 Electrostatic trapping of spatially indirect excitons

Motivated by the works of Keldysh and Kozlov, which predicted the possibility of an exciton BEC, the realization of a cold gas of excitons became a very active area of research in the field of semiconductor physics starting from the 1980's [45].

Ideally, one confines long lived excitons at a low bath temperature where microscopic properties can be quantitatively studied in a regime where the gas is free from sources of inhomogeneous broadening. In this chapter, we demonstrate that we are able to reach this degree of control with spatially indirect excitons confined in an electrostatic trap. This is achieved by exploiting the interaction between the electric dipole of indirect excitons and the field applied perpendicular to the growth axis of the CQW. Electrostatic traps provide a very flexible platform to manipulate the excitons spatial confinement. Indeed, they are simply realized by depositing gate electrodes on the surface of the field effect device. We will show that an elementary geometry consisting of two electrodes is already sufficient to produce a trapping potential with a spatial extension of approximately $7\text{-}8\ \mu\text{m}$.

An ideal trap should give a temporally and spatially stable trapping potential together with in-situ control of the potential landscape. This is ideally achieved by exploiting the high-field seeking nature of indirect excitons. The attempts to realize such a trap include strain induced traps [61], magnetic traps [16], laser induced traps [34, 3] and electrostatic traps. Electrostatic traps have lately become very popular among experimentalists in the field. They are a very favorable candidate according to our criteria for an ideal trap in terms of the wide variety of realizable potential shapes and in-situ control. Although this method of exploiting the dipolar nature of indirect excitons in order to spatially confine them is relatively new, it has already led to quite remarkable advances [91, 92, 68, 33, 15, 35, 73, 51].

In this chapter we report on photoluminescence experiments with indirect excitons in our GaAs/AlGaAs coupled quantum wells confined in an electrostatic

trapping potential generated by semitransparent metal gates. We will show the versatility of such a trap in terms of the range of trapping configurations accessible. Furthermore we will assess the stability of our potential over time by means of a dedicated pump-probe experiment.

4.1 Exploring the potential landscape

The potential landscape explored by the excitons is created by a disk trap. The disc trap consists of two semi-transparent metal gates. A circular shaped $10\ \mu\text{m}$ wide gate, the trap gate, is enclosed by a much larger gate (figure 4.1a), the guard gate

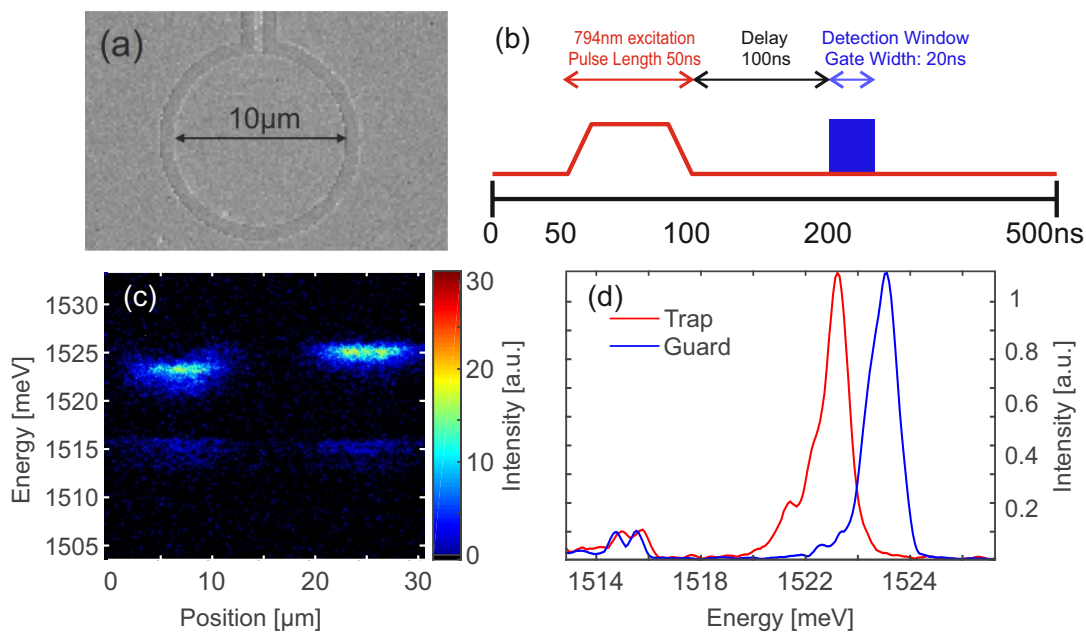


Figure 4.1: Probing the potential landscape with two laser beams focused on guard and trap gate respectively with excitation power set to $P_{ex} = 500\ \text{nW}$. The voltages for the trap (V_T) and guard gate (V_G) were set to $V_T = -4.4\ \text{V}$ and $V_G = -3.4\ \text{V}$. a) SEM-Image of the investigated trap with a $10\ \mu\text{m}$ diameter trapping gate separated by a $400\ \text{nm}$ guard gate. b) Sequence of the laser excitation and recording window. c) Spatially resolved spectrum of the photoluminescence signal emitted from the trap gate(left) and the guard gate(right). The image is an average of 10 single images, each with an exposure time of 15 s. d) Normalized spectral profiles emitted from the trap gate (solid red line) and guard gate (solid blue line) taken along the center of the trap along the line depicted in a).

The two electrodes are separated from each other by $400\ \text{nm}$. They are independently connected to the two outputs of the source meter unit. The experimental sequence is depicted in 4.1b: The wavelength of the laser is set to resonantly

excite the direct exciton absorption. This minimizes the generation of excess carriers as elaborated in section 1.4. Thus, direct excitons are photo-generated in the coupled quantum wells with a 50 ns long laser pulse at a repetition rate of 2 MHz.

The direct excitons formed in the two quantum wells become indirect excitons once electronic carriers have tunneled through the 4 nm AlGaAs barrier. The photoluminescence, emitted by the indirect excitons is then collected with our imaging spectrometer, after the extinction of the laser pulse. To suppress the laser leakage we use a longpass filter with a cutoff wavelength at 805 nm . A representative spectrum is shown in figure 4.1d. The photoluminescence is recorded 100 ns after the extinction of the laser pulse with a 20 ns gate width, also at 2 MHz repetition rate. The final image is an average of 10 single images, each acquired with an exposure time of 15 s in total. This experimental sequence is kept the same for the rest of this section.

4.1.1 Trap Depth - Recording a Potential Map

In the following we quantify the performance of the trap for a wide combination of voltage pairs. Therefore we inject indirect excitons at two separate positions by splitting the excitation pulse (figure 4.1c). The first beam is focused onto the trap gate to assess the behavior for the indirect excitons below this electrode. A second laser beam is focused onto the guard gate, $20\text{ }\mu\text{m}$ outside of the trap. The two beam waists are set to a width of $5\text{ }\mu\text{m}$, while their mean optical power is set to $P_{ex} = 500\text{ nW}$. We study the spectrum 100 ns after the end of the laser excitation to minimize any perturbative effects due to the photocurrent generated by our laser excitation. The recording settings are thus the same as depicted in 4.1b giving an average of 10 single images each with an exposure time of 15 s.

We reconstruct potential maps by studying the photoluminescence energy with respect to the applied gate voltages. The difference in energy between the photoluminescence peaks emitted from the guard and trap gate directly gives the depth of the potential trap between the two electrodes. By sweeping the trap and guard voltages we obtain a potential map displaying the trap depth for the various settings of V_G and V_T . As a first result figure 4.2 shows that we can create up to 9 meV deep trapping potentials for $V_T < V_G$. For values $V_T > V_G$ on the other hand, the excitonic potential below the trap gate is energetically higher than the one below the guard gate. We refer to this configuration as antitrap. As can be seen from figure 4.2 the highest potential step realized in the anti-trap regime is 9 meV high.

4 Electrostatic trapping of spatially indirect excitons

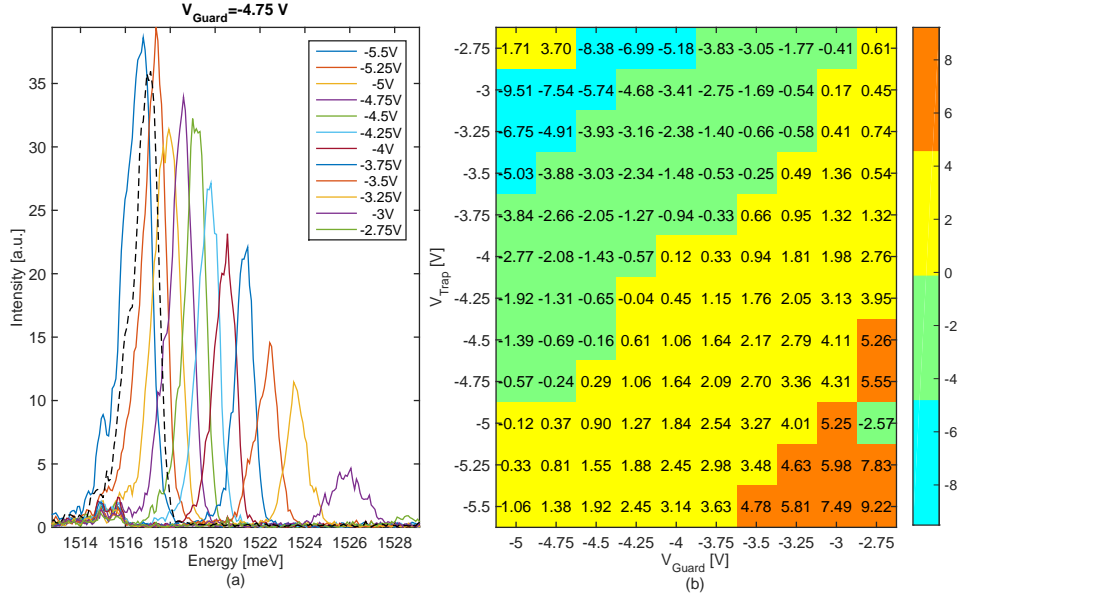


Figure 4.2: a) Spectra obtained from the trap keeping the guard constant at -4.75 V, while ramping the trap voltage from -5.5 V to -2.75 V in 0.25 V increments. The dashed black spectral profile was obtained from the guard gate. b) Map showing the potential depth depending on the applied bias at the trap and guard gates.

4.1.2 Electric Charges in the field effect device

To quantify our experimental findings, it is necessary to understand how much the photocurrent in the field effect device has an effect on our experiments. Our source meter measures the photocurrent at every applied voltage which enables us to examine dependencies between the applied bias voltages and the observed photocurrent. At this moment it has to be mentioned that any current present in our sample was solely due to the laser excitation induced photocurrent. This means that all charges contributing to the measurable current are created by the laser excitation, the highest dark current of 10 pA only being detected for gate voltages lower than -5 V. However, this does not exclude that the CQW suffers from a significant level of natural doping.

Figures 4.3a and b show the dependency between the applied voltage biases and the recorded photocurrent for the trap and guard gate respectively. At first it is noteworthy that the photocurrent through our device is remarkably low with a maximum of around 300 pA for the trap gate and 80 pA for the guard gate. Furthermore, the plot shows that the photocurrent in one electrode is mainly dependent on the applied bias voltage at that electrode. At the same time for a fixed bias of the trap (guard) voltage the current shows only a slight variation when changing the guard (trap) bias. Figure 4.3c shows the current in the trap

and guard gate for $V_{Trap} = V_{Guard}$. The two curves are essentially identical with the difference in magnitude being the only difference. This is expected since the trap gate is much smaller than the surrounding guard gate.

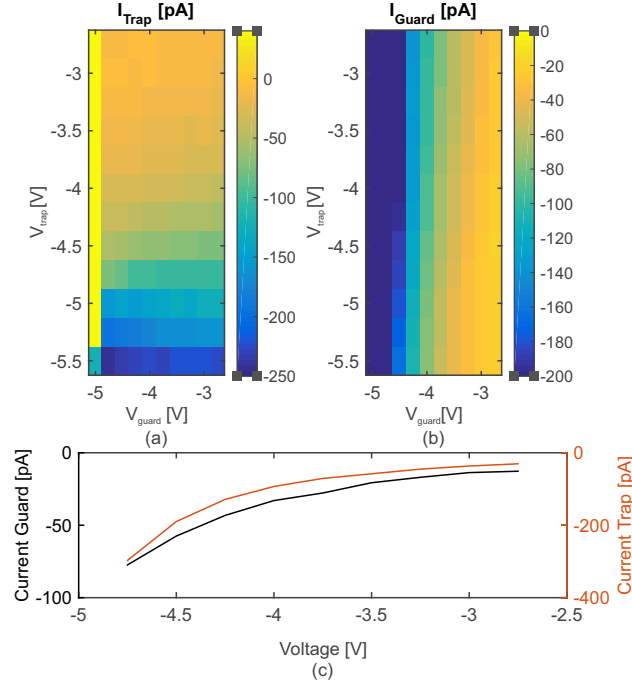


Figure 4.3: a-b) Variation of the current for all voltage settings flowing through the trap and guard gate respectively. c) Variation of the current versus the voltage for $V_{Trap} = V_{Guard}$ flowing through the guard gate (black) and trap gate (red).

4.1.3 Measurement of the dipole moment

To ensure that we work in a regime where the exciton interaction with the externally applied electric field is of dipolar nature, we extract the dipole moment from the potential map. Thus, we extract the position of the energy peak from the photoluminescence spectra recorded at the guard as well as the trap and plot them as a function of the applied gate voltage (figures 4.4a,b). A linear fit reveals a slope of $5.3 \frac{\text{meV}}{\text{V}}$ indicating an effective electron hole distance of 5.3 nm. This is about half of the theoretically expected distance of 12 nm between the quantum well centers for our field effect device. The deviation from the theoretical value can have several reasons. We believe that photo-induced excess charges is the most important one. A fraction of these excess charges can become trapped at the heterointerfaces. As outlined in section 1.4 figure 1.7, this can lead to a modification of the internal electric field. This effect can also occur at the surface gate electrodes where, due to the metal-semiconductor interface, a Schottky barrier is present. The combined effect of these captured charges can explain the deviation from the theoretically expected value.

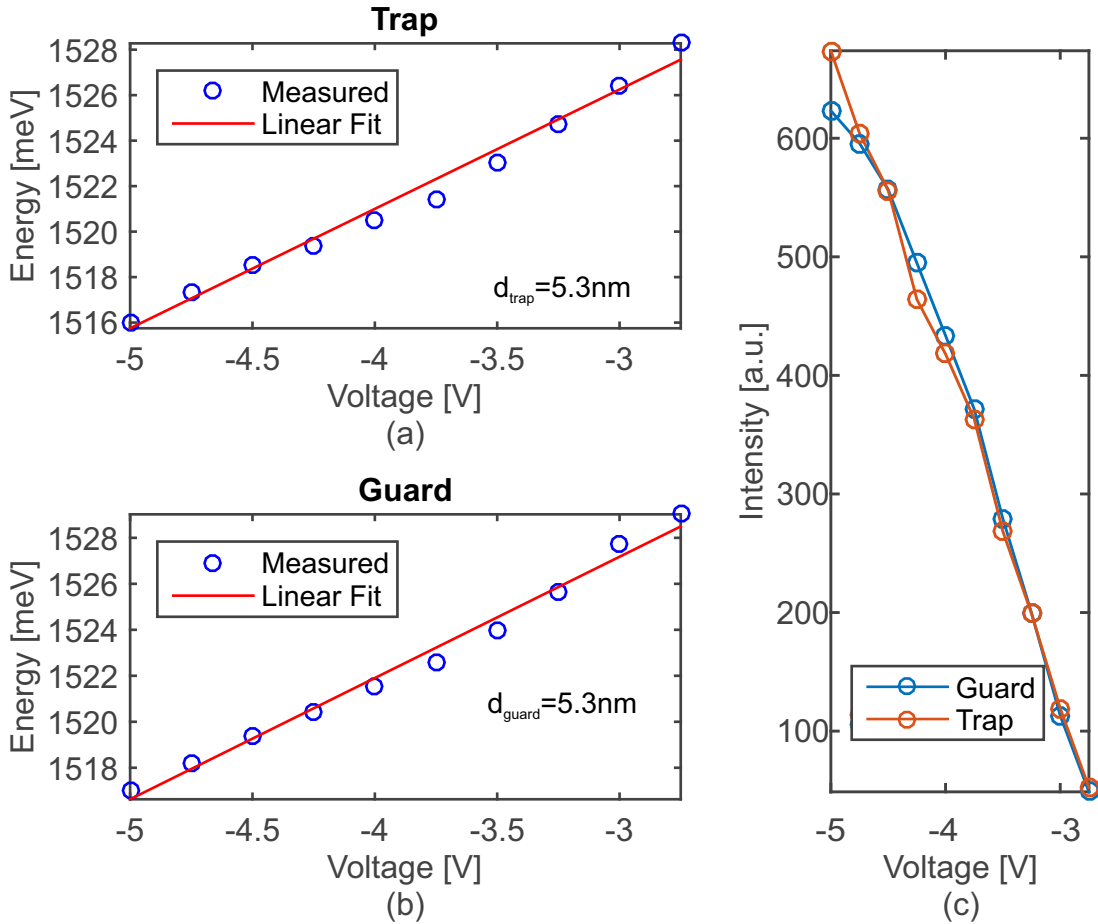


Figure 4.4: a)-b) Plots showing the variation of the photoluminescence energy peak versus the gate voltage (blue dots), together with a linear fit. The linear fit reveals an effective distance of 5.3nm between the electron and the hole of the exciton. c) Plot showing the linear dependence between the intensity and the gate voltage.

4.1.4 Linewidth

The profile of the spectrally resolved photoluminescence provides quantitative information about the interaction between the excitons themselves and the interactions between the excitons and their environment. The spectral linewidth, defined as the full width at half maximum, reveals the coherence time of bright indirect excitons, i.e. the time excitons spend on average in the light cone. If indirect excitons were only subject to homogeneous broadening the line shape would be a lorentzian, while inhomogeneous broadening leads to a wider gaussian line shape.

For indirect excitons homogeneous broadening can be caused by the dipolar exciton-exciton interactions, scattering between excitons and acoustic and optical phonons, as well as the finite radiative lifetime of the excitons. At temperatures below 1 K, the exciton-phonon interaction can be neglected since the thermal

activation energy for 0.33 K corresponds to 0.03 meV. The long lifetime of spatially indirect excitons of, between $10^2 - 10^3$ ns, also allows to discard broadening due to the radiative recombination since the maximum contribution is on the order of neV. Inhomogeneous broadening on the other hand is understood as an effect caused by the average of the disordered electrostatic potential. The disorder potential has several origins: Impurities, photo-induced excess charges, alloy fluctuations and crystal defects modify the band structure leading to band gap fluctuations [35]. Another contribution to disorder is the quantum well thickness that can fluctuate due to the interface roughness. However, this source of inhomogeneous broadening is minimized by using state of the art epitaxial growing techniques and is only relevant for low exciton densities. For higher exciton densities, the repulsive dipolar interaction between indirect excitons leads to the screening of the underlying disorder potential. The disorder potential can be characterized by the correlation length and the amplitude of its fluctuations. For a small correlation length compared to the exciton Bohr radius, the exciton wave function is subject to all fluctuations leading to a spectral line shape with no distinct features. On the other hand, when the correlation length is larger than the exciton Bohr radius, the excitons experience the disorder potential and rest in the local minima of the disorder potential, which can lead to peaks in the photoluminescence spectrum.

By examining the linewidth we can therefore obtain two different informations. The homogeneous broadening is an indicator for the interaction effects between the excitons while the inhomogeneous broadening is an indicator for the sample quality. We have extracted the spectral linewidth from all spectra recorded to obtain the potential map in the section before. The results are plotted in figure 4.5 for the trap and guard gate. For the trap gate we can identify two distinct regions. The first region is characterized by narrow linewidths around 1.1 meV and voltage settings for an anti-trap configuration. The second region shows larger linewidths of around 1.5 meV and coincides with voltage settings for the trap configuration. This behavior can be understood by looking at the charges in the quantum well. In the trap configuration ($V_T < V_G$), the photogenerated holes below the trap gate remain predominantly confined below the trap gate, while the electrons tend to leave the trap gate towards the energetically more favorable guard gate. For the anti-trap configuration ($V_T > V_G$) the situation is reversed. Electrons accumulate below the trap gate whereas holes accumulate below the energetically more favorable guard gate. We can see from figure 4.5 that the excitons created far away from the trap show an average linewidth of 1.2 meV that does not vary much when the voltage bias is changed. We therefore conclude that the

4 Electrostatic trapping of spatially indirect excitons

photogenerated holes, which possess a lower mobility than electrons, accumulate below the center electrode in the trap configuration and are responsible for the inhomogeneous broadening of the linewidth. This interpretation is in agreement with previous observations by Kowalik-Seidl et al. where the variation of the photoemission from a trap gate surrounded by a guard gate was enhanced when they went from a trap to an anti-trap setting, thus leading the authors to the same interpretation [51].

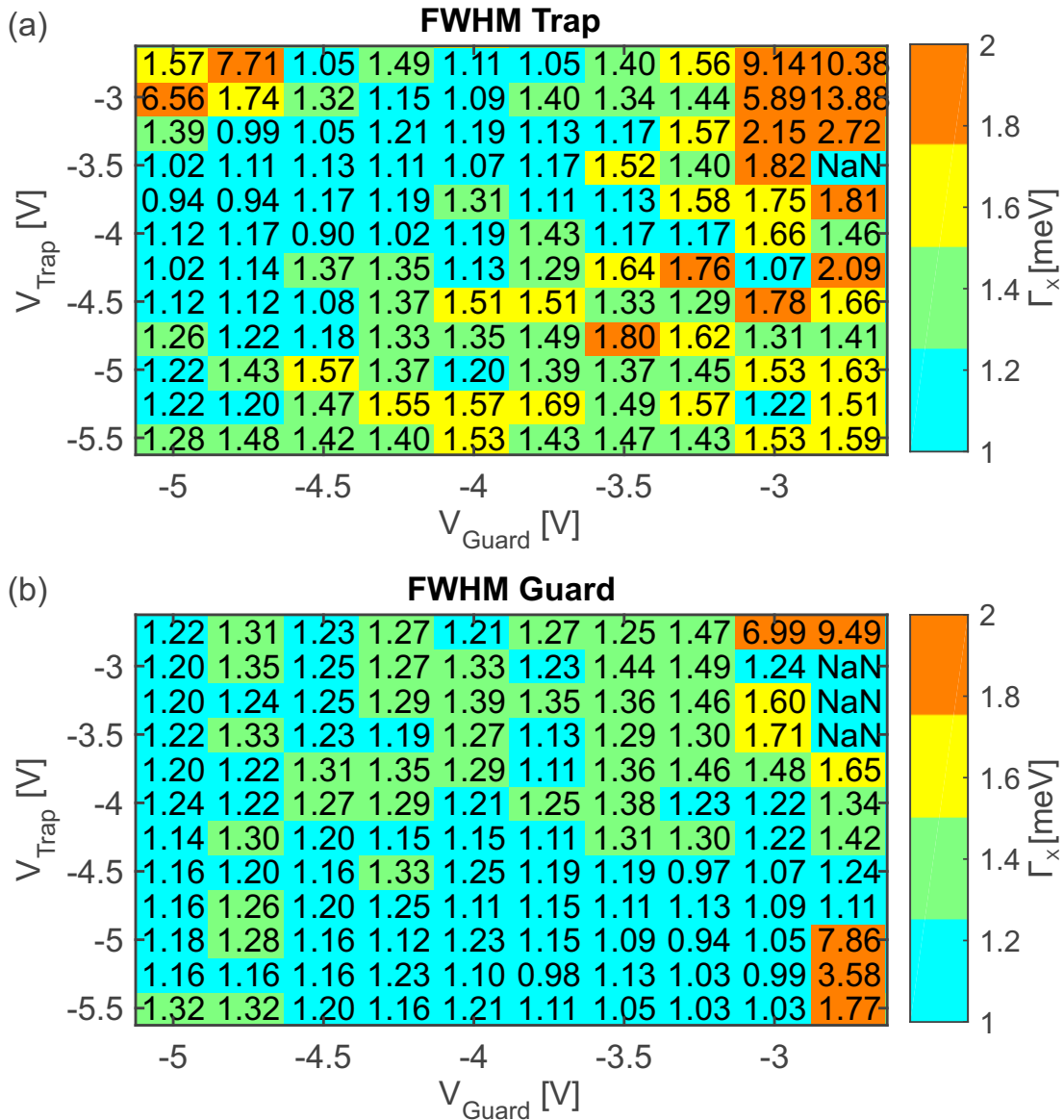


Figure 4.5: a) Map of the spectral linewidth Γ_x from the exciton cloud below the trap gate showing that the linewidth in the anti-trap configuration is narrower than in the trap configuration. b) Γ_x extracted from the cloud below the guard gate.

4.2 Trap stability

Excess charges from the laser excitation do not only lead to a broadening of the spectral linewidth. As already show in section 1.4, they can also accumulate at the heterointerfaces of our field-effect device, leading to an additional contribution to the externally applied electric field. Thus the trapping potential is altered for our measurement of the dipole moment. We have therefore performed a pump-probe measurement to quantify the influence of the excitation pulse on the trapping potential. The scheme is shown in figure 4.6. Using the pump excitation we first inject indirect excitons below the trap gate, and while while we vary the excitation power of the pump (see figure 4.6a and e) we monitor the spectral profile 200 ns after the extinction of the laser pulse (figure 4.6b and 4.6f) to ensure that the excitons populate the bottom of the trap. A line shaped laser excitation covering the trap and guard is then used to probe the potential of our trap. The line is 100 μm long and 10 μm wide, the excitation power is kept constant at $P_{\text{line}} = 400 \text{ nW}$, low enough to avoid perturbations of the potential. The probe pulse is 50 ns long and starts 200 ns after the pump pulse. By comparing the spectral profiles after the probe pulse for the three different excitation powers we investigate the influence of the pump excitation power onto the potential landscape. The results are plotted in figure 4.6f and 4.6g.

The spectral profile directly after the pump laser (see figure 4.6e) excitation shows a significant blueshift of 2 meV at the highest laser power of 1 μW with regard to the lower excitation powers of 50 nW and 200 nW. The relative blueshift between the two lowest excitation powers is 0.5 meV which is also the spectral resolution of our spectrometer. Thus, they can not be distinguished independently. Figure 4.6f shows that the spectral profiles all overlap 200 ns after the end of the pump laser excitation for all pump excitation powers. Since P_{ex} is increased by an order of magnitude we can thus safely assume that the trap bottom of the potential lies around 1519 meV. We can now verify that the pump excitation does not lead to a significant perturbation of the trapping potential by comparing the spectral profiles for the probe measurement at different pump excitation powers. The relative blueshift for the two highest pump excitation powers of 200 nW and 1 μW is 0.5 meV, at the spectral resolution limit. The two spectra are thus not distinguishable and the effect of the pump is therefore negligible. Nevertheless, for a pump excitation of 50 nW the probe measurement reveals a relative blueshift of 1 meV. However, given the huge overlap of all three spectra, it is safe to assume that the resonant excitation does not lead to a significant perturbation of the trapping potential for excitation powers up to 1 μW .

4 Electrostatic trapping of spatially indirect excitons

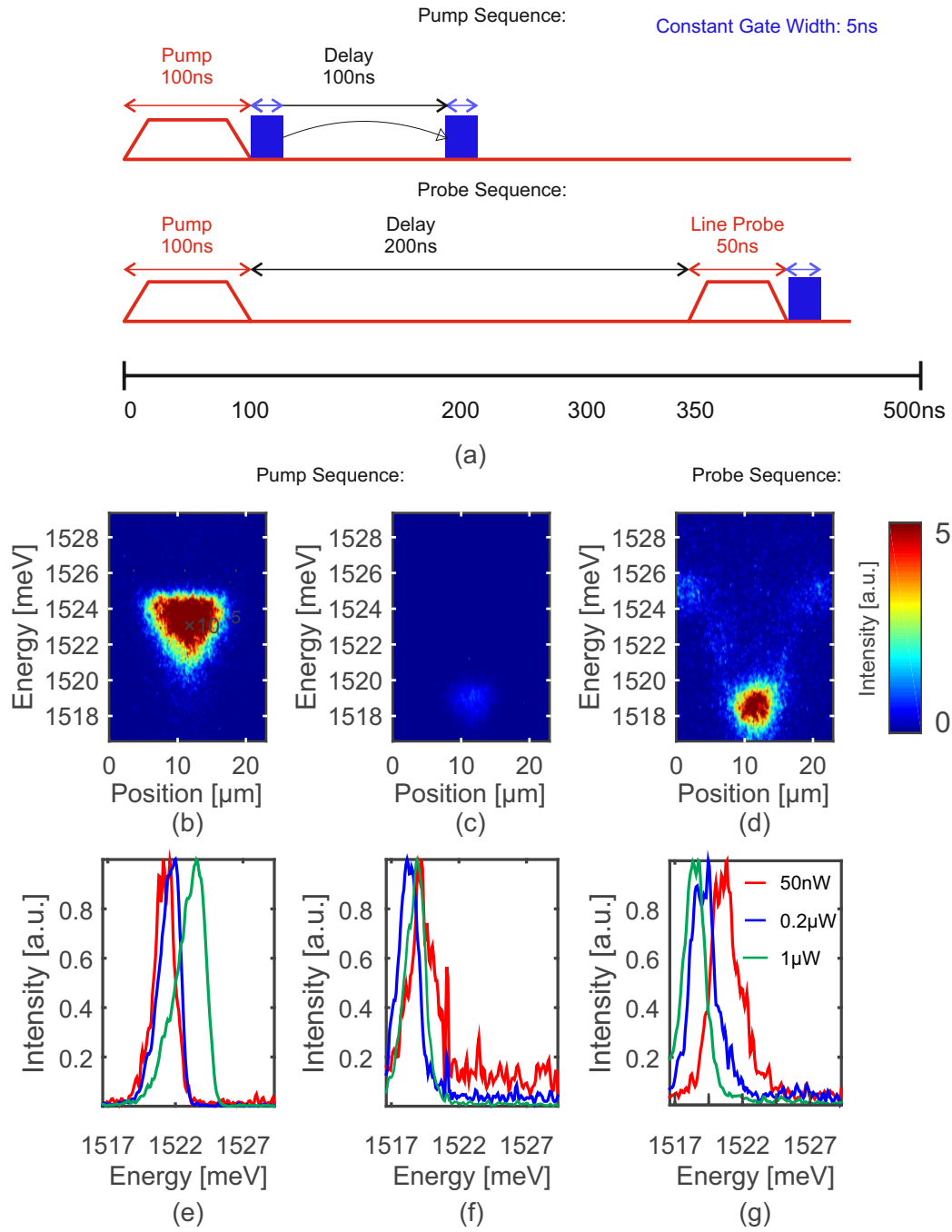


Figure 4.6: a) Sequence for pump-probe measurements b) Spectrally resolved image of the exciton cloud directly after the pump excitation c) 200 ns after the pulse when the cloud has settled at the bottom of the potential trap. Trap bias set to $V_{\text{Trap}} = -5\text{ V}$ and $V_{\text{Guard}} = -2.8\text{ V}$, $P_{\text{ex}} = 1\ \mu\text{W}$. d) Spectrally resolved image 200 ns after the pump excitation with the probe pulse on.. e-g) Respective spatial profiles for pump powers of 50 nW, 0.2 μW and 1 μW . The line excitation power was kept constant at $P_{\text{Line}} = 400\text{nW}$.

5 Trapped indirect excitons in the cold temperature regime

In chapter 4 we have demonstrated the successful realization of a trapping potential for spatially indirect excitons by exploiting their electric dipole. The main objective now is to inject a cold gas of indirect excitons at sufficiently high densities in order to observe the transition towards a Bose-Einstein condensate. In this chapter we report on the results of our photoluminescence experiments in a GaAs double quantum well aimed towards the achievement of this goal.

When trying to inject a cold gas of indirect excitons it is not advisable to use a continuous wave excitation laser. A continuous wave excitation leads to a local permanent heating of the exciton gas through the injection of hot carriers. As we have seen in chapter 4, these laser injected excess charges also contribute to the inhomogeneous broadening of the photoluminescence profile. We are therefore making use of a pulsed laser excitation. This will allow us to load a gas of indirect excitons into our electrostatic trap and to observe the density decrease through radiative recombination. In order to load the trap as homogeneously as possible, we adjust the waist of the laser beam in our experiments such that it covers the entire trap gate. This should also suppress the role of exciton transport and homogenize the density distribution. At the same time this ensures a homogeneous distribution of the excess charges as well.

Before we discuss the results of our measurements it is helpful to call back in to mind what one should expect when a gas of indirect excitons enters the quantum regime. As explained in chapter 2, the dark states lie energetically lower than the bright states. Therefore we anticipate a loss of photoluminescence due to the stimulated scattering from bright to dark states, which can not be attributed to the lifetime of the bright and dark state population.

5.1 Measuring the indirect exciton population in the trap

We extract the total exciton density in the trap by measuring the photoluminescence energy emitted by the trapped indirect excitons at different delays after the laser excitation. The density is extracted by comparing the energy of the photoluminescence at a given delay with the energy measured at a delay very long after the laser excitation, where the gas is very dilute. In order to be able to extract the density one again has to consider the two factors that determine the shift ΔE_{Peak} of the luminescence maximum

$$\Delta E_{Peak} = V_{dip} + \Delta E_X \quad (5.1)$$

where V_{dip} denotes the dipole-field interaction of the excitons while ΔE_X corresponds to the repulsive dipole-dipole interaction between the excitons. At long delays the contribution coming from the repulsive interaction becomes negligible and we can attribute this value to the bottom of our trapping potential. The interval of confidence for this approach is given by the two models used to quantify ΔE_X . The plate capacitor formula which underestimates the total population gives us a lower bound while the model which includes the repulsive exciton-exciton interaction sets the upper bound for n_{IX} . Let us note that we have shown in section 4.2 that excitation powers up to $1\mu W$ with a pulse length of 50ns do not lead to a significant alteration of the trapping potential. This is a critical prerequisite in order for the results to be comparable. Therefore our

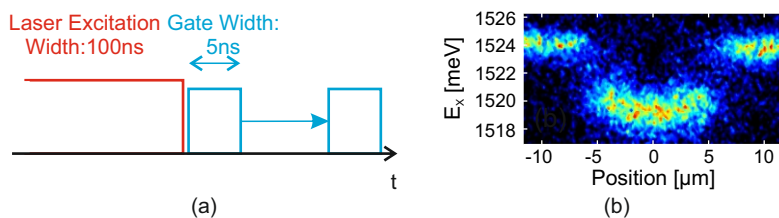


Figure 5.1: a) Measurement Sequence: A 100 ns long laser excitation with $P_{ex} = 1\mu W$ and gaussian beam shape is used to populate the trap with spatially indirect excitons. The photoluminescence is recorded with our spectrometer at different delays after the end of the laser pulse. b) Spatial profile of the confining potential realized at $T_B = 330\text{mK}$. The confinement profile is measured by injecting a very dilute and linearly shaped cloud of indirect excitons, along the horizontal axis of the trap.

measurement sequence is as follows (see figure 5.1a). We inject indirect excitons at the position of the trap gate. The electrostatic trapping potential is realized

5.1 Measuring the indirect exciton population in the trap

by setting the gate voltages to $V_{Trap} = -4.8V$ and $V_{Guard} = -3.5V$ which gives a trap depth of around 5 meV (see figure 5.1b). The excitation power of the laser with gaussian beam profile is set to $1\mu W$. We then record spectra for various delays after the end of the laser pulse to obtain information about the dynamics of the exciton population.

5.1.1 Extracting the density at 330mK

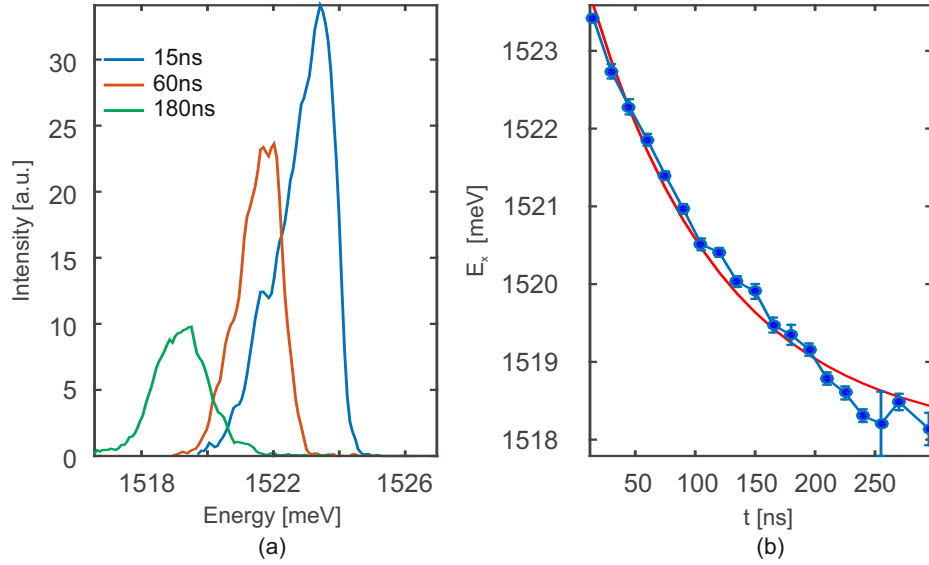


Figure 5.2: a) Spectra recorded for three different delays after the end of the laser excitation revealing the decay of the excitation via the blueshift and reduced intensity for longer delays. b) Dynamics of the PL-energy versus time at 330 mK (blue curve) revealing an overall blueshift of 5 meV. The red curve is an exponential fit with a time constant of 110 ns showing that the measured photoluminescence deviates from a simple exponential decay. All spectra are an statistical average of 10 single spectra per delay.

Figure 5.2 shows the dynamics of the photoluminescence energy after the laser excitation. The measurements were taken with the sample cooled down to $T_B = 330\text{ mK}$. We record the spectra after the laser excitation and extract the energy peak for each spectra. Figure 5.2a shows three exemplary spectra taken at different delays. The decay of the exciton population is directly observable via the redshift of the photoluminescence peak and the decline of the intensity. Extracting the energy peak E_x , as shown in figure 5.2b, for all delays shows that the evolution of the exciton population is close to an exponential decay suggesting that the radiative recombination of indirect excitons is the dominant decay channel. However, the curve can not be properly fitted with an exponential function. It is important to stress the deviation from a simple exponential decay

5 Trapped indirect excitons in the cold temperature regime

since this shows that the decay dynamics of the exciton population can not simply be explained through radiative recombination alone but rather through the more complex scattering processes, notably the ones coupling bright and dark states. Figure 5.2 also reveals that the amplitude of the blueshift is approximately 5 meV which matches the depth of our trapping potential. This shows that we have completely filled the trap with indirect excitons.

We can now conclude that we are able to trap a gas of indirect excitons with a density on the order of $n_{IX} \approx 1 - 5 \cdot 10^{10} \text{ cm}^{-2}$. This lies above the critical density at 330 mK for which the formation of an exciton BEC is anticipated. Furthermore we get a density parameter of $5n_x a_x^2 \approx 0.25$, a_x being the exciton Bohr radius, which is in the density regime where excitons can be well described as bosons, a necessary prerequisite for the formation of a BEC of excitons [20, 17].

5.1.2 Density dynamics at higher Temperatures

Figure 5.3 shows the evolution of the population at higher temperatures. We can see that in the first 50 ns there is a slight difference in the photoluminescence energy which can be attributed to the photocurrent which needs at least 50 ns to decay due to the RC time constant of our coaxial cables (see section 6.3). The transient current alters the internal field thereby modifying the initial photoluminescence energy. At longer delays we can see that the evolution of the photoluminescence energy with time does not depend on the bath temperature. Since the trapping potential is not influenced by the excitation laser we can conclude that we can inject a fixed density of excitons up to a temperature of 3.5 K . For higher temperatures the photoluminescence changes also for later delays which means that the trap profile has also changed. We therefore limit our studies to the regime where the density is constant in order to retrieve comparable results.

It is somewhat expected that the total exciton density remains constant since the laser excitation is blue detuned by 20 nm from the indirect exciton emission. This corresponds to 40 meV or 400 K of excess energy which is dissipated when a direct exciton is converted to an indirect exciton. Therefore the contribution of the bath temperature below 3.5 K is negligible in this relaxation process that is dominated by exciton-exciton scattering and the emission of longitudinal optical and longitudinal acoustic phonons. When we model the decay of E_X with a single exponential decay we get a time constant $\tau_{E_X} = 110\text{ ns}$ which does not vary significantly between 330 mK and 3.5 K . At this point it has to be mentioned

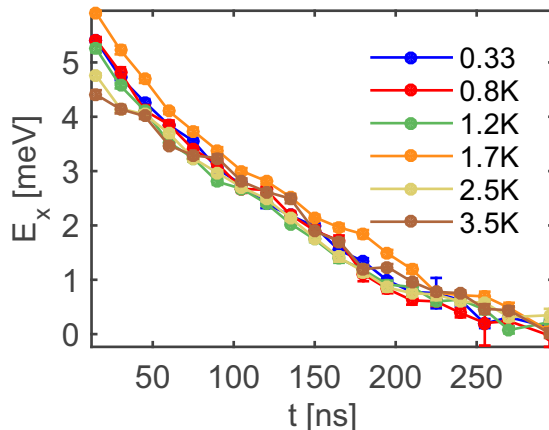


Figure 5.3: Evolution of the PL-energy vs time at higher temperatures. Showing that the blueshift of 5 meV is maintained at higher temperatures, showing that the density is kept constant at higher temperatures.

that we have to adjust the voltage for the trap gate at each temperature in order to end up at the same photoluminescence energy. Nevertheless the change never exceeded $0.1V$ between 0.33 mK and 3.5 K , and its influence on the density is therefore negligible. Beyond 3.5 K we have to adjust the trap voltage even further, indicating that we can not maintain the same trapping potential.

5.2 Studying the luminescence linewidth

As discussed in subsection 4.1.4, the photoluminescence linewidth reflects the time coherence of excitons in the light cone, the $\vec{k} = 0$ state. A priori it is given by the strength of the interaction between longitudinal-acoustic phonons and excitons as well as the repulsive dipolar interaction among the excitons. Further inhomogeneous broadening due to free carriers and impurities can lead to inhomogeneous broadening of the photoluminescence. In general we record the spectra by accumulating 10 spectra and extract the linewidth from the averaged spectrum. Figure 5.4a shows the evolution of the linewidth Γ_x versus time at 330 mK . We see an initial drop of the linewidth from 1.5 meV to 1.1 meV during the first 50 ns which we attribute to the thermalisation of the excitons and the decay of the photocurrent. This takes place during the same time interval since we have seen that an accumulation of charges in the trap broadens the spectral profile. For longer delays the linewidth variation vanishes despite a significant decrease of the exciton density through radiative recombination. Therefore the homogeneous broadening due to dipolar repulsive interactions is very weak. We can therefore conclude that the dipolar interaction is not very strong in the density regime observed. This is a promising result since BEC is expected to occur in a

5 Trapped indirect excitons in the cold temperature regime

weakly interacting regime, as realized in our experiments where interactions are weak. Nevertheless, the linewidth in our experiments is still too large for a BEC of indirect excitons which is expected to be on the order of $100 \mu\text{eV}$ [90]. We have therefore repeated the measurement in a different way. Rather than extracting the linewidth from one averaged spectrum of 10 images, we now extract the linewidth from each image and calculate the statistical average. The result is plotted in figure 5.4a as well for comparison. Quite remarkably this approach narrows the obtained linewidths by up to 0.5 meV , the narrowest linewidth being 0.6 meV . This lies within the order of magnitude were collective quantum effects are expected.

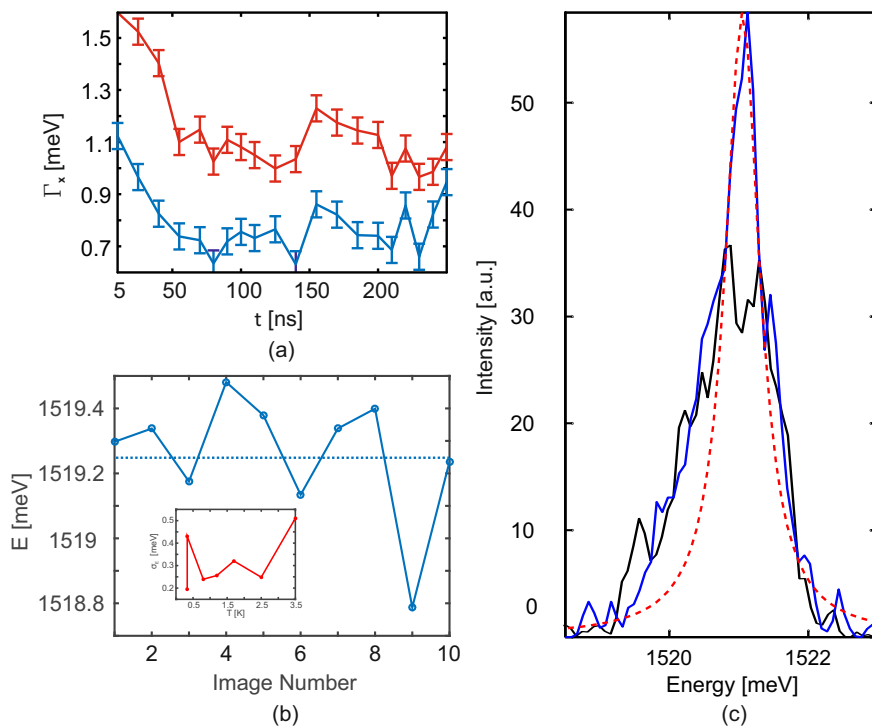


Figure 5.4: a) Dynamics of the spectral linewidth at 330 mK obtained from the averaged spectra (red) and the statistical average of the linewidth from the 10 individual spectra (blue). The latter approach yields a significant reduction of up to 0.5 meV due to inhomogeneous broadening. b) Fluctuation of the spectral peak for 10 images, showing deviations from the mean of up to 0.6 meV . The fluctuation of the spectral profile broadens the average spectrum. The inset shows the standard deviation of the spectral peak vs the bath temperature. c) Photoluminescence spectra measured 185 ns after the laser excitation in a one-minute interval (blue) or by averaging over 10 minutes (black). It shows a linewidth narrowing from 0.84 meV for the long exposure image to 0.4 meV for the shorter exposed image. The dashed red line shows a Lorentzian fit with $\Gamma_x = 0.3 \text{ meV}$.

The difference in the computation is related to a spectral diffusion of the photoluminescence signal due to long term fluctuations in the trapping potential. In order to quantify these fluctuations we have recorded 10 consecutive spectra to

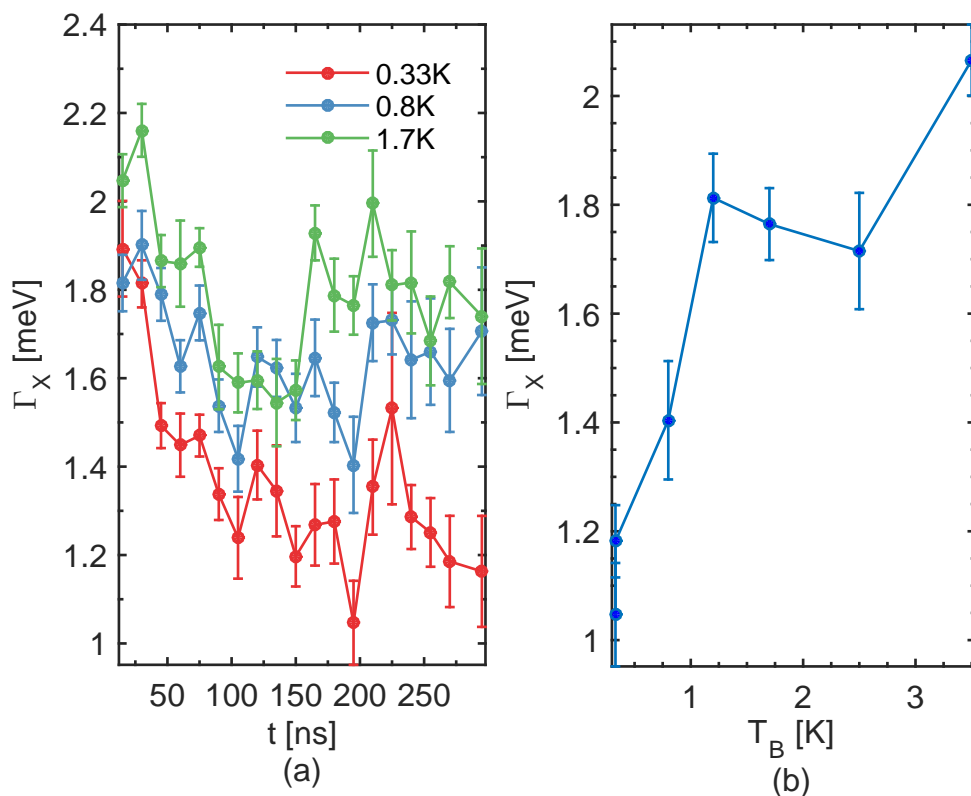


Figure 5.5: a) Evolution of the linewidth Γ_X with time for higher temperatures. b) Influence of the temperature on the linewidth Γ_X . All linewidth are extracted from an averaged spectrum of 10 single spectra, 200 ns after the end of the laser pulse.

assess the consequence of the spectral diffusion. Figure 5.4b shows the positions of the 10 spectral peaks recorded 185 ns after the end of the laser pulse. As we can see the peak of the spectral profile can vary up to 0.5 meV . This is indeed on the same order of magnitude as the observed linewidth narrowing. The origins for the trap fluctuations are the excess charges from the photocurrent caused by the resonant laser excitation. To determine the exact influence one would need to perform a time resolved measurement of the current. Unfortunately this is not possible since to our knowledge there exists no current amplifier that allows for detection of currents on the order of picoampere with nanosecond time resolution. Nevertheless, looking at figure 5.4 where we have recorded two spectra with an exposure time of 1 min, we can deduce the time scale on which these fluctuations take place. The shorter exposure times yields a narrower linewidth of 0.4 meV compared to the 0.84 meV of the longer exposed image. The fluctuations become thus dominant on a time scale of minutes. After discussing the evolution of the linewidth at 330 mK it is necessary to examine the influence of the bath temperature. Figure 5.5 shows a plot of the linewidth Γ_X vs the bath temperature T_b 200 ns after the laser pulse. It clearly shows an increase of the linewidth

when the bath temperature is raised. This is expected since raising the bath temperature increases the interaction between the gas of indirect excitons and longitudinal acoustic phonons. This interaction leads to an increased dephasing of excitons from the center of the light cone resulting in a broadened linewidth. It is worth mentioning that we are able to measure this behavior despite the challenges imposed by the spectral diffusion. Thus, the measurements show that the gas temperature is lowered when the bath temperature is decreased.

5.3 Probing the spatial profile of the exciton gas

To confirm the previous results, showing a cooling of the exciton cloud, we analyze the dependence of the bath temperature on the spatial profile of the exciton cloud from the spatially resolved spectrum (see figure 5.6a). Figure 5.6b shows the spatial profiles of the exciton cloud for the lowest temperature at 330 mK and at 2.5 K 185 ns after the end of the laser pulse. It can be seen that the spatial width defined as the full width at half maximum is considerably smaller at the coldest bath temperature. We have therefore investigated the influence of the bath temperature on the spatial width of the cloud. Figure 5.6c shows that the exciton cloud contracts by almost 40% from its initial size of $7.6 \mu\text{m}$ as T_b is decreased from 3.5 K to the lowest bath temperature of 330 mK. This is consistent with the cooling of an exciton gas that accumulates at the trap center where the potential has its minimum. The blueshift of around 4 meV at this point yields a density on the order of $n_{\text{IX}} = 10^{10} \text{cm}^{-2}$ for a trap depth of 5 meV (see figure 1.5) for both 2.5 K and 0.33 mK. Thus, the spatial distribution confirms the spectral analysis that the exciton gas is cooled down by decreasing the bath temperature.

5.4 Studying the distribution between dark and bright states

We now study exclusively the bright exciton population dynamics through their photoluminescence for different temperatures. Comparing these with the dynamics of the blueshift should give further insight about the global distribution between bright and dark states since the density of excitons is kept constant at all temperatures in our experiments. Figure 5.7a and b show that around 100 ns after the laser excitation, the peak intensity and integrated intensity I_x of the

5.4 Studying the distribution between dark and bright states

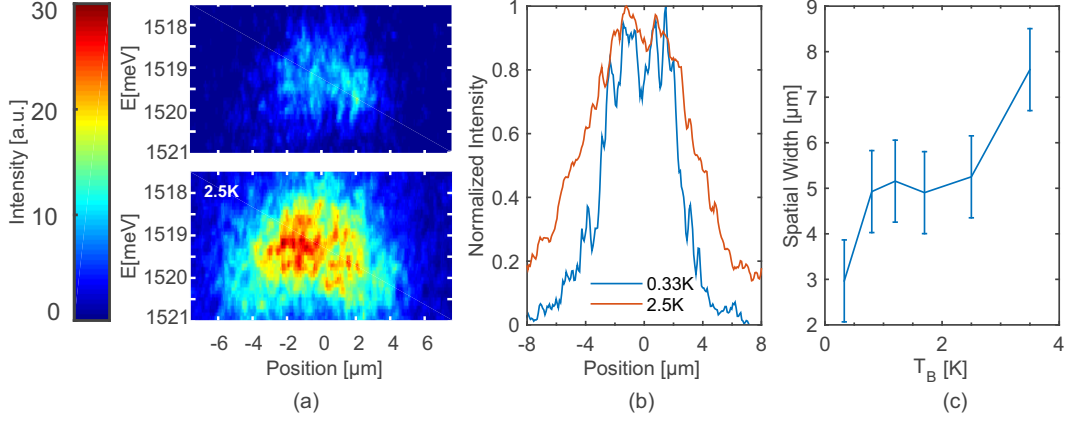


Figure 5.6: a) Spatially resolved spectral image of the exciton cloud in the trap for b) Spatial profile of the exciton cloud extracted from the spectrally resolved image at 330 mK (blue) and 2.5 K (red). c) Spatial width versus temperature showing the contraction of the exciton cloud as the bath temperature is lowered. Both profiles are taken 185 ns after the extinction of the laser pulse.

photoluminescence recorded at 330 mK deviates towards lower values compared to the curve recorded at 2.5 K. This indicates that the population of bright excitons is reduced when the bath temperature is lowered. We have thus investigated the influence of the bath temperature on the integrated intensity. Figure 5.7c confirms that the integrated intensity is reduced by a factor of 3 between the 3.5 K and 0.33 mK. This contradicts the behavior for a classical gas of indirect excitons obeying the Maxwell-Boltzmann energy distribution. Intuitively one expects that, as the bath temperature is lowered, the Maxwell-Boltzmann distribution shifts towards lower energies, the bottom of the light cone, and thus more excitons should populate the radiative zone. Consequently the integrated intensity should show an increase when the bath temperature is lowered. However our measurements do not reflect this scenario, but the opposite.

Looking at the time evolution of the integrated photoluminescence I_X (see fig. 5.7d) we can extract the optical decay times τ_{opt} for each bath temperature by fitting them with a mono exponential decay. We find that the optical decay time τ_{opt} decreases when the bath temperature is lowered (see inset fig. 5.7d). For the highest temperature the optical decay time is similar to the decay time of the photoluminescence energy E_X on the order of 100 ns indicating that the population of bright excitons decays as fast as the combined population of bright and dark excitons which is expected. Furthermore we also see that the optical decay time saturates for temperatures below 1.5 K as predicted for a Bose gas of excitons in a CQW, i.e. a statistically degenerate gas [42]. On the contrary for a classical gas obeying Maxwell-Boltzmann statistics it should show a linear decrease of the optical decay time when the bath temperature is lowered, as

5 Trapped indirect excitons in the cold temperature regime

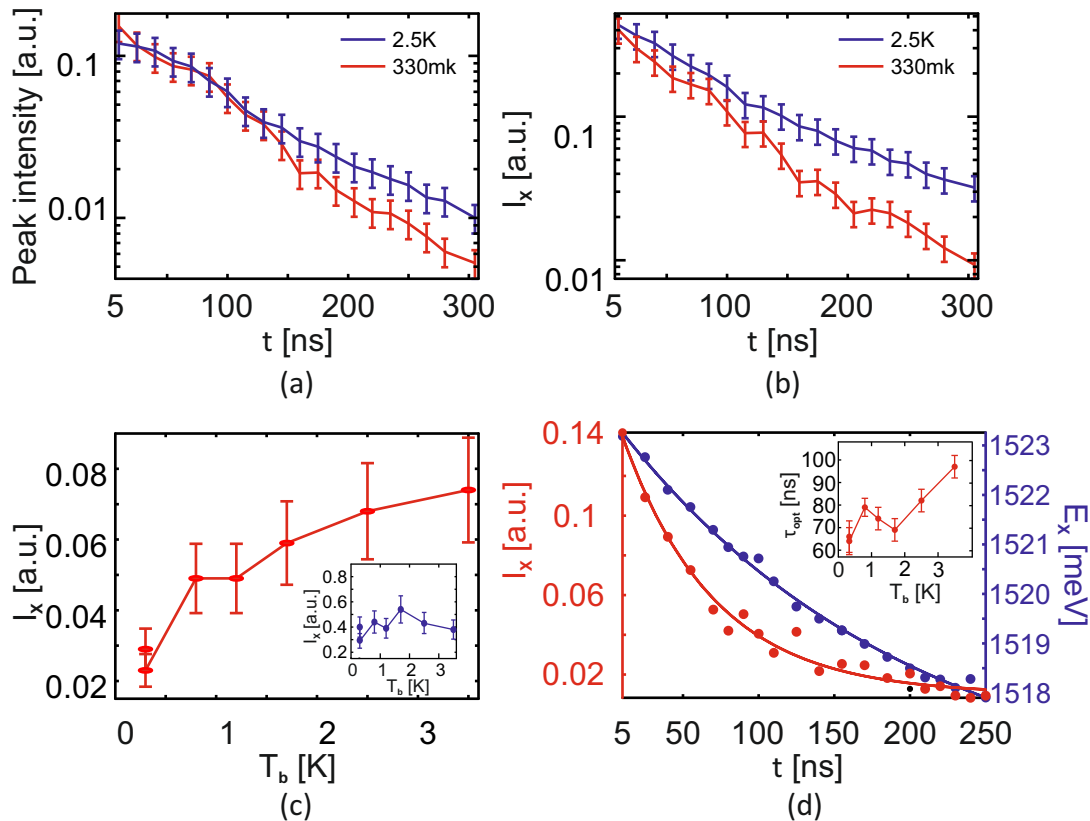


Figure 5.7: a-b) Peak and integrated intensity of the exciton cloud with time for 330 mK (red) and 2.5 K (blue). Around 100 ns after the laser pulse the photoluminescence at 330 mK shows a drop for both integrated and peak intensity. c) Integrated intensity I_X of the exciton cloud 190 ns after the end of the laser pulse versus temperature showing a decrease as the bath temperature is lowered. The inset shows the integrated intensity vs temperature directly after the laser pulse. The variation is negligible, thus indicating a cooling of the gas of indirect excitons. d) Evolution of the integrated intensity I_X and the spectral peak E_X . At 330 mK the time constant for I_X is shorter than for E_X showing that the bright exciton population decays faster than the total population of excitons. The inset in figure d) shows that the time constant for I_X decreases as the bath temperature is lowered.

theoretically predicted [6]. Also note that the integrated intensity does not vary much directly after the excitation pulse (inset figure 5.7c). This first analysis confirms again that the gas of excitons is not thermalised after the laser pulse.

In order to gain further insight about the total exciton population we compare the density of bright excitons using their optical decay time, extracted from the integrated intensity, to the dynamics of the blueshift E_X in figure 5.7d. As already shown before, in our experiments we always load our trap with a fixed density of excitons below a temperature of 3.5 K. When we lower the temperature we can conclude from the decrease of the optical decay time that the bright exciton population gets depleted. To account for the constant density with a diminished

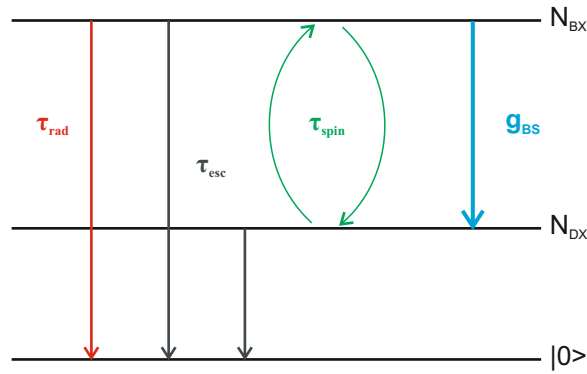
bright exciton population we consequently have to conclude that the majority of excitons occupy non-radiative states, the dark states, which do not couple to light. Since the optical decay time matches the decay time of the blueshift at 3.5 K we can assume that we are in a classical regime, such that the exciton population of the dark states is equal to the population of the bright states. We can then deduce by comparing the decay times at 330 mK that approximately 20% of the excitons occupy the bright state while the remaining population occupies the dark state. This is highly non-classical, since the splitting between dark and bright states does not exceed $5\mu\text{eV}$ which is much lower than the thermal activation energy of $28\mu\text{eV}$ at our lowest bath temperature of 330 mK.

5.5 Modeling the dynamics between the dark and bright states

Until now we have extracted quantitative results from the photoluminescence and blueshift decays through simple mono exponential fitting. In this section we present a simple model to see if the data is consistent with a Bose stimulation from bright to dark states by modeling the populations of the bright and dark states through a rate equation model which considers coupling between bright and dark states and population decay. The coupling is modeled through spin flips and through Bose stimulation from the bright to the dark states. The population decay also includes radiative combination and non-radiative decays. A scheme of the model together with the resulting rate equations are shown in figure 5.8.

In the rate equations τ_{rad} denotes the optical decay time, τ_{spin} the time characterizing spin flips which converts bright to dark excitons and vice versa, τ_{esc} is the time constant characterizing the non-radiative loss of exciton population and g_{BS} , a bosonic stimulation factor proportional to the dark exciton population. We model the decay starting from 70 ns after the laser excitation has ended in order to ensure that we are not influenced by the transient photocurrent or the thermalisation of the excitons. We model our experimental results for two temperatures. The lowest bath temperature at 330 mK and for 2.5 K. For the lowest temperature we include the effect of Bose-Einstein statistics while we discard this effect at 2.5 K by setting $g_{BS} = 0$. In table 5.1 we have compiled the model parameters. The radiative decay rate was set to be on the order of the experimentally observed values. The spin flip rates are in good agreement with recent research results that estimate the spin-flip rate to be on the order of 10^2 ns [56, 50, 9]. The output of the modeled photoluminescence is plotted in figure

5 Trapped indirect excitons in the cold temperature regime



$$\frac{dN_{BX}}{dt} = -\frac{N_{BX}}{\tau_{rad}} - \frac{N_{BX}}{\tau_{esc}} - \frac{N_{BX}}{\tau_{spin}} + \frac{N_{DX}}{\tau_{spin}} - (g_{BS}N_{DX})N_{BX}$$

$$\frac{dN_{DX}}{dt} = -\frac{N_{DX}}{\tau_{esc}} + \frac{N_{BX}}{\tau_{spin}} - \frac{N_{DX}}{\tau_{spin}} + (g_{BS}N_{DX})N_{BX}$$

Figure 5.8: Our model considers the bright and dark exciton manifold N_{BX} and N_{DX} respectively. The two levels are coupled through spin flips that can convert bright to dark excitons and vice versa characterized by τ_{spin} . At low enough temperatures the Bose-Stimulation g_{BS} has to be introduced to account for the observed dynamics. The depletion of the bright excitons is characterized by the optical decay time τ_{rad} while the depletion of the dark exciton population is characterized by τ_{esc} .

5.9a together with the measured integrated intensity I_x . We can see that our model reproduces the dynamics of the photoluminescence quite well. At 330 mK in particular we are only able to reproduce the drop in the photoluminescence intensity where Bose stimulation is included. Our model is also in good agreement for the measurements at higher temperatures where we just accounted for the increased radiative lifetime as theoretically predicted while setting $g_{BS} = 0$ [42]. Next we have attempted to model the decay of the photoluminescence energy. Figure 5.9b shows that we do not reproduce the decay of the population through the blueshift as well. We attribute this to the lack of tools available that allow for a more precise estimation of the exciton density.

From the model we extract the population distribution using the evolution of the exciton blueshift E_X . We assume an equal population of bright/dark states in the beginning. The results plotted in figure 5.10 show that our model also allows us to reach a correct level of agreement for the total population of excitons in our trap. This becomes evident looking at figure 5.10a which shows the model results at 330mK. When we include bosonic stimulation we are again able to account for the steep drop in the bright exciton population. However, if we set this term to zero, meaning we assume a population that behaves according to a classical gas, we are not able to reproduce this intensity drop. Let us note that the initial rise

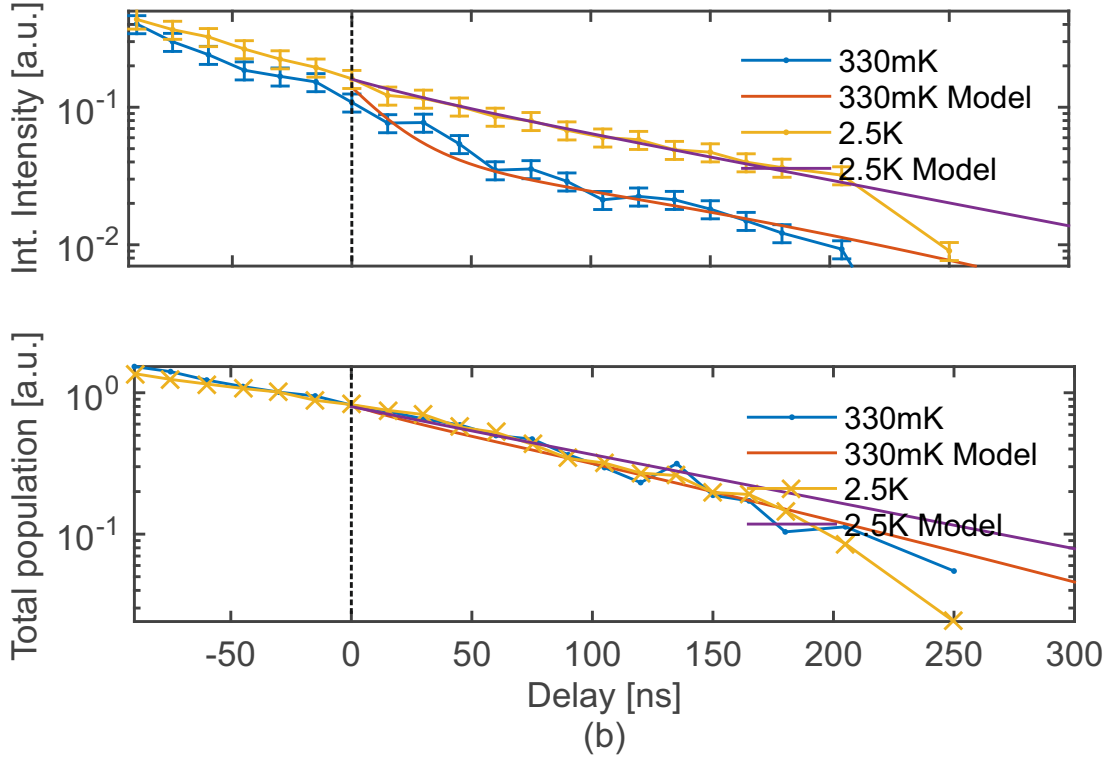


Figure 5.9: a) Results of the model for the photoluminescence together with the measured data showing a good level of agreement for 330 mK and 2.5 K. b) Results of the model for the total population plotted together with the total population extracted from the measured blueshift. The dashed line marks the beginning of the simulation 70 ns after the end of the laser excitation.

in the dark population is absolutely coherent with a decaying bright population in the beginning while the blueshift, mapping the total exciton population, decays on a slower time scale. In figure 5.10b we show the evolution of the exciton population for a bath temperature of 2.5 K where we have set $g_{BS} = 0$. The plot shows that bright and dark states decay equally as expected for a classical gas of excitons.

Despite its simplicity, the results of the simulations show that our model is quite suitable to reproduce the photoluminescence dynamics of the excitons. In particular the phenomenological simulation shows that Bose stimulation is needed to account for the initial drop in the integrated photoluminescence together with a rise in the dark state population which explains the slower time decay of the blueshift compared to the decay of the photoluminescence. Unfortunately we can not fully reproduce the decay of the blueshift with our model. We attribute this flaw to the lack of a suitable model that allows for a more precise estimation of the exciton density.

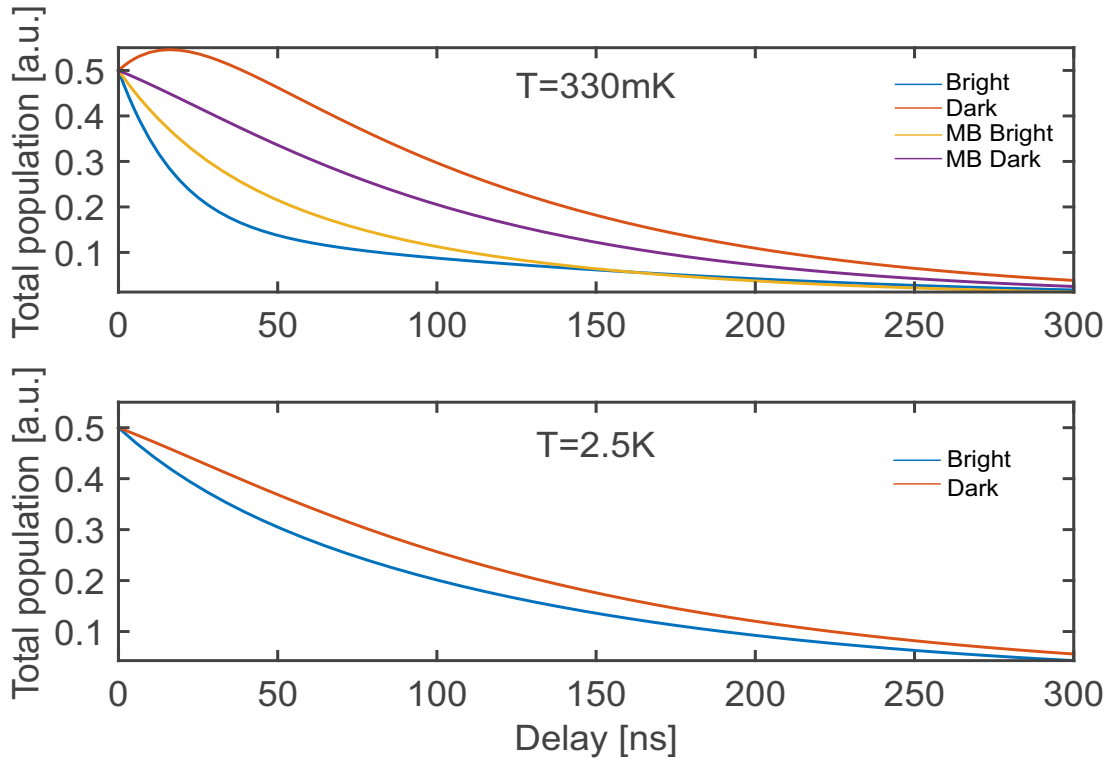


Figure 5.10: Phenomenological model to simulate the evolution of the bright and dark states with time, a) at 330 mK with and without Bose stimulation showing Bose stimulation is needed to account for an initial drop in the photoluminescence b) at 2.5 K showing that the dark/bright population decays with a similar time constant.

| | τ_{rad} [ns] | τ_{esc} [ns] | τ_{sf} [ns] | g_{BS} [$\frac{1}{\text{ns}}$] |
|---------|--------------------------|--------------------------|-------------------------|---|
| 0.33 K | 70 | 175 | 100 | $\frac{1}{27}$ |
| 2.5 K | 150 | 210 | 80 | 0 |
| MB Low | 70 | 175 | 100 | 0 |
| MB High | 140 | 200 | 100 | 0 |

Table 5.1: Overview of the model parameters

5.6 Conclusion

In this chapter we have provided photoluminescence measurements on cold exciton gases confined in an electrostatic trap. Quite remarkably we were able to show that below a temperature of 3.5 K our device allows for the studies of indirect excitons at a fixed density when the bath temperature is varied. This allowed us to compare the results when the bath temperature was varied. Spatially resolved spectral measurements revealed a narrowing of the spectral linewidth below 1 meV, 185 ns after the laser excitation, as the bath temperature is low-

ered. This linewidth narrowing coincides with a contraction of the exciton cloud by almost 50%. We can thus conclude that the temperature of the exciton gas drops as we lower the bath temperature.

This degree of control has allowed us to show that the population of bright excitons is anomalously decreased when the bath temperature is lowered. The observed dynamics contradict the expected behavior for a gas obeying Maxwell-Boltzmann statistics. In this case one would expect an increase of the bright exciton population within the light cone which should lead to an increased photoluminescence intensity. However the contrary is the case. The decay for the overall exciton population stayed constant while the optical decay time showed a decrease when the bath temperature is lowered suggesting a stimulated scattering towards the energetically lower dark states. We have thus provided a model for the exciton populations which shows that the observations can be accounted for by introducing a Bose-Stimulation from bright to dark states at sub-Kelvin temperatures. This stimulated scattering would then of course be a precursor for a BEC which might occur in our experiments. Nevertheless, our observations are not able to unambiguously demonstrate the existence of a BEC through other quantum signatures. This would require a measurement of the spatial coherence of the bright excitons, 185 ns after the laser pulse, where the anomalous darkening of the exciton cloud is observed.

At these densities on the order of $n_{\text{IX}} = 10^{10}\text{cm}^{-2}$ it is expected that a fraction of bright excitons contributes to the condensate. This situation corresponds to the regime where a gray condensate is formed as theoretically predicted [21]. The coherence length would then be limited by the spatial extension of the condensate itself. The size of the condensate ultimately being restricted by the boundaries of our trap. In principle the coherent state should be reflected in the photoluminescence. Unfortunately we are not able to provide such a measurement since any spatial coherence would be blurred by intensity fluctuations, thus making it impossible to rule out that the spatial interference pattern is of pure quantum nature and not due to the intensity fluctuations. Furthermore any coherence from the bright part of the condensate would be blurred by the photoluminescence from bright excitons in the non-condensed thermal part of the exciton cloud. Assuming a condensate consisting of 90% of the total exciton population, with for instance 10% forming the bright part of the predominantly condensate, the photoluminescence signal would consist of equal coherent and non-coherent parts. Thus, depending on the ratio of condensed to non-condensed excitons, this might make any interference measurements impossible, even in the absence of intensity fluctuations. A possible route to obtain clearer signatures of exciton condensa-

5 Trapped indirect excitons in the cold temperature regime

tion could be a further reduction of the exciton gas temperature, however, as we will see in the next chapter, this can not be achieved by lowering the bath temperature as exciton-phonon interactions become less efficient.

6 Arbitrary in-situ control of the potential landscape

The original desire to achieve in-situ control of the potential explored by the excitons is based on potential applications in optoelectronics. In particular photo-generated dipolar excitons can act as a photonic memory which can release photons at will with up to sub-nanoseconds response times. Thus, excitons could be used to optical-interconnects [93, 88]. Furthermore, recent experiments show that the spin of the reemitted photon is stored in the light field. This provides a degree of freedom to encode information that can be transferred from an optical signal into a solid state platform [56, 50, 9]. The controlled transport of indirect excitons has been realized through electrostatic means, by employing a local field gradient inducing a long-range drift of the exciton cloud [29]. An alternative transfer mechanism relies on inducing surface acoustic waves (SAWs) on top of a field effect device. The resulting strain induced band-gap modulation induces a movement of the excitons along the propagation direction of the SAW [54, 53, 84].

Recently there has also been an interest in manipulating cold exciton gases for fundamental studies. This has led to the development of sophisticated trap designs that allow for studies of a cold gas of excitons, for instance by deploying a lattice geometry in order to study correlations, or a snowflake geometry that allows to rotate the exciton cloud [52, 69]. These devices have to operate on a sub-ns timescale due to the finite lifetime of the excitons. However, current techniques to achieve in-situ control of the electric field are subject to a major drawback. High-speed in-situ control of the electric field is currently achieved by means of impedance matching, since standard transmission lines have an impedance of $Z=50 \Omega$ while the resistance for a field effect device is typically on the order of $M\Omega - G\Omega$ [87]. Until now impedance matching has been realized by using low loss broad-band transmission lines in combination with a 50Ω termination resistor in parallel with the field effect device. The resistor has to be positioned as close as possible to the sample in order to effectively match the impedance. The downside of this approach is of course a significant heating as the energy of a high-speed pulse is ultimately dissipated in the 50Ω resistor.

In this chapter we present a novel approach that allows for in-situ control of the electrostatic potential landscape used to confine a cold gas of indirect excitons. The technique exploits the high-field seeking properties of the indirect excitons. We use a voltage pulse which varies the internal electric field, interacting with the excitons electric dipole. By determining the transfer function which links the voltage pulse to the response of the excitons photoluminescence energy in a deterministic manner, we are able to achieve arbitrary in-situ control of the potential explored by the excitons on the ns time scale. This level of control is maintained without suffering from heating effects due to passive electric components. Thus, our technique is suitable for the manipulation of a cold gas of dipolar excitons and could pave the way towards quantitative studies of exciton thermalization and possibly evaporative cooling of exciton gases in coupled quantum wells.

6.1 Exciton thermalisation and evaporative cooling

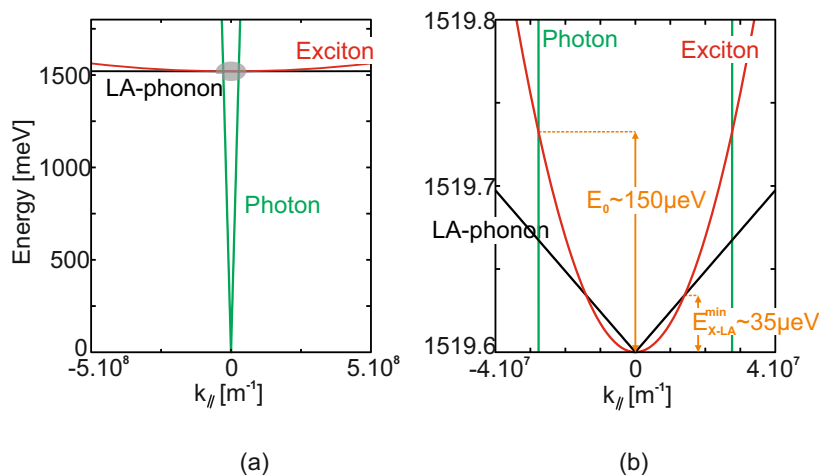


Figure 6.1: a) Global view of the dispersion relations for LA-phonons excitons and photons. b) Close-up picture of around $k = 0$ showing that exciton phonon-interaction has a lower boundary at $35 \mu\text{eV}$. Excitons below this kinetic energy can not emit a single LA-phonon to reduce their kinetic energy.

At low temperatures, the thermalisation of a dilute gas of excitons is dominated by the emission of longitudinal phonons [65, 44, 42]. The thermalisation process is even more efficient for excitons in confined two 2D since the in-plane momentum conservation is lifted [62]. Thus, dipolar excitons can couple to a continuum of phonons, leading to an enhanced cooling rate on the sub-ns scale in coupled wells compared to excitons in bulk which is on the order of nanoseconds [80, 79].

6.1 Exciton thermalisation and evaporative cooling

As a result long-lived dipolar excitons are expected to thermalise down to sub-Kelvin temperatures, where collective quantum effects are expected. However, the thermalisation process through exciton-phonon interaction is limited. This is shown in figure 6.1 which depicts the dispersion relations for LA-phonons, excitons and photons around the $k=0$ state. While momentum conservation is relaxed perpendicular to the quantum well plane, energy conservation must still hold for exciton-phonon interactions. As a result excitons in the $k=0$ state get scattered above a given energy determined by the minimum LA-phonon that an exciton can emit to lower its energy while energy conservation is fulfilled. This leads to the requirement $E_{Phonon,min} = \hbar v_s k_{phonon} = \frac{\hbar^2 k_x^2}{2m_x}$. Setting $k_x = k_{phonon}$ gives a minimum energy of $E_{Phonon,min} = 35 \mu eV$ corresponding to a temperature around 300mK ($v_s = v_{LA} = 5.29 \cdot 10^5 \frac{cm}{s}$ [62]). A further reduction of the gas temperature can only be achieved through second order processes as for instance the absorption of a phonon with an energy close to $E_{Phonon,min}$ followed by the emission of a phonon with higher energy. However, the probability of this second order process decreases exponentially with the bath temperature [80, 79]. Thus, exciton-phonon interaction is not efficient enough to lower the temperature of the exciton gas further down and a different cooling mechanism has to be implemented.

In the field of ultra cold atoms, evaporative cooling was used to cool a gas of neutral atoms below the critical temperature for BEC. However, this method is not restricted to neutral alkali atoms alone. Quite the contrary, the dynamics of evaporative cooling can be derived from rather simple considerations, applicable to a wide variety of particles [46]. Evaporative cooling is performed by lowering the potential walls of a trap confining a gas of particles in such a way that the hottest particles escape from the trap. The hottest particles leaving the trap are on the high tail of the Maxwell-Boltzman distribution. As a result they take a significant amount of kinetic energy out of the gas in the trap. The evaporative sequence has to be short enough to allow for a constant thermalisation of the remaining particles in the trap as the hottest particles escape the trap to mitigate the effects of the overall particle loss through an increase of the phase space density [46]. Thus, the timescale at which the potential walls are lowered is limited by the thermalisation time of the particles. The success of this approach is thus ultimately determined by two factors, the time the gas needs to thermalise, once the hottest particles have left the trap, and the overall trap lifetime.

Indirect excitons thermalise on a sub-ns scale while their lifetime can be on the order of up to microseconds. Thus, evaporative cooling is a promising approach to further actively cool a cold gas of excitons in a controlled manner [39], even

below the threshold of 300 mK imposed by the exciton-phonon interactions. The implementation requires the ability of in-situ control of the potential landscape without free from any detrimental heating effects.

6.2 Arbitrary high-speed control of the exciton confinement

Achieving high-speed control of the bias voltage for an arbitrary gate electrode, used to create indirect excitons, relies on three key components. To manipulate the internal electric field in-situ we need an arbitrary waveform generator (AWG) which is able to provide engineered voltage pulses on a much shorter timescale than the exciton lifetime, ideally on the nanosecond range. Furthermore, in order to deliver the voltage pulses as unperturbed as possible, we need ultra high frequency transmission lines that have well known loss and impedance characteristics and are suitable for applications in a cryogenic environment. At last we need a printed circuit board which extends the path from the transmission line just in front of the field effect device with well defined impedance.

6.2.1 The Arbitrary Waveform Generator

In our experiments we used an arbitrary waveform generator provided by Signadyne (SD AWG-H3344). It can deliver output voltages of up to 1.5 V at 50 Ω output impedance. The shape of the waveform can be manipulated with 1 ns precision. The AWG is operated through a labview program that has been designed as a part of this thesis. The waveform can be defined by a mathematical function or provided by an ASCII file. The latter option allows for the creation of custom waveforms with third-party software. The arbitrary waveform generator comes with a 10MHz reference output and an trigger channel that can be configured as trigger in or trigger out. The 10MHz reference output is used to synchronize the timebase of the AWG with the experimental master clock to avoid a time jitter between the two devices.

6.2.2 Coaxial Transmission Lines

The connection between the output of the AWG and the printed circuit board carrying the sample is realized in two stages. The first stage establishes a con-

6.2 Arbitrary high-speed control of the exciton confinement

nection between the AWG and the entry port of the electric feedthrough flange of the cryostat via an UHF coaxial cable with SMA connectors. The second stage is established through a coaxial cable suitable for cryogenic environments that connects the PCB and the inside of the electric feedthrough with SMB connectors. The choice for the cable inside the cryostat is vital to the success of our approach. It has to allow for high frequency signal transmission while showing low thermal conductance at the same time, in order to isolate the low temperature stages as good as possible from the room temperature environment. In the case of metals, unfortunately, the thermal conductivity scales with the electrical conductivity. Our coaxial cable consists of a 0.2 mm stainless steel core surrounded by a 0.2 mm thick Teflon insulation. The shielding is also made of braided stainless steel. The center conductor has a resistance of $23.62 \frac{\Omega}{\text{m}}$ whereas the outer jacket has a resistance of $3.62 \frac{\Omega}{\text{m}}$, for comparison coax cables based on copper have a resistance on the order of $0.5 \frac{\Omega}{\text{m}}$. Thus, one can directly deduce from these numbers that an arbitrary pulse sent by the AWG is strongly attenuated as it travels further down the cable due to the use of steel as center conductor. However, as already stated, this is necessary in order to have a good thermal insulation from the outside environment.

6.2.3 Design of the printed circuit board

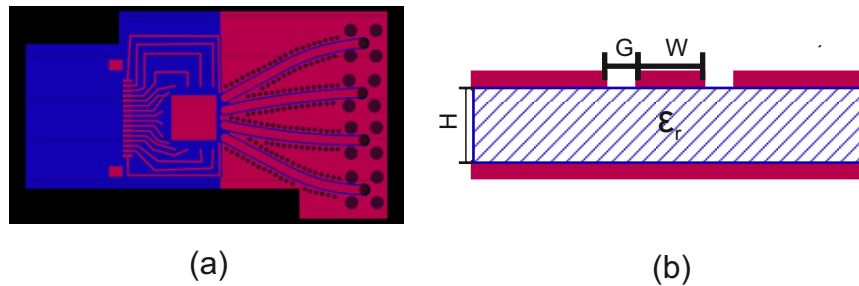


Figure 6.2: a) Layout of our Printed circuit board: On the left we have the copper pads to mount the write-to-board connector. The four signal traces are designed such that the impedance is 50Ω . The holes next to the impedance matched lines are added to improve overall thermalisation. b) Schematic of a conductor-backed coplanar wave guide. A dielectric is put between two layers of copper. The top layer is processed to mill out a signal trace surrounded by two grounded planes. The dimension in our case are $G=0.3 \text{ mm}$, $W=1.6 \text{ mm}$ and $H=1.55 \text{ mm}$. The dielectric layer is FR4, a standard epoxy resin with $\epsilon_r = 4.3$.

At the beginning of the design process for the PCB, one has to decide how impedance matching of the high-frequency signal trace should be realized. Various options such as striplines, microstriplines or slotlines exist to realize impedance matched transmission lines on a printed circuit board. Among these we have

selected the conductor-backed coplanar waveguide to be deployed on our printed circuit board since it allows for wide-band impedance matching without a drastic increase of losses [76]. Furthermore this approach allows for a compact realization of many impedance matched signal traces next to each other. Figure 6.2a shows a sketch of a conductor-backed coplanar waveguide. It is made of two metal layers separated by a dielectric material. Conventional coplanar waveguides consist of a signal trace between two ground planes, which are called the return conductors. Signal trace and return conductors are electrically isolated from each other. Adding an additional grounded bottom layer results in the conductor-backed coplanar waveguide. The impedance of the signal trace is determined by various factors like the height of the different layers, the conducting material and the dielectric. The main factor which determines the impedance of this type of transmission line is given by the ratio between the width W of the signal trace and its distance G to the ground plane(see figure 6.2b). Numerous software packages exist that assist in the design of impedance matched traces for waveguides on PCB. In this thesis we have used the freeware TXLine[©] to calculate the dimensions of the signal traces and used a PCB layout editor to design the board. The board layout is shown in figure 6.2b. The top and bottom layers consist of a 35 μm thick gold coated copper layer. They are separated by a 1.6 mm dielectric material. The material is FR4, a standard epoxy laminate which is nowadays used for the majority of rigid PCB's. These values determine that the signal trace must be 1.6 mm wide, with a separation gap of 0.3 mm to the return conductor for an impedance of 50 Ω at 1GHz. Let us note that the calculations show that the impedance changes less than 1% in the range of 1 to 4 GHz for our layout. The traces of the PCB are connected by surface mount through hole SMA connectors. The plated through holes along the signal traces and the gold coating have been added to ensure proper thermalisation of the PCB.

6.3 Characterization of the Components

To quantify the response time it is necessary to characterize the frequency response of each component. A spectrum analyzer was used to make sure that the coaxial cable outside of the cryostat shows no transmission losses up to 2 GHz. The same holds true for the printed circuit board. This comes at no surprise since standard coaxial cables show no significant losses around these frequencies. Furthermore we have kept the distance between frequency generator and the feedthrough flange as short as possible since the losses scale with the length of the cable. The losses on the PCB are negligible since no trace is longer than

5 cm and according to the calculation with our software the losses for our traces are on the order of $2 \frac{\text{dB}}{\text{m}}$. A priori this gives us an upper limit of the rise time of 0.5 ns. Losses occur mainly in the coaxial cable inside the cryostat. This is

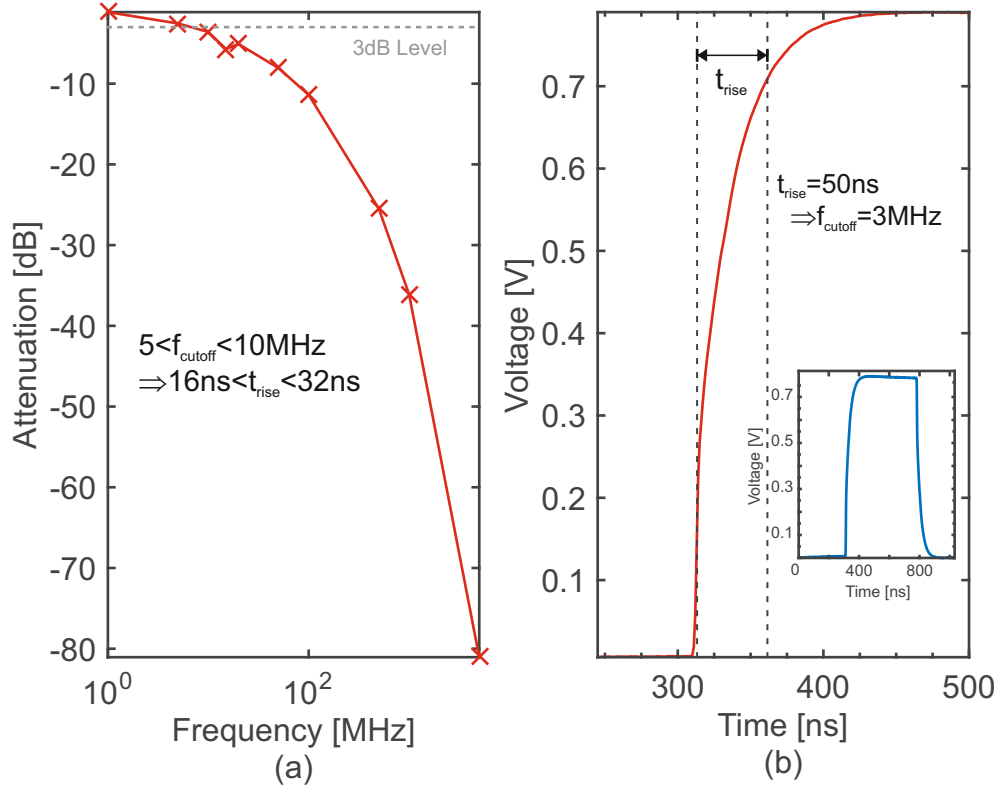


Figure 6.3: a) Plot showing attenuation of the cryogenic cable at each frequency. b) Rising part of the response of the cryogenic cable to a box pulse with sub-ns rise time. The inset shows the complete response to the box pulse.

expected since the core and the shield of the cable are made of stainless steel, a relatively poor conductor. Figure 6.3a shows the attenuation at each frequency for our cable according to the manufacturer CMR-Direct. The values are adjusted to 2 m length of our cable. A 3 dB loss already occurs at a frequency of around 10 MHz. This cutoff frequency gives a rise time of 15 ns. In order to verify this, we have sent a rectangular pulse through a similar cable where the output was connected to an oscilloscope. In Figure 6.3b we plot the output from the oscilloscope, the response, and extracted a rise time of approximately 50 ns which is on the same order of magnitude than the manufacturer specifications. The deviation can be attributed to the 1GHz bandwidth of our oscilloscope.

At this point, we are only missing the frequency response of the sample. However, this is rather difficult since it is hard to assess how the frequency response of our field effect device changes at lower bath temperature. At room temperature, measuring resistance and capacitance on deduces a rise time on the order of 1 ms giving a cutoff frequency on the order of kHz [88]. Furthermore, let us note that

6 Arbitrary in-situ control of the potential landscape

the connection between the sample and the PCB is established through gold wire bonds. However, we can neglect the influence of the wire bonds since they do not exceed 1cm length, hence, losses are negligible.

It might seem now as if the field-effect device will contribute the most to the overall rise time of our circuit. However this is a misleading notion since our goal is to control the potential at the gates of the field effect device. Thus, our only concern is the voltage present at the gate electrodes. The high impedance of the sample will only lead to a reflection of our voltage pulses, i.e. not to current dissipation in the field-effect device itself. Ideally, one would confirm this conclusion with a network analyzer. This would directly give us the frequency dependent impedance and show us where the majority of reflections occur in the circuit. Unfortunately we do not have this equipment at our disposal. We have therefore developed an alternative approach to overcome the impedance mismatch and gain arbitrary control of the electric field applied in the quantum wells.

6.4 Engineering the arbitrary voltage pulse

Our approach to engineer an arbitrary voltage pulse relies on determining the transfer function of the whole circuit including the sample. An excellent introduction to the field of control theory and transfer functions can be found in [8]. Here we will just briefly review the key equations necessary to understand our technique.

The transfer function of a circuit is a mathematical representation that describes the relation between the input and output of a linear-time-invariant system in the frequency domain according to

$$Y(s) = H(s)X(s), \quad s = i\omega \quad (6.1)$$

where $Y(s)$ and $X(s)$ are the Laplace transforms of the input and output signal $x(t)$ and $y(t)$ defined as:

$$X(s) = \int_0^{\infty} x(t) \cdot e^{-st} dt \quad (6.2)$$

$$Y(s) = \int_0^{\infty} y(t) \cdot e^{-st} dt \quad (6.3)$$

By inverting the transfer function we obtain the relationship

$$X_{Mod}(s) = H^{-1}(s)Y(s) \quad (6.4)$$

which gives us the laplace transformed $X_{mod}(S)$ of the modified signal input $x_{mod}(t)$ to obtain our desired output signal $y(t)$. This method proves to be quite powerful since no detailed knowledge of the circuit is needed to obtain $H(s)$ [8]. Ideally one would send a dirac-delta function as input since the two-sided Laplace transform of a dirac-delta function is one. Thus, one directly obtains the transfer function by performing the two-sided Laplace transform on the output signal. However, this method imposes high-requirements on the pulse generator and measurement device. An alternative route is to apply a step function and deduce the transfer function from the response. Let us note at this point that a precise knowledge of the transfer function allows us to engineer pulses of arbitrary steepness only limited by the resolution of our measurement devices. Therefore, in principle, it allows us to compensate for all high-frequency losses of our circuit.

6.4.1 Experimental determination of the Transfer Function

To determine the transfer function we generate a rectangular voltage pulse as input $x(t)$ using our AWG. We use a bias-tee to combine the DC bias with the output of the AWG. Since the goal is to achieve at will control of the exciton interaction with the internal electric-field, the luminescence signal of the indirect excitons serves as output signal $y(t)$. Thus, we have injected a gas of indirect excitons in our trap. The excitation power was set to $P_{ex} = 2 \mu\text{W}$ to ensure a high enough signal to noise ratio. The guard and center gate were set to $V_G = V_C - 5\text{V}$. The amplitude of the rectangular pump was set to $V_{Pulse} = 0.5\text{V}$. The procedure for the characterization is always as follows (see Figure6.4):

First we record images and increase the delay with a fixed step size, in other words, we record a calibration movie to study the evolution of the exciton blueshift $E_{off}(t)$ with $V_{Pulse} = 0\text{V}$. This is necessary to eliminate the influence of the exciton decay in the pulse response as it is a priori not related to the applied voltage pulse. We then record a second movie $E_{on}(t)$ with all parameters being the same, except this time we set $V_{Pulse} = 0.5\text{V}$. Now we have two plots showing the peak position of the photoluminescence vs time. We define the response as $y(t) = E_{on}(t) - E_{off}(t)$, thus, eliminating the influence of the decaying exciton population. Figure 6.4c shows the response to the rectangular pulse. We can identify two distinct time constants. A short rise of 6 ns in the beginning followed by a slower rise starting

6 Arbitrary in-situ control of the potential landscape

from 128 ns to 152 ns. The signal then starts to decay towards the baseline without prior saturation.

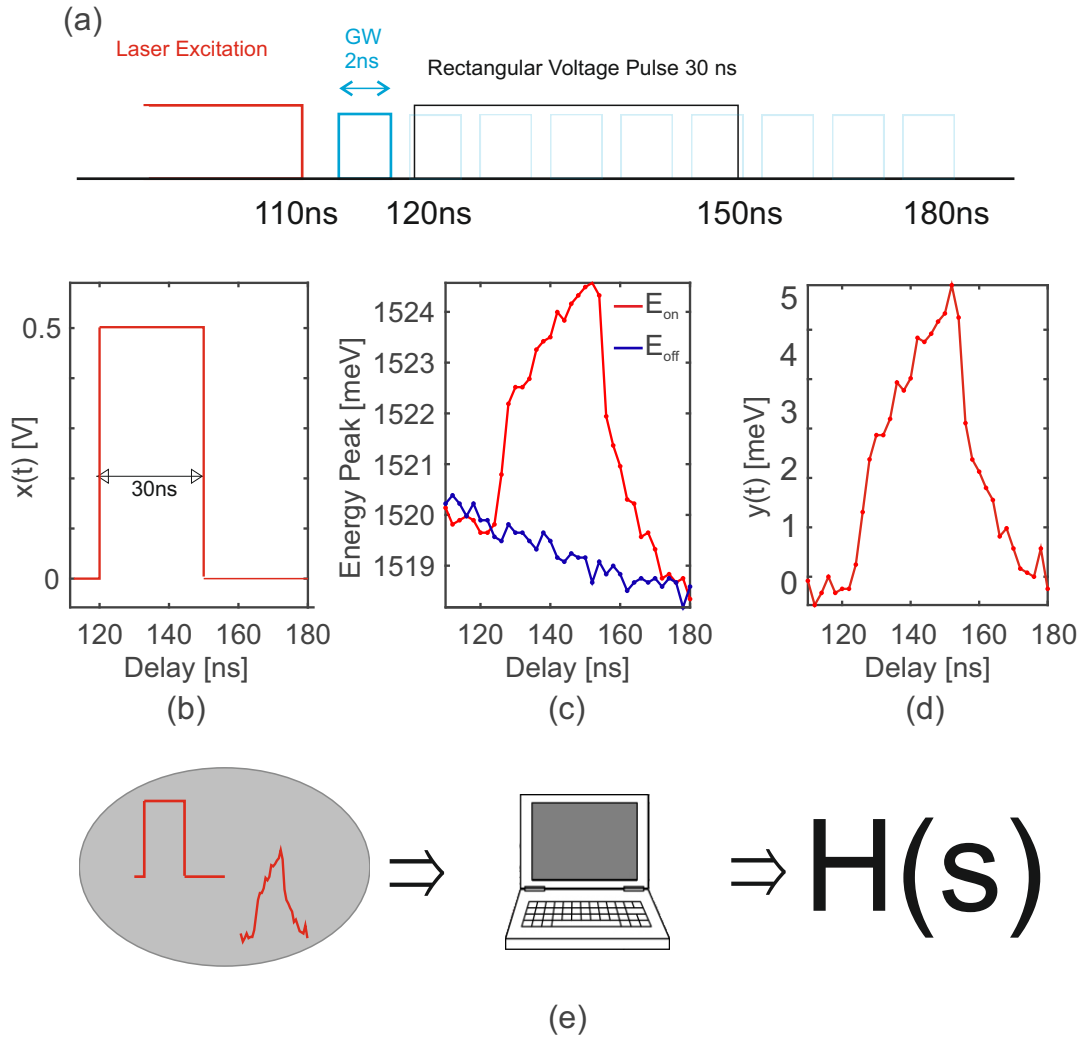


Figure 6.4: a) Measurement Sequence: We inject a gas of indirect excitons into the electrostatic trap. The spectral peak is recorded with a 2 ns gate width and the delay is varied in 2 ns steps from 110 to 180 ns. We record an average image of 10×30 s per image at each delay. The excitation power is set to $P_{ex} = 2 \mu\text{W}$. b) The trap gate is pulsed with a 30 ns long voltage pulse with $V_{pulse} = 0.5$ V. c) Plot showing the evolution of the spectral peak versus time, extracted from the accumulated spectra for $V_{pulse} = 0.5$ V (red) and $V_{pulse} = 0$ V (blue). d) Response $y(t) = E_{on} - E_{off}$, corrected for the decay of the exciton population in order to e) supply the software with $x(t)$ and $y(t)$ to obtain the response function $H(s)$.

To determine the transfer function we use the system identification toolbox provided by Matlab. Finding the transfer function is thus reduced to providing the input $x(t)$ and output $y(t)$ as numeric arrays in Matlab. The software will then provide us with the transfer function of general polynomial form for a linear time

independent continuous system which can easily be inverted:

$$H(s) = \frac{b_n s^n + b_{n-1} s^{n-1} + \dots + b_1 s + b_0}{s^n + a_{n-1} s^{n-1} + \dots + a_1 s + a_0} \implies H^{-1}(s) = \frac{s^n + a_{n-1} s^{n-1} + \dots + a_1 s + a_0}{b_n s^n + b_{n-1} s^{n-1} + \dots + b_1 s + b_0} \quad (6.5)$$

6.4.2 Determining the corrected pulseshape

Using the system identification toolbox, we reverse engineer the modified input pulse $x_{\text{mod}}(t)$ that gives us the desired response, a box pulse. We simply supply the toolbox with the box pulse and the experimentally determined inverse transfer function. The modified input pulse can then be loaded into the AWG in order to validate the degree of success of our approach. Figure 6.5b shows the reverse engineered $x_{\text{mod}}(t)$ pulse that we obtain. The main characteristics of this pulse are the over and undershoot which coincide with the flanks of our rectangular pulse. This is expected due to the high-frequency losses in the coaxial cable which have to be compensated by overshoots. Figure 6.5c shows the response of the exciton gas to the modified signal at 330 mK and 2.5 K respectively. The output $y(t)$ can be seen in figure 6.5d.

The result shows a drastic improvement of the response in terms of steep rise and fall times. The rise time is $t_{\text{rise}} = 2 \text{ ns}$, which corresponds to the temporal resolution limit of the camera while the fall time is $t_{\text{fall}} = 6 \text{ ns}$. We explain the deviation of the fall time from the optimum of 2 ns to our sampling method. Since we are only able to record the dynamics down to a 2 ns resolution, this give a cutoff frequency off 80 MHz. Thus, higher frequencies can not be considered when the transfer function is determined. We can thus conclude that, despite our limited temporal resolution, our method works well. Furthermore, during the data acquisition, which takes three hours per run, no increase of the bath temperature was observed. We can thus conclude that our method allows for an arbitrary in-situ control of the exciton potential without leading to detrimental heating effects of the sample. Let us note that there are of course dissipation effects in the coaxial cable inside of the cryostat due to its relatively high resistivity. However, one has to keep in mind that this cable is 2 m long, thus, the dissipation is distributed along the whole transmission line of which only 40 cm are in direct contact with the lowest cooling stage.

As a final point let us note that figure 6.5d also shows a drastic drop of intensity coinciding with the rise and fall of our of the box pulse. This suggests that the

6 Arbitrary in-situ control of the potential landscape

exciton gas is heated during the pulse. However this conclusion is not straightforward.

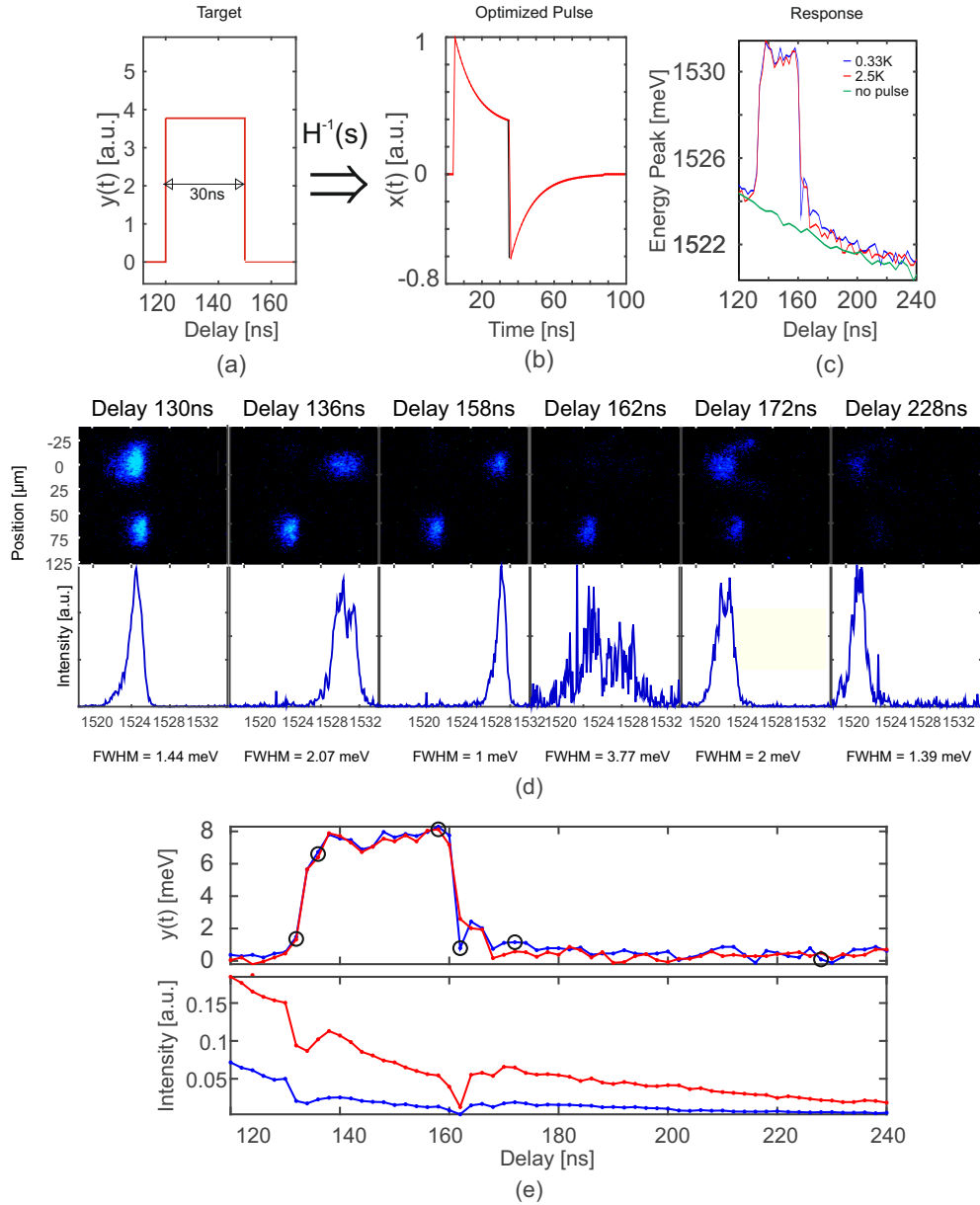


Figure 6.5: Correcting the pulse shape: a) Target pulse shape $y(t)$ that yields b) the modified pulse after performing the inverse laplace transform of the product $H^{-1}(s)Y(s)$. c) Plot of the excitons dynamics with the corrected pulse shape at a bath temperature of 0.33 K (blue) and 2.5 K (red). d) Spectrally resolved images of the exciton cloud for various delays. e) Top: Response of the excitons corrected for the population decay. Bottom: Evolution of the integrated intensity with time showing that the beginning and end of the pulse coincides with a loss in intensity at both bath temperatures. Recording Parameters: Gate Width 2ns, 5x60s per point, $V_G = -3.5\text{V}$, $V_C = -4.8\text{V}$, $V_{\text{Pulse}} = 1.5\text{V}$. e-g) Same as c-d) for a gaussian of 30 ns width (blue gaussian 30ns width, red experimental data). The deviation around delay 200 ns in f) can be attributed to the weak signal.

Indeed, simple considerations regarding the exciton population within the light cone do not indicate that heating is dominant. Using a Maxwell-Boltzmann-distribution we can derive the fraction $n_{LC}(T)$ of excitons within the light cone through the cumulative distribution function

$$n_{LC}(T) = \int_0^{E_{LC}} f(E, T) dE = \int_0^{E_{LC}} \frac{1}{k_B T} e^{-\frac{E}{k_B T}} dE = 1 - e^{-\frac{E_{LC}}{k_B T}},$$

where $f(E, T)$ is the Maxwell-Boltzmann energy distribution, k_B the Boltzmann-constant, $E_{LC} = 0.15 \text{ meV}$ the upper boundary of the light cone and T the temperature of the exciton gas. Assuming that the darkening is caused by a heating of the exciton gas due to the voltage pulse, we can extract the temperature increase ΔT through the loss of excitons in the light cone. This loss is related to the photoluminescence which can be expressed as a ratio γ according to

$$\gamma(T, \Delta T) = \frac{I_{X,pulse}(t)}{I_X(t)} = \frac{N_X n_{LC}(T + \Delta T) e^{-\frac{t}{\tau}}}{N_X n_{LC}(T) e^{-\frac{t}{\tau}}} = \frac{n_{LC}(T + \Delta T)}{n_{LC}(T)} = \frac{1 - e^{-\frac{E_{LC}}{k_B(T+\Delta T)}}}{1 - e^{-\frac{E_{LC}}{k_B T}}}, \quad (6.6)$$

$$\begin{aligned} \gamma(T, \Delta T) &= \frac{I_{X,pulse}(t)}{I_X(t)} = \frac{N_X n_{LC}(T+\Delta T) e^{-\frac{t}{\tau}}}{N_X n_{LC}(T) e^{-\frac{t}{\tau}}} \\ &= \frac{n_{LC}(T+\Delta T)}{n_{LC}(T)} = \frac{1 - e^{-\frac{E_{LC}}{k_B(T+\Delta T)}}}{1 - e^{-\frac{E_{LC}}{k_B T}}}, \end{aligned} \quad (6.7)$$

where I_X denotes the integrated intensity, N_X the total number of excitons and ΔT the temperature increase due to the pulse. Solving equation 6.6 for ΔT then gives us the temperature increase.

From our experiments we have extracted $\gamma(0.33 \text{ mK}, \Delta T_{0.33 \text{ K}})_{t=132 \text{ ns}} = 0.42$ and $\gamma(2.5 \text{ K}, \Delta T_{2.5 \text{ K}})_{t=132 \text{ ns}} = 0.72$ around delay 132 ns which gives an effective temperature increase of $\Delta T_{0.33 \text{ K}} = 2.9 \text{ K}$ and $\Delta T_{2.5 \text{ K}} = 1.38 \text{ K}$.

By comparing these numbers to the cooling power of our cryostat and for the two delays where the darkening is observed, we can estimate if the darkening can be associated to a temperature increase of the exciton gas. For a bath temperature of 330 mK the cooling power of our cryostat at the sample holder is 0.1 mW compared to 50mW at a bath temperature of 2.5 K. This corresponds to a factor of 10^2 between the two bath temperatures whereas the temperature increases due to the darkening scales with a factor of 2. Furthermore we observe the darkening also at the delay 162 ns. At these position we obtain similar values for both temperatures $\gamma(0.33 \text{ mK}, \Delta T_{0.33 \text{ K}})_{t=162 \text{ ns}} = 0.36$ and $\gamma(2.5 \text{ mK}, \Delta T_{0.33 \text{ K}})_{t=162 \text{ ns}} = 0.32$. However, the steep rising and falling flanks of the modified pulse depicted

6 Arbitrary in-situ control of the potential landscape

in figure 6.5b both have a magnitude of 1.5 V. Thus for a fixed bath temperature T_B one should observe $\gamma(T_B, \Delta T)_{t=132ns} = \gamma(T_B, \Delta T)_{t=162ns}$ which is not the case in our experiments. We can therefore exclude a simple thermal heating of the exciton gas as a reason for the observed darkening when we pulse the trap. A heating of the sample can be excluded in general due to the resistance on the order of several M Ω . The darkening is thus subject of ongoing investigations. It is worth mentioning that this darkening makes it difficult to localize the energy peak with a sufficiently high signal to noise ratio which can cause the observed deviations of the response $y(t)$ from the ideal target pulse.

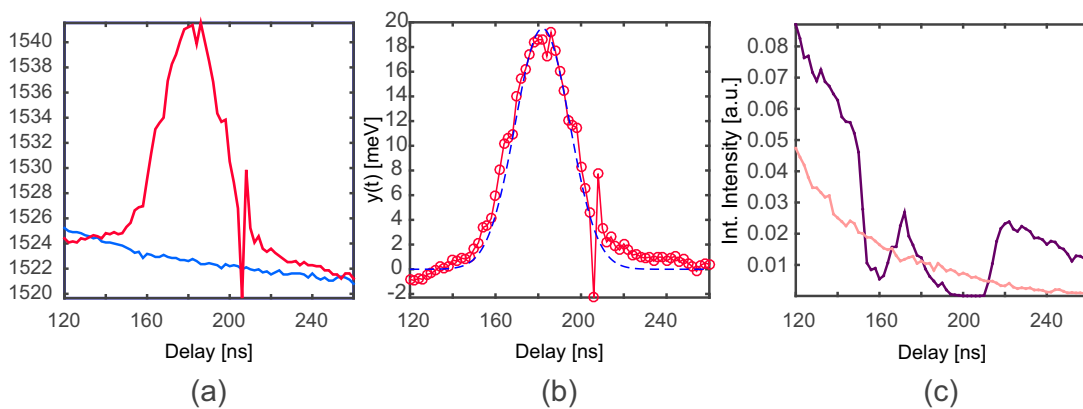


Figure 6.6: a) Exciton Response to a Gaussian pulse of 30 ns width (red) together with calibration movie on the guard(blue). b) Response of the excitons corrected for the population decay(red) showing good agreement with a Gaussian of 30 ns width(blue dashed). c) Evolution of the integrated intensity with time showing a smooth decline in intensity coinciding with the rise and fall of the Gaussian pulse. Recording Parameters: Gate Width 2ns, 5x60s per point, $V_G = -3.5V$, $V_C = -4.8V$, $V_{Pulse} = 1.5V$. The deviation around delay 200 ns in b) can be attributed to the weak photoluminescence signal.

To show the flexibility of our approach in terms of arbitrary control of the blueshift vs time, we have computed a modified pulse to obtain a 30 ns wide Gaussian response of the blueshift. The results can be seen in figures 6.5e-g and show a remarkably precise replication of the Gaussian pulse shape. Let us note that the amplitude of the exciton shift is a factor of two bigger than for the box pulse. We can attribute this to the frequency spectrum associated for the applied pulse shape. High-frequency components in the Gaussian pulse are less dominant than for a step box pulse. Thus less energy is dissipated in the coaxial cables due to high frequency losses which can then contribute to the blueshift.

6.5 Conclusion

In this chapter we have introduced a novel method to achieve in-situ control of the trapping potential confining the indirect excitons. This degree of control was achieved by characterizing the transfer function of our system, comprising of the transmission lines and custom designed printed circuit board with conductor-backed coplanar waveguides to minimize impedance mismatch on the input side and the blueshift of the exciton gas as output. The determination of the transfer function by a test square pulse allowed for the generation of modified voltage pulses which resulted in the desired response of the exciton gas in terms of the exciton-field interaction on a time scale of 2-6 ns, despite a characteristic time constant of 50 ns due to high frequency losses in the transmission lines. The main limitation in our approach is the temporal resolution of our optical detection with 2 ns which imposes an cutoff frequency of 80Mhz below which frequencies are contributing to the determination of the transfer function. To demonstrate the success of our approach in terms of arbitrary control of the exciton blueshift, we have shown a gaussian response of the blueshift which relies on the exact same method. Furthermore we have demonstrated through careful analysis of the integrated intensity that the loss of photoluminescence is not caused by heating due to the voltage pulse. Thus, our approach is suitable for the manipulation of cold excitons, i.e. the exploration of evaporative cooling of cold indirect excitons.

7 Conclusion and Outlook

In this thesis we have presented experimental results on trapped and cold gases of spatially indirect excitons. The experiments were performed on coupled GaAs/ Al-GaAs quantum wells embedded in a field effect device. The excitons were trapped in an electrostatic potential, realized by applying voltage biases to individual surface gate electrodes. These electrodes control the electric field between the surface of our device and its ohmic substrate. The observed narrow spectral linewidth below 1 meV at 330 mK demonstrate that we realized a weakly interacting exciton gas where inhomogeneous broadening effects are greatly suppressed, but not completely absent due to free photo-induced charge carriers in the quantum well.

The device that we characterized provides an unprecedented degree of control over exciton gases. In particular, it allows us to control the exciton density in the trap, for temperatures up to 3.5 K, such that a quantitative analysis is possible. Our measurements show an efficient cooling of the exciton cloud through a narrowing of the spectral linewidth and a contraction of the exciton cloud. This is accompanied by a 50% decrease of the photoluminescence when the bath temperature is lowered, contradictory to the behavior for a gas obeying Maxwell-Boltzmann statistics. In this situation, the decreasing temperature leads to an increase of excitons in the radiative region, thus, to an enhanced photoluminescence intensity which is not observed in our experiments. Instead we clearly show, that our exciton population exhibits non-classical behavior. Since the overall exciton density is fixed for all temperatures we are led to conclude that Bose stimulation from bright to dark states is responsible for the disproportionate population of the dark exciton ground state. To confirm these results we have provided a phenomenological model which demonstrates that the exciton population dynamics in bright and dark states can not be accounted for when Bose-Stimulation is not included at the lowest bath temperature. Unfortunately, we are not able to extract any long-range coherence by means of interference measurements, as our studies are limited by intensity fluctuations. As a result, a coherent bright part in our predominantly, dark exciton condensate is blurred. Furthermore we have currently no method to distinguish bright excitons in the condensed state from

7 Conclusion and Outlook

the ones in the thermal part of the trapped gas. A possible way to obtain direct quantitative results about the exciton distribution, among bright and dark states, could be obtained by performing microwave spectroscopy. Since the splitting between bright and dark excitons lies in the GHz range, Rabi-Oscillations, as performed in atomic physics experiments, could be used to probe the exciton gas with a π – pulse to invert the population of bright and dark states. This would render a dark condensate bright, making it observable via their emitted photoluminescence.

As part of this thesis we have also demonstrated a novel method to arbitrarily manipulate the electrostatic landscape confining the indirect excitons. This degree of control was achieved by determining the transfer function of our setup which links the response of our excitons to the voltage pulse applied to the electrodes in a deterministic manner. The impedance mismatch was minimized using transmission lines with constant impedance and a custom designed printed circuit board on which the field effect device is mounted. Thus, the impedance mismatching is negligible since it occurs less than 1 cm away from the field effect device. Our approach eliminates the dependence on impedance matching networks which rely on passive components acting as heating source close to the sample. Furthermore the use of a transmission line with a highly resistive core leads to a distribution of heat throughout the cryogenic system, due to reflected signals from the high impedance field effect device. This novel approach could pave the way towards a controlled temperature reduction of trapped exciton gases via evaporative cooling. Evaporative cooling could then reduce the gas temperature below 300 mK where exciton-phonon interactions are not efficient enough to contribute to the cooling of indirect exciton gases in GaAs/AlGaAs coupled quantum wells.

Bibliography

- [1] M. Alloing. *Experimental evidence for the quantum condensation of ultracold dipolar excitons*. PhD thesis, Universitat Politècnica de Catalunya, 2014.
- [2] M. Alloing, M. Beian, M. Lewenstein, D. Fuster, Y. González, L. González, R. Combescot, M. Combescot, and F. Dubin. Evidence for a bose-einstein condensate of excitons. *EPL (Europhysics Letters)*, 107:10012, July 2014.
- [3] M. Alloing, A. Lemaître, E. Galopin, and F. Dubin. Optically programmable excitonic traps. *Scientific Reports*, 3:1578, April 2013.
- [4] T. Amand, X. Marie, P. Le Jeune, M. Brousseau, D. Robart, J. Barrau, and R. Planel. Spin quantum beats of 2D excitons. *Physical Review Letters*, 78:1355–1358, February 1997.
- [5] M. H. Anderson, J. R. Ensher, M. R. Matthews, C. E. Wieman, and E. A. Cornell. Observation of bose-einstein condensation in a dilute atomic vapor. *Science*, 269:198–201, July 1995.
- [6] Lucio Claudio Andreani, Francesco Tassone, and Franco Bassani. Radiative lifetime of free excitons in quantum wells. *Solid state communications*, 77(9):641–645, 1991.
- [7] MR Andrews, CG Townsend, H-J Miesner, DS Durfee, DM Kurn, and W Ketterle. Observation of interference between two bose condensates. *Science*, 275(5300):637–641, 1997.
- [8] John Bechhoefer. Feedback for physicists: A tutorial essay on control. *Reviews of Modern Physics*, 77(3):783, 2005.
- [9] M. Beian, M. Alloing, E. Cambril, C. Gomez Carbonell, J. Osmond, A. Lemaître, and F. Dubin. Long-lived spin coherence of indirect excitons in GaAs coupled quantum wells. *EPL (Europhysics Letters)*, 110:27001, April 2015.

Bibliography

- [10] E. Blackwood, M. J. Snelling, R. T. Harley, S. R. Andrews, and C. T. B. Foxon. Exchange interaction of excitons in GaAs heterostructures. *Phys. Rev. B*, 50:14246–14254, November 1994.
- [11] J. M. Blatt, K. W. Böer, and W. Brandt. Bose-einstein condensation of excitons. *Physical Review*, 126:1691–1692, June 1962.
- [12] I. Bloch, J. Dalibard, and W. Zwerger. Many-body physics with ultracold gases. *Reviews of Modern Physics*, 80:885–964, July 2008.
- [13] S Bose. Plancks gesetz und lichtquantenhypothese. *Zeitschrift fur Physik*, 26:178–181, December 1924.
- [14] L. V. Butov, C. W. Lai, A. L. Ivanov, A. C. Gossard, and D. S. Chemla. Towards bose-einstein condensation of excitons in potential traps. *Nature*, 417:47–52, May 2002.
- [15] G. Chen, R. Rapaport, L. N. Pfeifer, K. West, P. M. Platzman, S. Simon, Z. Vörös, and D. Snoke. Artificial trapping of a stable high-density dipolar exciton fluid. *Phys. Rev. B*, 74(4):045309, July 2006.
- [16] P. C. M. Christianen, F. Piazza, J. G. S. Lok, J. C. Maan, and W. van der Vleuten. Magnetic trap for excitons. *Physica B Condensed Matter*, 249:624–627, June 1998.
- [17] M. Combescot, O. Betbeder-Matibet, and R. Combescot. Bose-Einstein condensation in semiconductors: The key role of dark excitons. *Physical Review Letters*, 99(17):176403, October 2007.
- [18] M. Combescot and M. N. Leuenberger. General argument supporting bose-einstein condensate of dark excitons in single and double quantum wells. *Solid State Communications*, 149:567–571, April 2009.
- [19] Monique Combescot, Odile Betbeder-Matibet, and François Dubin. The many-body physics of composite bosons. *Physics Reports*, 463(5):215–320, 2008.
- [20] Monique Combescot and Christian Tanguy. New criteria for bosonic behavior of excitons. *EPL (Europhysics Letters)*, 55(3):390, 2001.
- [21] R. Combescot and M. Combescot. “Gray” BCS condensate of excitons and internal josephson effect. *Physical Review Letters*, 109(2):026401, July 2012.

- [22] E. A. Cornell and C. E. Wieman. Nobel lecture: Bose-einstein condensation in a dilute gas, the first 70 years and some recent experiments. *Rev. Mod. Phys.*, 74:875–893, Aug 2002.
- [23] Franco Dalfovo, Stefano Giorgini, Lev P. Pitaevskii, and Sandro Stringari. Theory of bose-einstein condensation in trapped gases. *Rev. Mod. Phys.*, 71:463–512, Apr 1999.
- [24] K. B. Davis, M.-O. Mewes, M. R. Andrews, N. J. van Druten, D. S. Durfee, D. M. Kurn, and W. Ketterle. Bose-einstein condensation in a gas of sodium atoms. *Physical Review Letters*, 75:3969–3973, November 1995.
- [25] A. Einstein. Quantentheorie des einatomigen idealen gases: Zweite abhandlung. *Sitzungber. Preuss. Akad. Wiss*, 3, 1925.
- [26] L Esaki and R Tsu. Ibm research report no. *RC-2418*, 1969.
- [27] Leo Esaki and Ray Tsu. Superlattice and negative differential conductivity in semiconductors. *IBM Journal of Research and Development*, 14(1):61–65, 1970.
- [28] J. Feldmann, G. Peter, E. O. Göbel, P. Dawson, K. Moore, C. Foxon, and R. J. Elliott. Linewidth dependence of radiative exciton lifetimes in quantum wells. *Physical Review Letters*, 59:2337–2340, November 1987.
- [29] A. Gärtner, A. W. Holleitner, J. P. Kotthaus, and D. Schuh. Drift mobility of long-living excitons in coupled GaAs quantum wells. *Applied Physics Letters*, 89(5):052108, July 2006.
- [30] A. Gärtner, L. Prechtel, D. Schuh, A. W. Holleitner, and J. P. Kotthaus. Micropatterned electrostatic traps for indirect excitons in coupled GaAs quantum wells. *Phys. Rev. B*, 76(8):085304, August 2007.
- [31] Stephan Glutsch. *Excitons in Low-Dimensional Semiconductors: Theory Numerical Methods Applications*, volume 141. Springer Science & Business Media, 2013.
- [32] Zoran Hadzibabic, Peter Krüger, Marc Cheneau, Baptiste Battelier, and Jean Dalibard. Berezinskii–kosterlitz–thouless crossover in a trapped atomic gas. *Nature*, 441(7097):1118–1121, 2006.
- [33] A. T. Hammack, N. A. Gippius, S. Yang, G. O. Andreev, L. V. Butov, M. Hanson, and A. C. Gossard. Excitons in electrostatic traps. *J. Appl. Phys.*, 99:066104, March 2006.

Bibliography

- [34] A. T. Hammack, M. Griswold, L. V. Butov, L. E. Smallwood, A. L. Ivanov, and A. C. Gossard. Trapping of Cold Excitons in Quantum Well Structures with Laser Light. *Physical Review Letters*, 96(22):227402, June 2006.
- [35] A. A. High, A. T. Hammack, L. V. Butov, L. Mouchliadis, A. L. Ivanov, M. Hanson, and A. C. Gossard. Indirect excitons in elevated traps. *Nano Letters*, 9:2094–2098, May 2009.
- [36] A. A. High, J. R. Leonard, A. T. Hammack, M. M. Fogler, L. V. Butov, A. V. Kavokin, K. L. Campman, and A. C. Gossard. Spontaneous coherence in a cold exciton gas. *Nature*, 483:584–588, March 2012.
- [37] A. A. High, J. R. Leonard, M. Remeika, L. V. Butov, M. Hanson, and A. C. Gossard. Condensation of excitons in a trap. *Nano Letters*, 12(5):2605–2609, 2012.
- [38] A. A. High, E. E. Novitskaya, L. V. Butov, M. Hanson, and A. C. Gossard. Control of exciton fluxes in an excitonic integrated circuit. *Science*, 321:229–231, July 2008.
- [39] A. A. High, A. K. Thomas, G. Grosso, M. Remeika, A. T. Hammack, A. D. Meyertholen, M. M. Fogler, L. V. Butov, M. Hanson, and A. C. Gossard. Trapping indirect excitons in a GaAs quantum-well structure with a diamond-shaped electrostatic trap. *Physical Review Letters*, 103(8):087403, August 2009.
- [40] A. L. Ivanov. Quantum diffusion of dipole-oriented indirect excitons in coupled quantum wells. *EPL (Europhysics Letters)*, 59:586–591, August 2002.
- [41] A. L. Ivanov. Thermalization and photoluminescence dynamics of indirect excitons at low bath temperatures. *Journal of Physics Condensed Matter*, 16:3629, September 2004.
- [42] A. L. Ivanov, P. B. Littlewood, and H. Haug. Bose-einstein statistics in thermalization and photoluminescence of quantum-well excitons. *Phys. Rev. B*, 59:5032–5048, February 1999.
- [43] A. L. Ivanov, E. A. Muljarov, L. Mouchliadis, and R. Zimmermann. Comment on “Photoluminescence ring formation in coupled quantum wells: Excitonic versus ambipolar diffusion”. *Physical Review Letters*, 104(17):179701, April 2010.

- [44] AL Ivanov, PB Littlewood, and H Haug. Bose–einstein statistics in photoluminescence of quantum well excitons. *Journal of luminescence*, 87:189–191, 2000.
- [45] L. V. Keldysh and A. N. Kozlov. Collective properties of excitons in semiconductors. *Soviet Journal of Experimental and Theoretical Physics*, 27:521, September 1968.
- [46] W Ketterle and NJ van Druten. Evaporative cooling of trapped atoms. *Advances in atomic, molecular, and optical physics*, 37:181–236, 1996.
- [47] Wolfgang Ketterle and N. J. van Druten. Bose-einstein condensation of a finite number of particles trapped in one or three dimensions. *Phys. Rev. A*, 54:656–660, Jul 1996.
- [48] C. Kittel. *Introduction to Solid State Physics*. Wiley, 2004.
- [49] John Michael Kosterlitz and David James Thouless. Ordering, metastability and phase transitions in two-dimensional systems. *Journal of Physics C: Solid State Physics*, 6(7):1181, 1973.
- [50] K. Kowalik-Seidl, X. P. Vögele, B. N. Rimpfl, S. Manus, J. P. Kotthaus, D. Schuh, W. Wegscheider, and A. W. Holleitner. Long exciton spin relaxation in coupled quantum wells. *Applied Physics Letters*, 97(1):011104, July 2010.
- [51] K. Kowalik-Seidl, X. P. Vögele, B. N. Rimpfl, G. J. Schinner, D. Schuh, W. Wegscheider, A. W. Holleitner, and J. P. Kotthaus. Tunable photoemission from an excitonic antitrap. *Nano Letters*, 12:326–330, January 2012.
- [52] YY Kuznetsova, P Andreakou, MW Hasling, JR Leonard, EV Calman, LV Butov, M Hanson, and AC Gossard. Two-dimensional snowflake trap for indirect excitons. *Optics letters*, 40(4):589–592, 2015.
- [53] S Lazić, A Violante, K Cohen, R Hey, R Rapaport, and PV Santos. Scalable interconnections for remote indirect exciton systems based on acoustic transport. *Physical Review B*, 89(8):085313, 2014.
- [54] S. Lazić, A. Violante, K. Cohen, R. Hey, R. Rapaport, and P. Ventura Santos. Scalable interconnections for remote exciton systems. *arXiv*, page 1310.6912, October 2013.
- [55] Anthony J. Leggett. Bose-einstein condensation in the alkali gases: Some fundamental concepts. *Rev. Mod. Phys.*, 73:307–356, Apr 2001.

Bibliography

- [56] J. R. Leonard, Y. Y. Kuznetsova, S. Yang, L. V. Butov, T. Ostatnický, A. Kavokin, and A. C. Gossard. Spin transport of excitons. *Nano Letters*, 9:4204–4208, December 2009.
- [57] Jia Ling Lin and J. P. Wolfe. Bose-einstein condensation of paraexcitons in stressed Cu_2O . *Phys. Rev. Lett.*, 71:1222–1225, Aug 1993.
- [58] F London. Nature. *London*, 141:643, 1938.
- [59] Yu E Lozovik and VI Yudson. Feasibility of superfluidity of paired spatially separated electrons and holes; a new superconductivity mechanism. *JETP lett*, 22(11):274–276, 1975.
- [60] S. A. Moskalenko. Reversible optico-hydrodynamic phenomena in a nonideal exciton gas. *Sov Phys-Sol State*, 4:199, 1962.
- [61] V. Negoita, D. W. Snoke, and K. Eberl. Harmonic-potential traps for indirect excitons in coupled quantum wells. *Phys. Rev. B*, 60:2661–2669, Jul 1999.
- [62] I-K Oh and Jai Singh. Excitonic relaxation through phonon interactions in quantum wells. *Journal of luminescence*, 85(4):233–246, 2000.
- [63] W. Pauli. The connection between spin and statistics. *Phys. Rev.*, 58:716–722, Oct 1940.
- [64] William D Phillips. Nobel lecture: Laser cooling and trapping of neutral atoms. *Reviews of Modern Physics*, 70(3):721, 1998.
- [65] C Piermarocchi, F Tassone, V Savona, A Quattropani, and P Schwendimann. Nonequilibrium dynamics of free quantum-well excitons in time-resolved photoluminescence. *Physical Review B*, 53(23):15834, 1996.
- [66] L. P. Pitaevskii and S. Stringari. *Bose-einstein condensation*. Clarendon Press, Oxford, 2003.
- [67] R. Rapaport and G. Chen. Experimental methods and analysis of cold and dense dipolar exciton fluids. *Journal of Physics Condensed Matter*, 19:C5207, July 2007.
- [68] Ronen Rapaport, Gang Chen, Steven Simon, Oleg Mitrofanov, Loren Pfeiffer, and P. M. Platzman. Electrostatic traps for dipolar excitons. *Phys. Rev. B*, 72:075428, Aug 2005.

- [69] M Remeika, JR Leonard, CJ Dorow, MM Fogler, LV Butov, M Hanson, and AC Gossard. Measurement of exciton correlations using electrostatic lattices. *Physical Review B*, 92(11):115311, 2015.
- [70] Emmanuel Rosencher and Borge Vinter. *Optoelectronics*. Cambridge University Press, 2002.
- [71] David Rychtarik, B Engeser, H-C Nägerl, and R Grimm. Two-dimensional bose-einstein condensate in an optical surface trap. *Physical review letters*, 92(17):173003, 2004.
- [72] G. J. Schinner, J. Repp, E. Schubert, A. K. Rai, D. Reuter, A. D. Wieck, A. O. Govorov, A. W. Holleitner, and J. P. Kotthaus. Confinement and interaction of single indirect excitons in a voltage-controlled trap formed inside double InGaAs quantum wells. *Physical Review Letters*, 110(12):127403, March 2013.
- [73] G. J. Schinner, E. Schubert, M. P. Stallhofer, J. P. Kotthaus, D. Schuh, A. K. Rai, D. Reuter, A. D. Wieck, and A. O. Govorov. Electrostatically trapping indirect excitons in coupled $\text{In}_x\text{Ga}_{1-x}\text{As}$ quantum wells. *Phys. Rev. B*, 83(16):165308, April 2011.
- [74] D. Semkat, S. Sobkowiak, G.. Manzke, and H. Stolz. Comment on “Condensation of excitons in a trap”. *Nano Letters*, 12(9):5055–5057, 2012.
- [75] Y. Shilo, K. Cohen, B. Laikhtman, K. West, L. Pfeiffer, and R. Rapaport. Particle correlations and evidence for dark state condensation in a cold dipolar exciton fluid. *Nature Communications*, 4, August 2013.
- [76] Rainee N. Simons. *Coplanar Waveguide Transitions*. John Wiley & Sons, Inc., 2002.
- [77] K. Sivalertporn, L. Mouchliadis, A. L. Ivanov, R. Philp, and E. A. Muljarov. Direct and indirect excitons in semiconductor coupled quantum wells in an applied electric field. *Phys. Rev. B*, 85(4):045207, January 2012.
- [78] D. Snoke and G. M. Kavoulakis. Bose-Einstein condensation of excitons in Cu_2O : progress over 30 years. *Reports on Progress in Physics*, 77(11):116501, November 2014.
- [79] AV Soroko and AL Ivanov. Phonon-assisted relaxation kinetics of statistically degenerate excitons in high-quality quantum wells. *Physical Review B*, 65(16):165310, 2002.

Bibliography

- [80] P Stenius and AL Ivanov. Relaxation kinetics of quasi two-dimensional excitons coupled to a bath of bulk acoustic phonons. *Solid state communications*, 108(2):117–122, 1998.
- [81] V. B. Timofeev and A. V. Gorbunov. Bose-einstein condensation of dipolar excitons in double and single quantum wells. *Physica Status Solidi C*, 5:2379–2386, June 2008.
- [82] László Tisza. Transport phenomena in helium ii. *Nature*, 141:913, 1938.
- [83] L. Viña. Spin relaxation in low-dimensional systems. *Journal of Physics Condensed Matter*, 11:5929–5952, August 1999.
- [84] Adriano Violante, Kobi Cohen, Snežana Lazić, Rudolph Hey, Ronen Rapaport, and Paulo Ventura Santos. Dynamics of indirect exciton transport by moving acoustic fields. *New Journal of Physics*, 16(3):033035, 2014.
- [85] Z. Vörös, R. Balili, D. W. Snoke, L. Pfeiffer, and K. West. Long-distance diffusion of excitons in double quantum well structures. *Physical Review Letters*, 94(22):226401, June 2005.
- [86] Z. Vörös, D. W. Snoke, L. Pfeiffer, and K. West. Trapping excitons in a two-dimensional in-plane harmonic potential: Experimental evidence for equilibration of indirect excitons. *Physical Review Letters*, 97(1):016803, July 2006.
- [87] A. G. Winbow. *Subnanosecond control of excitons in coupled quantum well nanostructures: Photonic storage and Exciton Conveyer devices*. PhD thesis, University of California, San Diego, 2010.
- [88] AG Winbow, LV Butov, and AC Gossard. Photon storage with subnanosecond readout rise time in coupled quantum wells. *Journal of Applied Physics*, 104(6):063515, 2008.
- [89] James P Wolfe and Joon I Jang. The search for bose–einstein condensation of excitons in cu2o: exciton-auger recombination versus biexciton formation. *New Journal of Physics*, 16(12):123048, 2014.
- [90] R Zimmermann. Bose-einstein condensation of excitons: Promise and disappointment. *Problems of Condensed Matter Physics-Quantum Coherence Phenomena in Electron-Hole and Coupled Matter-Light Systems*, edited by AL Ivanov and SG Tikhodeev (Oxford University Press, 2007), page 281, 2008.

- [91] S. Zimmermann, A. O. Govorov, W. Hansen, J. P. Kotthaus, M. Bichler, and W. Wegscheider. Lateral superlattices as voltage-controlled traps for excitons. *Phys. Rev. B*, 56:13414–13421, Nov 1997.
- [92] S. Zimmermann, G. Schedelbeck, A. O. Govorov, A. Wixforth, J. P. Kotthaus, M. Bichler, W. Wegscheider, and G. Abstreiter. Spatially resolved exciton trapping in a voltage-controlled lateral superlattice. *Applied Physics Letters*, 73:154, July 1998.
- [93] S Zimmermann, A Wixforth, JP Kotthaus, Werner Wegscheider, and Max Bichler. A semiconductor-based photonic memory cell. *Science*, 283(5406):1292–1295, 1999.